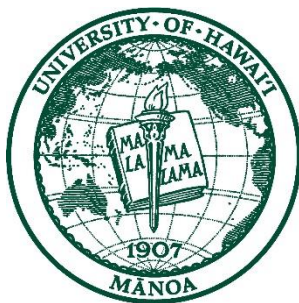

SIMULATED SPACE WEATHERING OF PLANETARY SURFACES

by

Parker Brian Crandall



Submitted to the Graduate Department in partial fulfillment of the requirements for the degree of

Master of Science in Chemistry

University of Hawai'i at Mānoa

December 2018

Thesis Committee:

Ralf Kaiser, Chairperson

Matthew Cain

Jeffrey Gillis-Davis

ACKNOWLEDGEMENTS

Foremost, I wish to thank my family for being my strongest support. My sisters, Jana, Abbey, and Allie for being my best friends and helping me each in your own way. To my parents, Brian and Susan, I thank you for the late night phone calls, packages, and thousands of miles traveled to show your love and support. You've taught me far more meaningful things than I could learn in a classroom and I owe everything to you. And to my grandfather, Robert Crandall—thank you for all the times you put the wind in my sails by sharing your optimism and faith in me.

My deepest gratitude goes to Kevin Hallstrom, Darren Wong, and Matthew Corry for burning the “lower lights”. Your counsel, wisdom, and friendship has been the answer I needed many times over.

I wish to mention my mentors and friends in the academic community from whom I've learned so much. To Shane Ruebush, I thank you for starting the fire in me and helping me develop not only a joy for chemistry, but a love for learning as well. It's reasonable to say that this is all your fault. J. Brad Dalton III deserves my immense appreciation for making a childhood dream be realized. My summer at the Jet Propulsion Laboratory in 2013 will remain a highlight experience of my life. A special thank you to Corey Jamieson for putting the idea in my head to come to Hawaii, even if it wasn't what you intended. To Ralf Kaiser, for giving me the unique opportunity to merge my interests in astronomy, geology and chemistry through experimental research. It has been an edifying experience. Jeff Gillis-Davis, thank you for your support through this project and providing a well-rounded perspective to the research. To Tom Apple, John Head, and Matthew Cain—a huge mahalo for your encouragement while still having the good sense to push me when it was needed. Marko Förstel, Cheng Zhu, Alex Bergantinni, and Robert Frigge—thanks for being

patient with my incessant questioning and “brilliant” ideas. You’ve saved me from disaster more than once. I’ve enjoyed learning from the diverse ways you each approach a problem, and we’ve shared several good laughs as well. Particularly, I wish to thank Sándor Góbi (and his family, Edina and Nándor). You’ve been a great teacher to me, and an even better friend. Lastly, to my fellow “Lost Boys” Andrew Turner, Matt Abplanalp, and Aaron Thomas. Through our close association over the years, I’m grateful that among us there has always been a spirit of camaraderie and I look forward to seeing where life takes you next.

Most seriously, I wish to memorialize the members of the prestigious institution, Science Huddle: Elizabeth Toller, David Harris, Alina Allen, Elizabeth Nielsen, Steven Fluckiger, McKenna Allen, Griffin Allen, McKenna Gleason, and visiting junior associate, Robyn Lung. May you each live long and prosper.

This research was funded by NASA under Grants NNX14AG39G (R.I.K.), NNX16AO79G, and NNX14AI48G to The University of Hawaii (R. I. K., J. J. G.-D.) as well as the System Exploration Research Virtual Institute (SSERVI) Volatiles Regolith Thermal Investigations Consortium for Exploration and Science (VORTICE) grant to A.P.L. and J.J.G.-D.

ABSTRACT

Remote sensing data and laboratory simulation experiments have demonstrated the dramatic effects space weathering of planetary bodies can have to alter the chemical makeup of planetary surfaces. The dominant weathering processes are affected by the presence of an atmosphere, which effectively shields ionizing radiation in the form of solar wind and micrometeorite impacts. Here, novel laboratory experiments simulating the effects of space weathering agents on the surface of Mars and the Moon are presented. The results aim to assist in the ongoing investigations of three important discoveries made over the last few decades: *First*, the apparent lack of exogenic organic molecules on Mars, *second*, the generation of H₂ molecules in the lunar exosphere, and *third*, the presence of surficial hydroxyl (–OH) groups bound in lunar minerals and exposed water ice deposits at the lunar poles. The systematic approach of these experiments provides important mechanistic details towards the formation of radiogenic molecules on these planetary bodies. In addition, they can be extended to similar environments throughout the Solar System.

TABLE OF CONTENTS

Acknowledgements	ii
Abstract.....	iv
List of Tables	viii
List of Figures.....	ix
Chapter 1 PLANETARY SURFACES	1
1.1 SPACE WEATHERING OF PLANETARY SURFACES	1
1.2 WEATHERING BY CHARGED PARTICLES.....	3
1.2.1 Galactic Cosmic Rays.....	3
1.2.2 Solar Wind	4
1.2.3 Energy Transport of Ions in Solids.....	5
1.3 WEATHERING BY MICROMETEORITE IMPACTS.....	7
1.4 THESIS OVERVIEW	7
1.5 REFERENCES	9
Chapter 2 SOLID STATE MACHINE	13
2.1 EXPERIMENTAL DESIGN.....	13
2.2 VACUUM GENERATION	17
2.3 COLDHEAD OPERATION	20
2.4 IRRADIATION SOURCES	23
2.4.1 Charged Particle Source.....	23
2.4.2 Electron Gun.....	25

2.4.3	<i>Infrared CO₂ Laser</i>	25
2.5	MASS SPECTROMETER	26
2.6	REFERENCES	30
Chapter 3 DEGRADATION OF PERCHLORATES ON MARS BY GCRS		34
3.1	PERCHLORATES AND THE MARTIAN ENVIRONMENT	34
3.2	EXPERIMENTAL DETAILS	37
3.3	RESULTS	45
3.3.1	<i>5 keV D₂⁺ Irradiation</i>	47
3.3.2	<i>5 keV Electron Irradiation</i>	47
3.3.3	<i>Simultaneous Irradiation</i>	48
3.3.4	<i>Sequential Irradiation</i>	49
3.4	DISCUSSION	50
3.4.1	<i>Production Yields</i>	50
3.4.2	<i>O₂ Mass Balance</i>	53
3.4.3	<i>H₂O₂ on Mars</i>	56
3.5	CONCLUSION	59
3.6	REFERENCES	60
Chapter 4 H₂ IN THE LUNAR EXOSPHERE		69
4.1	INTRODUCTION	69
4.2	METHODS	72
4.3	LUNAR ENVIRONMENT SIMULATIONS	75
4.4	ION MICROPROBE ANALYSIS OF IRRADIATED GRAINS	78

4.5	DISCUSSION AND CONCLUSION	82
4.6	REFERENCES	85
Chapter 5	LUNAR WATER FROM SOLAR WIND AND MICROMETEORITES.....	91
5.1	WATER ON THE MOON	91
5.2	METHODS	93
5.2.1	<i>Irradiation of Olivine Samples.....</i>	<i>94</i>
5.2.2	<i>Focused Ion Beam – Scanning Electron Microscopy (FIB-SEM).....</i>	<i>97</i>
5.3	MASS SPECTRA AND VEELS ANALYSIS	98
5.4	THE ROLE OF MICROMETEORITE IMPACTS.....	105
5.5	CONCLUSION.....	110
5.6	REFERENCES	112
Chapter 6	CONCLUSION	120
6.1	SUMMARY OF RESULTS.....	120
6.2	REFERENCES	123
APPENDIX.....	125
A.1	BAKEOUT PROCEDURE	125
A.2	ION GUN OPERATION	129
A.3	ION BEAM ALIGNMENT	133
A.4	ION SELECTION	137

LIST OF TABLES

Table 2.1 Pressures (in Torr) of the differentially pumped regions of the SSM	19
Table 3.1 List and conditions of experiments	40
Table 3.2 Summary of $\text{Mg}(\text{ClO}_4)_2 \cdot 6\text{H}_2\text{O}$ sample preparation by experiment	41
Table 3.3 TRIM and CASINO simulations for the radiolysis of $\text{Mg}(\text{ClO}_4)_2 \cdot 6\text{H}_2\text{O}$	42
Table 3.4 Total molecules produced via radiolysis of $\text{Mg}(\text{ClO}_4)_2 \cdot 6\text{H}_2\text{O}$	51
Table 4.1 Parameters for the ion irradiation source.	73
Table 4.2 Quantified deuterium molecules (N) in the TPD phase.....	78
Table 4.3 Parameters for the quantification of D_2 trapped in samples at 300 K.....	82
Table 5.1 Parameters for irradiation sources	96
Table 5.2 List of experiments	96
Table 5.3 Number of released deuterium and D_2 -water molecules during irradiation	106
Table A.1 Setpoint temperatures for bakeout of SSM.....	128
Table A.2 Example of ion gun parameters used in experiments	131

LIST OF FIGURES

Figure 1.1 Depiction of dominant space weathering processes.	2
Figure 1.2 Polar plots of solar wind speed as a function of latitude	4
Figure 1.3 SRIM simulation showing the range distribution of implanted protons in olivine.	6
Figure 2.1 3D rendering of the Solid State Machine	14
Figure 2.2 Top-down view of the Solid State Machine.	15
Figure 2.3 Pressure/volume relationship during an adiabatic expansion.....	21
Figure 2.4 PV diagram of the four steps involved in a Gifford-McMahon cycle.....	23
Figure 2.5 Image of the Specs 12/38 ion source installed on the Solid State Machine	24
Figure 2.6 Diagram of a quadrupole mass filter..	26
Figure 2.7 Scheme for calibrating the mass spectrometer	29
Figure 3.1 Top view of the experimental setup..	39
Figure 3.2 Output of Monte Carlo simulations showing penetration depth of 5 keV D_2^+ ions	43
Figure 3.3 Ion currents recorded by the QMS during TPD for irradiated samples.	46
Figure 3.4 Depth profile of a sample exposed to both D^+ ions and electrons.....	53
Figure 4.1 Quantification of molecular deuterium detected via $m/z = 4$ signal.	77
Figure 4.2 Backscattered and secondary electron images of an irradiated sample.....	79
Figure 4.3 Depth profiles of $\delta D/^{18}O$ ratios for samples irradiated by D_2^+ ions	80

Figure 4.4 Average D/ ¹⁸ O ratio by depth for irradiated oliving samples.....	81
Figure 5.1 QMS profiles recorded during simulated micrometeorite impact	100
Figure 5.2 Ratio of ion counts recorded at m/z = 20 to m/z = 18.	101
Figure 5.3 STEM image of an ion implanted and laser processed olivine sample.....	103
Figure 5.4 SEM images of ion-implanted and laser-processed olivine grains..	103
Figure 5.5 VEEL spectra an ion implanted and laser processed olivine sample	105
Figure 5.6 Calculated implantation profiles from SRIM of 2.5 keV D ⁺ ions into olivine.....	108
Figure 5.7 Schematic view of olivine irradiated by deuterium ions.	110
Figure A.1 Picture of the SPECS IQE 12/38 charged particle source.	129
Figure A.2 Design of the main chamber faraday cup (MCFC).	133
Figure A.3 Ion beam profile using the MC faraday cup.	134
Figure A.4 Ion beam profile using the RIV faraday cup.	135
Figure A.5 Relative beam currents of ions produced from D ₂ gas.	137

Chapter 1

PLANETARY SURFACES

1.1 Space Weathering of Planetary Surfaces

Space weathering is a term used to encompass any alteration caused by the environment of space to an exposed surface [Bennett, Pirim, and Orlando 2013]. The earliest studies investigating this phenomenon focused on the observed darkening of ancient lunar regolith samples compared to younger, brighter impact craters and ejecta [Barricelli and Metcalfe 1969]. The return of lunar samples from the Apollo missions accelerated our knowledge of the agents responsible for changes in the absorption spectra of lunar minerals, while new effects of space weathering were also discovered. Particularly, it was found that most of the rock samples returned were agglutinates, which exhibit a glassy appearance with small rock fragments and minerals embedded within [Hibbitts et al. 2011]. These were thought to form during a shock-heating and rapid cooling process consistent with a meteoroid impact. However, subsequent laboratory experiments found that the effects of meteoroid impacts could not explain the observed optical properties of small lunar grains [Hapke 2001]. Other observations revealed that regolith grains collected in the upper few centimeters of the surface displayed amorphous rims a few tens of nanometers thick containing nanophase iron particles [Sasaki et al. 2001; Pieters and Noble 2016]. Further *in situ* experiments by Apollo astronauts and remote sensing spacecraft were able to explain these observations by revealing details of the lunar environment. Over the last several decades, similar observations have been on other airless bodies in the Solar System [Rivkin and Emery 2010; Campins et al. 2010; Küppers et al. 2014].

Figure 1.1 provides a pictorial summary of various agents of space weathering for airless planetary surfaces [Pieters and Noble 2016]. The dominant sources of weathering effects greatly depend on the local environment of the surface as the energy fluxes of these processes are not uniform throughout the Solar System. In the case of large terrestrial planets, the effects of micrometeorite bombardment and solar wind implantation are negligible at the surface due to shielding by the atmosphere. In this thesis, we consider the effects of the dominant weathering sources on two examples of planetary bodies in the Solar System: Mars and the Moon. Galactic cosmic ray (GCR) implantation, solar wind exposure, and micrometeorite impacts are discussed in some detail in this chapter, followed by an overview of the experiments that are presented here.

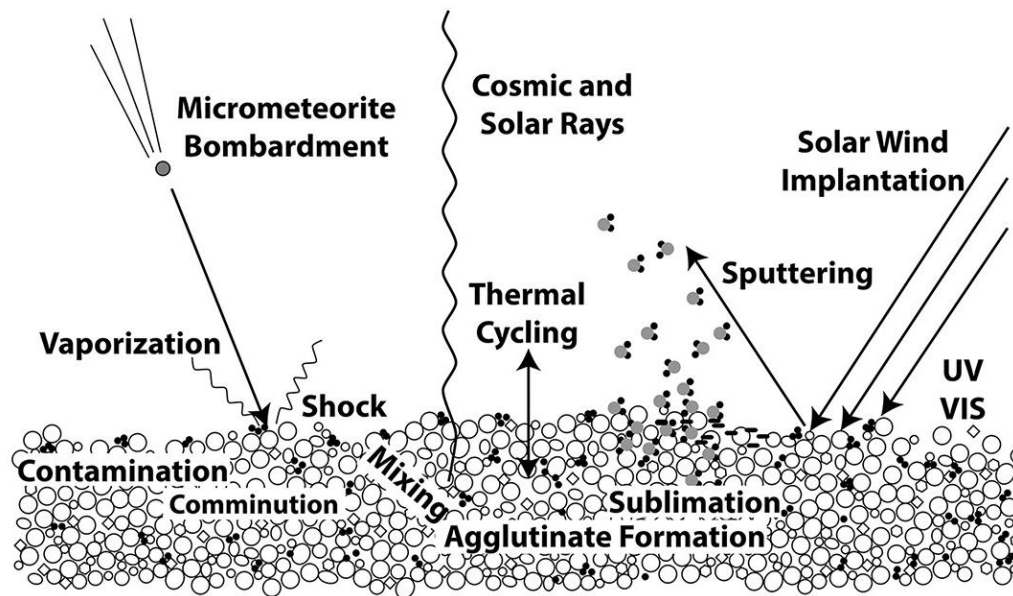


Figure 1.1 Depiction of dominant space weathering processes active across the solar system. Courtesy of Pieters and Noble [2016].

1.2 Weathering by Charged Particles

1.2.1 Galactic Cosmic Rays

Galactic cosmic rays (GCRs) are energetic charged particles originating outside the solar system that have been accelerated to near the speed of light likely through supernova events [Aab et al. 2017]. About 90% of these particles are protons, with another 9% found to be alpha particles (helium nuclei stripped of their electrons). The remaining 1% contain ions of nearly every other element known and are referred to as HZE ions, a reference to their high atomic number (Z) and energy (E) [Chaisson and McMillan 2005]. The energy distribution of these particles varies greatly, from $< 1 \times 10^6$ eV to beyond 1×10^{20} eV, and show a peak in the distribution within the range of 100 MeV to 1 GeV [Carroll and Ostlie 1996]. Due to the presence of strong magnetic fields throughout the galaxy and the solar system, the trajectories of these particles cannot be traced back to their source, making it difficult to study their origin. Thus, the spatial distribution of GCRs is isotropic in the solar system [Binns et al. 2006].

In the case of planetary bodies that exhibit atmospheres (Venus, Earth, Mars, Titan), a constant flux of GCRs travel through the atmosphere towards the surface, bombarding gaseous molecules through predominantly inelastic collisions. This phenomenon results in cascades of secondary particles made up of muons, electrons, positrons, and photons that “shower” down on the surface [Kudela 2009]. While the flux of GCRs is extremely low compared to typical solar wind fluxes at 1 AU, solar wind particles are orders of magnitude lower in energy and do not penetrate through a thick atmosphere. Thus, GCRs can provide a considerable energy flux on atmospheric bodies or on airless bodies in regions of the outer solar system where the solar wind flux is low [Caballero-Lopez and Moraal 2004; Hassler et al. 2014].

1.2.2 Solar Wind

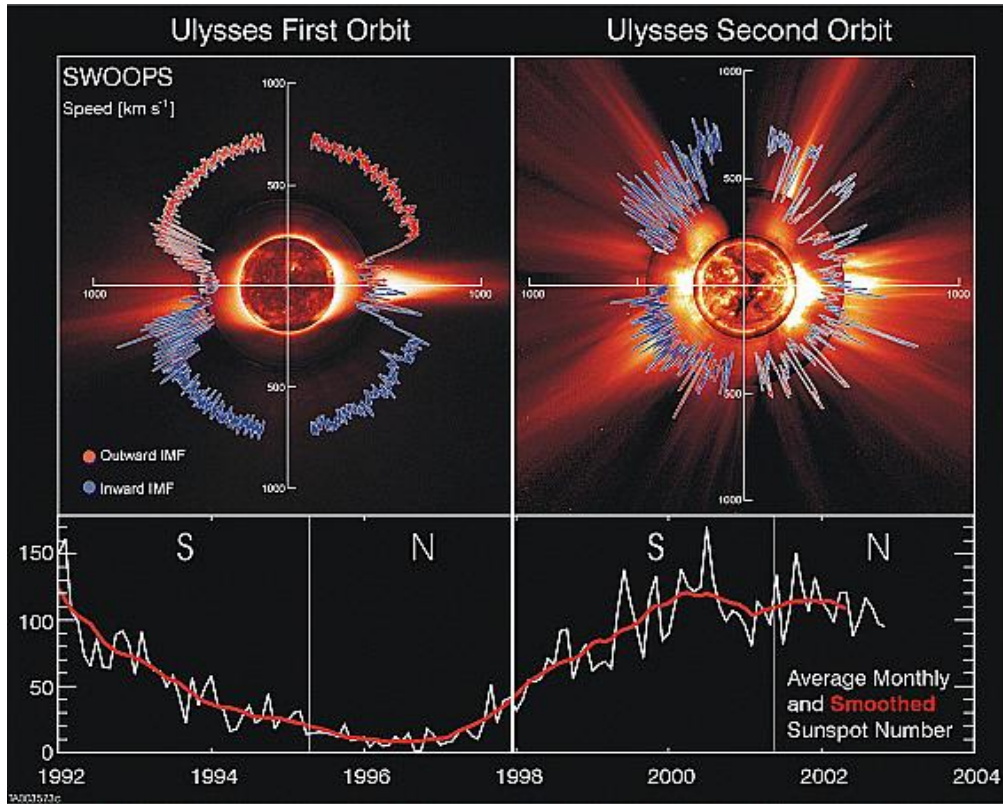


Figure 1.2 Polar plots of solar wind speed as a function of latitude for Ulysses' first two orbits. Sunspot number (bottom panel) shows that the first orbit occurred through the solar cycle declining phase and minimum while the second orbit spanned solar maximum. Both are plotted over solar images characteristic of solar minimum (8/17/96) and maximum (12/07/00). Courtesy of McComas et al. 2003

The solar wind is a torrent of charged particles emanating from the corona of the Sun. Similar to GCRs, the solar wind is primarily composed of protons ($> 90\%$), alpha particles, electrons, and a small percentage as heavy ions [Farrell et al. 2015a]. Unlike GCRs, however, the kinetic energies of these particles are much lower, ranging from a few hundred eV to ~ 10 keV with an average value of 1 keV amu^{-1} . It has also been observed that properties of the solar wind such as density, speed, and temperature vary greatly based on events throughout a solar cycle [McComas and Elliott 2003]. The *Ulysses* probe made the first observations of the solar wind

outside of the ecliptic plane of the Solar System and discovered changes in the solar wind speed as a function of latitude and number of sunspots (Figure 1.2). During solar minima, the probe was at high latitudes and found the average speed of the ions to be relatively fast ($\sim 750 \text{ km s}^{-1}$). At solar maxima, however, the solar wind speed fluctuated to extreme highs and lows due to changes in magnetic field lines surrounding the Sun. Thus, when determining weathering effects of a planetary surface, the variability of solar wind particles must be considered and rationalized. In the following chapters, the solar wind contribution to the weathering of lunar silicates was simulated using deuterium ions implanted into olivine. For these experiments, as well as others referenced in the following chapters, the average flux and near-average energy of H^+ solar wind particles at 1 AU was modeled [Pillinger 1979; Hurley and Farrell 2013; Managadze et al. 2011].

1.2.3 Energy Transport of Ions in Solids

A great portion of the work presented in the following chapters investigates the bombardment of low-energy ions as proxies for solar wind particles and galactic cosmic rays with solid materials serving as planetary surface analogues. These interactions result in morphological changes to the surface by creating defects in the crystal lattice, removing atoms and molecules from the outermost layers, and even induce the destruction and formation of molecular bonds. Generally, “low energy” ions refer to charged atomic and molecular species with energies in the range of 5–15 eV, which is on the same order of bond energies in the bulk solid, as a lower limit up to ions with a kinetic energy of a few keV.

As an ion impinges a solid surface and is implanted, it loses its kinetic energy to the bulk solid through elastic (interactions with nuclei in the crystal lattice) and inelastic (electronic

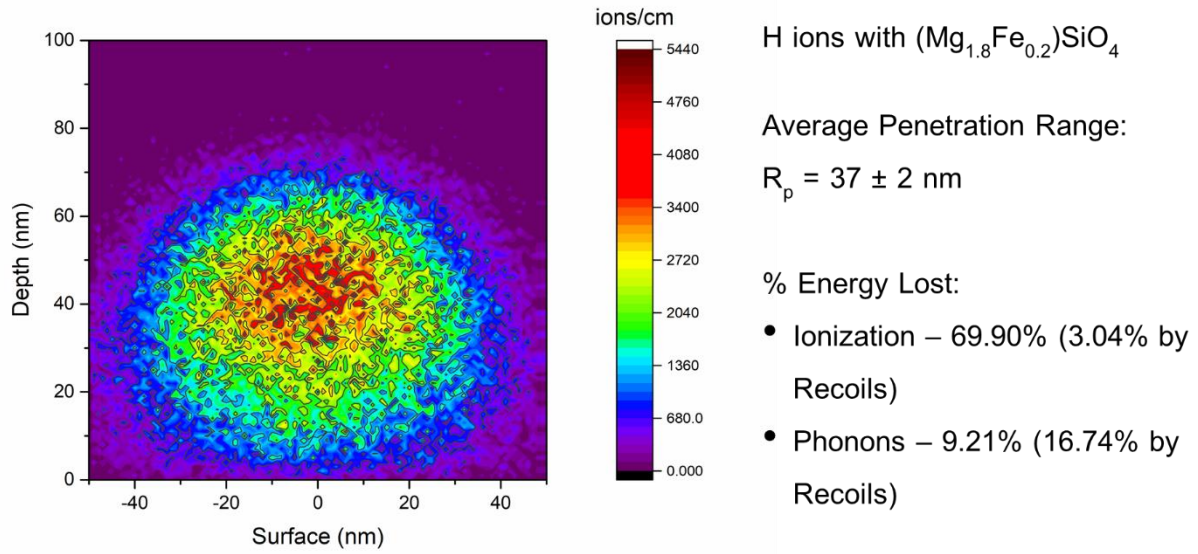


Figure 1.3 SRIM simulation showing the range distribution of implanted protons in olivine.

excitations) collisions. The differential energy loss of a layer in the solid is expressed as a sum of the nuclear (n) and electronic (e) processes by the equation

1.1

$$\frac{dE}{dx} = \left(\frac{dE}{dx}\right)_n + \left(\frac{dE}{dx}\right)_e = -N[S_n(E) + S_e(E)]$$

Where N is the number density of atoms in the sample, and $S_n(E)$ and $S_e(E)$ are the nuclear and electronic stopping cross sections. The derivation of these cross sections is beyond the scope of this chapter but is a function of the interaction potential between the impinging ions and the target atoms well as the nuclear charges. It is sufficient to say that for very light ions, electronic stopping via inelastic collisions dominate in the energy loss of the ion. The Stopping of Ions in Matter (SRIM) code uses a Monte Carlo simulation algorithm to model these collisions in a target solid and results are in very good agreement with experimental conclusions. Thus, the laboratory studies in this thesis are supplemented with SRIM calculations to determine the range (depth profile) of

GCR and solar wind ions as well as to understand recoil effects of the target atoms. Figure 1.3 shows the output of one such simulation, showing a majority of the energy loss of the ions was to ionization events in the solid.

1.3 Weathering by Micrometeorite Impacts

Micrometeorite bombardment is one of the most important processes of space weathering on airless bodies [Hapke 2001; Chapman 2004; Lucey 2006; Pieters and Noble 2016]. Figure 1 shows the mass distribution at 1 AU of the interplanetary meteoroids [Grün et al. 1985]. It is seen that a significant fraction of micrometeorites are particles of 10^{-6} to 10^{-4} g. These small particles have very high-velocities (>10 km s $^{-1}$) and can heat the surfaces of planetary bodies without the protection of an atmosphere up to 104 K upon hitting the surface [Orlando et al. 2018], which results in significant changes in spectral and chemical properties of the surficial material. Laser irradiation experiments have been used widely to simulate micrometeorite impact [Kissel and Krueger 1987; Moroz et al. 1996; Sasaki et al. 2001; Gillis-Davis et al. 2017; Matsuoka et al. 2015]. For example, Moroz et al. [1996] irradiated chondrites with microsecond pulse lasers and detected spectral similarity between S-asteroids and laser processed ordinary chondrites. Additionally, Sasaki et al. [2001] found iron nanoparticles had formed in the amorphous rims of irradiated grains, which are observed in lunar regolith samples returned from the Apollo missions.

1.4 Thesis Overview

In this thesis, several laboratory experiments are presented representing simulated planetary conditions, the results of which reveal new insights to the chemical evolution of these surfaces by space weathering processes. Specifically, the following chapters will first investigate the degradation of perchlorates, a strong oxidizing agent, found ubiquitously on Mars beneath the

Martian surface where GCR irradiation is the dominant weathering source (Chapter 3). 5 keV electrons are used to model the effects of secondary electrons generated by GCRs in the Martian soil while 5 keV D_2^+ ions serve to investigate recombination pathways of reactive hydrogen atoms trapped below the surface after a GCR has been implanted and come to rest.

Secondly, the experiments turn towards simulating weathering conditions on the lunar surface where the solar wind and micrometeorite impacts dominate. Using olivine as a lunar regolith analogue, samples are bombarded with D_2^+ ions (Chapters 4 and 5) as well as exposed to laser radiation to mimic thermal processing from micrometeorites (Chapter 5). The results are compared to findings made from spacecraft data which show the presence of volatile atomic and molecular species forming an exosphere over the lunar surface. Chapter 4 provides a lower limit to the efficiency of the solar wind being converted to molecular hydrogen (H_2) in silicate minerals, Additionally, Chapter 5 demonstrates the first experimental evidence of endogenic water being formed and released from the lunar regolith by both solar wind and micrometeorite weathering effects.

1.5 References

- Aab, A., P. Abreu, M. Aglietta, I. Al Samarai, I. F.M. Albuquerque, I. Allekotte, A. Almela, et al. 2017. “Observation of a Large-Scale Anisotropy in the Arrival Directions of Cosmic Rays above 8×10^{18} eV.” *Science*. doi:10.1126/science.aan4338.
- Barricelli, Nils Aall, and Ralph Metcalfe. 1969. “The Lunar Surface and Early History of the Earth’s Satellite System.” *Icarus* 10 (1). Academic Press: 144–63. doi:10.1016/0019-1035(69)90015-3.
- Bennett, Chris J., Claire Pirim, and Thomas M. Orlando. 2013. “Space-Weathering of Solar System Bodies: A Laboratory Perspective.” *Chemical Reviews*. doi:10.1021/cr400153k.
- Binns, W. R., M. E. Wiedenbeck, M. Arnould, A. C. Cummings, J. S. George, S. Goriely, M. H. Israel, et al. 2006. “Superbubbles, Wolf-Rayet Stars, and the Origin of Galactic Cosmic Rays.” *Journal of Physics: Conference Series*. doi:10.1088/1742-6596/47/1/008.
- Caballero-Lopez, R. A., and H. Moraal. 2004. “Limitations of the Force Field Equation to Describe Cosmic Ray Modulation.” *Journal of Geophysical Research: Space Physics*. doi:10.1029/2003JA010098.
- Campins, Humberto, Kelsey Hargrove, Noemi Pinilla-Alonso, Ellen S. Howell, Michael S. Kelley, Javier Licandro, T. Mothé-Diniz, Y. Fernández, and Julie Ziffer. 2010. “Water Ice and Organics on the Surface of the Asteroid 24 Themis.” *Nature*. doi:10.1038/nature09029.
- Carroll, Bradley W., and Dale A. Ostlie. 1996. *An Introduction to Modern Astrophysics*. An Introduction to Modern Astrophysics, by B.W. Carroll and D.A. Ostlie. Benjamin Cummings, 1996. ISBN 0-201-54730-9.

- Chaisson, Eric, and Steve McMillan. 2005. Astronomy Today. Journal of Chemical Information and Modeling. doi:10.1017/CBO9781107415324.004.
- Chapman, Clark R. 2004. "Space Weathering of Asteroid Surfaces." Annual Review of Earth and Planetary Sciences. doi:10.1146/annurev.earth.32.101802.120453.
- Farrell, W. M., D. M. Hurley, and M. I. Zimmerman. 2015. "Solar Wind Implantation into Lunar Regolith: Hydrogen Retention in a Surface with Defects." Icarus 255: 116–26. doi:10.1016/j.icarus.2014.09.014.
- Gillis-Davis, Jeffrey J., Paul G. Lucey, John P. Bradley, Hope A. Ishii, Heather M. Kaluna, Anumpam Misra, and Harold C. Connolly. 2017. "Incremental Laser Space Weathering of Allende Reveals Non-Lunar like Space Weathering Effects." Icarus. doi:10.1016/j.icarus.2016.12.031.
- Grün, E., H. A. Zook, H. Fechtig, and R. H. Giese. 1985. "Collisional Balance of the Meteoritic Complex." Icarus. doi:10.1016/0019-1035(85)90121-6.
- Hapke, Bruce. 2001. "Space Weathering from Mercury to the Asteroid Belt." Journal of Geophysical Research E: Planets. doi:10.1029/2000JE001338.
- Hassler, Donald M, Cary Zeitlin, Robert F. Wimmer-Schweingruber, Bent Ehresmann, Scot Rafkin, Jennifer L Eigenbrode, David E Brinza, et al. 2014. "Mars' Surface Radiation Environment Measured with the Mars Science Laboratory's Curiosity Rover." Science (New York, N.Y.) 343 (6169): 1244797. doi:10.1126/science.1244797.
- Hibbitts, C. A., G. A. Grieves, M. J. Poston, M. D. Dyar, A. B. Alexandrov, M. A. Johnson, and T. M. Orlando. 2011. "Thermal Stability of Water and Hydroxyl on the Surface of the Moon

- from Temperature-Programmed Desorption Measurements of Lunar Analog Materials.” *Icarus* 213 (1): 64–72. doi:10.1016/j.icarus.2011.02.015.
- Hurley, D. M., and William M. Farrell. 2013. “Solar Wind Fluence to the Lunar Surface.” *Lunar and Planetary Science Conference Proceedings*, no. 2013.
- Kissel, J., and F. R. Krueger. 1987. “Ion Formation by Impact of Fast Dust Particles and Comparison with Related Techniques.” *Applied Physics A Solids and Surfaces*. doi:10.1007/BF00618161.
- Kudela, K. 2009. “On Energetic Particles in Space.” *Acta Physica Slovaca*. doi:10.2478/v10155-010-0098-4.
- Küppers, Michael, Laurence O’Rourke, Dominique Bockelée-Morvan, Vladimir Zakharov, Seungwon Lee, Paul Von Allmen, Benoît Carry, et al. 2014. “Localized Sources of Water Vapour on the Dwarf Planet (1) Ceres.” *Nature*. doi:10.1038/nature12918.
- Lucey, P. 2006. “Understanding the Lunar Surface and Space-Moon Interactions.” *Reviews in Mineralogy and Geochemistry*. doi:10.2138/rmg.2006.60.2.
- Managadze, G.G., V.T. Cherepin, Y.G. Shkuratov, V.N. Kolesnik, and a.E. Chumikov. 2011. “Simulating OH/H₂O Formation by Solar Wind at the Lunar Surface.” *Icarus* 215 (1): 449–51. doi:10.1016/j.icarus.2011.06.025.
- Matsuoka, Moe, Tomoki Nakamura, Yuki Kimura, Takahiro Hiroi, Ryosuke Nakamura, Satoshi Okumura, and Sho Sasaki. 2015. “Pulse-Laser Irradiation Experiments of Murchison CM2 Chondrite for Reproducing Space Weathering on C-Type Asteroids.” *Icarus*. doi:10.1016/j.icarus.2015.02.029.

- McComas, DJ, and HA Elliott. 2003. “The Three-Dimensional Solar Wind Around Solar Maximum.” *Geophysical Research Letters*. doi:10.1029/2003GL017136.
- Moroz, L. V., A. V. Fisenko, L. F. Semjonova, C. M. Pieters, and N. N. Korotaeva. 1996. “Optical Effects of Regolith Processes on S-Asteroids as Simulated by Laser Shots on Ordinary Chondrite and Other Mafic Materials.” *Icarus*. doi:10.1006/icar.1996.0130.
- Orlando, Thomas M, Brant Jones, Carol Paty, Micah J Schaible, John R Reynolds, Phillip N First, Stephen K Robinson, Valeria La Saponara, and Esther Beltran. 2018. “Catalyst: Radiation Effects on Volatiles and Exploration of Asteroids and the Lunar Surface.” *Chem* 4 (1). Elsevier: 8–12. doi:10.1016/j.chempr.2017.12.004.
- Pieters, Carle M., and Sarah K. Noble. 2016. “Space Weathering on Airless Bodies.” *Journal of Geophysical Research: Planets*. doi:10.1002/2016JE005128.
- Pillinger, C. T. 1979. “Solar-Wind Exposure Effects in the Lunar Soil.” *Reports on Progress in Physics* 42 (5): 897–961. doi:10.1088/0034-4885/42/5/003.
- Rivkin, Andrew S., and Joshua P. Emery. 2010. “Detection of Ice and Organics on an Asteroidal Surface.” *Nature*. doi:10.1038/nature09028.
- Sasaki, Sho, Keiko Nakamura, Yoshimi Hamabe, Erika Kurahashi, and Takahiro Hiroi. 2001. “Production of Iron Nanoparticles by Laser Irradiation in a Simulation of Lunar-like Space Weathering.” *Nature*. doi:10.1038/35069013.

Chapter 2

SOLID STATE MACHINE

2.1 Experimental Design

Besides the voyages to the moon during the Apollo era, human exploration of planetary bodies in the solar system remains a future endeavor. Instead, NASA and other space agencies over the last several decades have prioritized robotic missions which rely heavily on remote sensing capabilities to study Earth's celestial neighbors [Hughes 2004]. While there are many advantages to this strategy, launching probes into space is still expensive, time consuming, and dependent on limited resources or components that are prone to malfunction. For these reasons and more, it is expected that experimental research under simulated conditions in the laboratory will always hold a key role in the fields of astrochemistry and planetary science.

The experiments described in the following chapters of this thesis were all conducted in a custom built ultra-high vacuum (UHV) system that collectively is referred to as the Solid State Machine (SSM). The main chamber is a 15 L cylindrical stainless steel (type 304SS) chassis with 9 centro-symmetric CF flange ports used for connecting various components and measurement devices. The samples used in the experiments were loaded onto a substrate that is positioned in the center of the chamber and attached to a CTI-Cryogenics Cryodyne 1020 helium refrigerator, henceforth referred to as the coldhead. This coldhead, in conjunction with a 25 Ω cartridge heater and Model 336 temperature controller (Lakeshore Cryotronics), is used to precisely control the temperature of the sample in the range of 10–320 K. In order to reach temperatures as low as 10 K, special considerations must be taken to ensure proper thermal shielding of the cryogenic system. The main shaft of the coldhead that extends from the differentially-pumped rotatable feedthrough

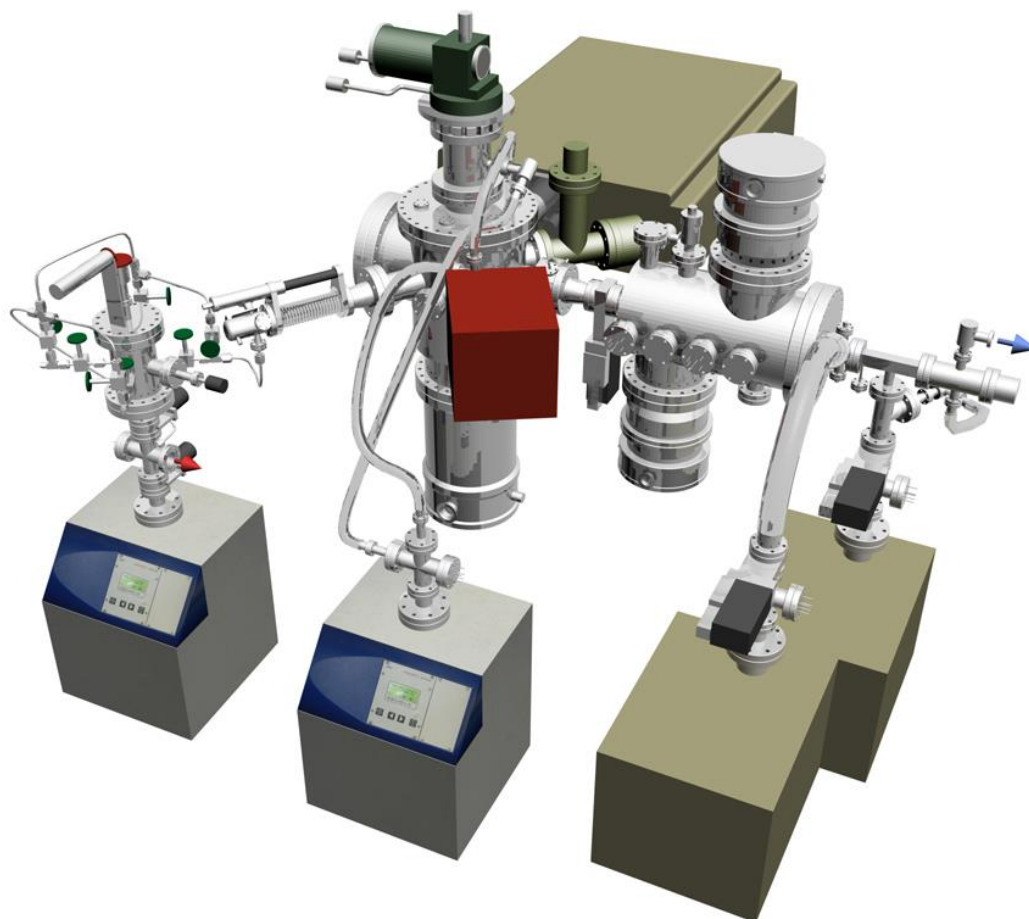


Figure 2.1 3D rendering of the Solid State Machine shown with the differentially pumped regions of the charged particle source. The main chamber (center) is equipped with a freely rotatable feedthrough to allow the sample holder mounted to the coldhead to rotate within the experimental plane.

down to the center of the chamber is concealed by an *oxygen-free high conductance* copper shroud (type OFHC101) to protect the secondary stage of the coldhead and the target from radiative heat transfer from the chamber walls which remain at 298 K. Additionally, a thin film of indium foil (0.1 mm) is sandwiched between the silver substrate that holds the sample and copper holder attached to the end of the coldhead. The indium helps to minimize the effects of heat conduction that can occur if the substrate is in poor contact with the copper mount [Bennett, Jamieson, Mebel, and Kaiser 2004; Jamieson et al. 2005].

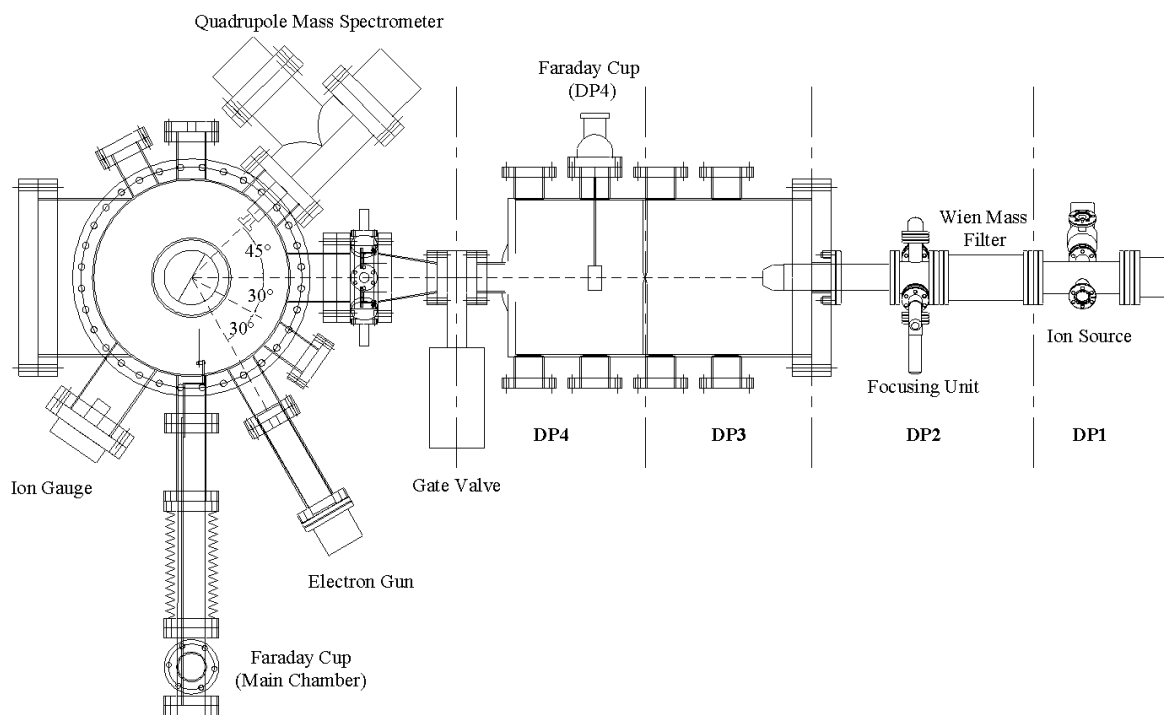


Figure 2.2 Top-down view of the Solid State Machine showing the main chamber and the differentially pumped regions for the ion source (DP 1-4).

Since all experiments were conducted with solid materials, samples were prepared by either crystallizing the substance from a solvent on the silver substrate or crushing the material to a fine powder and pressing it into the silver using a hydraulic press. Afterwards, the substrate was mounted onto the copper target in the main chamber before the chamber was sealed and evacuated to low 10^{-10} Torr for experiments. To reach this pressure, it is necessary to bakeout the entire vacuum system, after the pumps are at full speed, for several days with heating tapes to eliminate residual gases that adhere to the stainless-steel chamber walls. A detailed procedure of evacuating and baking the chamber is found in the appendix.

To carry out an experiment, the sample is cooled to the desired temperature by the coldhead and rotated to the proper orientation for exposure to the irradiation source. The experimental setup features three irradiation sources to simulate space weathering processes: an ion gun (SPECS

12/38) to simulate SCRs and GCRs [Ennis, Bennett, and Kaiser 2011; Bennett, Ennis, and Kaiser 2014a], an electron gun (Specs EQ 22/35) to model secondary electrons generated by high-energy GCRs [Turner et al. 2015; Abplanalp et al. 2015], and a CO₂ laser (SYNRAD Firestar v40) to produce the effects of thermal processing from micrometeorite impacts [Dangi et al. 2015]. The length of time each sample is irradiated is determined beforehand to correspond with an equivalent time period relevant to the system or process of interest. Thus, the rate of energy deposited into the sample over a known time yields an energy dosage typically equivalent to time periods on planetary bodies that are impractical or impossible to directly reproduce, up to millions of years in some cases [Góbi, Abplanalp, and Kaiser 2016; Andrew M. Turner et al. 2015].

During the irradiation phase of the experiment, gases in the main chamber are monitored by a quadrupole mass spectrometer (QMS) with electron impact ionization at 100 eV, running in residual gas analyzer mode. This QMS is equipped with an off-axis (90°) secondary electron multiplier (SEM) detector to allow highly sensitive changes in concentrations of background gasses to be detected (see Section 2.5 for more details). After the irradiation phase, the sample is slowly warmed up from the irradiation temperature to 300 K at a rate of 1 K min⁻¹ while the QMS continues to monitor changes in the residual gases of the chamber. The QMS data collected is always compared to a blank experiment wherein all conditions of the experiment are reproduced except that the sample is not exposed to the irradiation source. The QMS signals that differ from the blank experiment confirm the presence of new products formed as a result of irradiation. While the sample is warming up, these new products will diffuse or sublime out of the sample at a specific temperature, which is useful for characterization of the signals from the QMS. This technique is applied in several other research groups and is commonly referred to as a temperature programmed desorption (TPD) [He et al. 2010; Vidali 2013; Poston et al. 2015]. The remainder of this chapter

will focus on the details and working principles of the mentioned chief components on the Solid State Machine.

2.2 Vacuum Generation

The SSM is supported by an intricate system of dry scroll pumps, membrane pumps, and turbomolecular pumps in order to operate under UHV conditions. These conditions are necessary for the type of surface science experiments detailed in the following chapters. The flux, ϕ ($\text{m}^2 \text{s}^{-1}$), representing the accumulation of gaseous atoms/molecules on a solid surface is a function of the pressure of the gas, the temperature, and the average molecular speed according to the function

2.1

$$\phi = \frac{P\bar{v}}{4k_B T}$$

where \bar{v} is the average molecular speed, P is pressure, k_B is the Boltzmann constant, and T is temperature all in SI units. The molecular speed is a Boltzmann distribution given by

2.2

$$\bar{v} = \sqrt{\frac{8k_B T}{M\pi}}$$

with M being the molar mass of the gas. The experiments presented in this thesis generally require irradiation periods in excess of 10 hours and the irradiation sources are known to penetrate only up to a few hundred nm, depending on the sample. It is reasonable to state from these equations that at experimental pressures above 10^{-5} Torr, over the course of the experiment the residual gas in the chamber would accumulate on the sample surface to such a degree that ionizing radiation

would not be able to penetrate through and reach the sample. With the pressure held at low 10^{-10} Torr however, roughly 2 monolayers of residual gas will accumulate over the surface area of the sample over the course of the experiment, which is a sufficiently low column density.

The operation of the ion source, mentioned in section 2.4.1 of this chapter, presents a difficult problem for sustaining such low pressures in the main chamber. The source chamber of the ion gun requires a high pressure in the range of 10^{-3} Torr to operate a beam current necessary for the experiments. The vacuum system on the main chamber is not capable of pumping at speeds necessary to maintain the desired pressure if the ion gun had been connected directly to a port on the main chamber. Instead, an intricate differential pumping scheme is used to step the pressure down from the ion source chamber to the main chamber (Figure 2.2). The ion gun itself is comprised of two regions that are separated by a small aperture 1 mm in diameter, referred to as regions 1 and 2 (R1, R2). The beam then passes through another small aperture at the end of the deflection plates and enters a much larger chamber that is divided into two sections (R3, R4) by a circular copper gasket with a small aperture drilled in the center. The main chamber can be isolated from the differential pumping regions by closing a gate valve after RIV.

Under molecular flow conditions, small apertures between the regions causes a step down in the baseline pressure due to conductance. This can be considered as a volumetric flow with units of $L\ s^{-1}$. If we imagine a tube or pipe in the vacuum, the conductance is a measure of the pipe's ability to transmit gas molecules from end-to-end in a given time. Since gas molecules tend to "stick" for short periods after colliding with a wall or surface, they do not travel along a reflected trajectory, meaning there is equal probability the gas will travel in any direction after the collision. Thus, a pipe with a small diameter has a lower conductance than a larger pipe due to increased collisions with the surface. Calculating the conductance of an aperture follows the equation

2.3

$$C_{aperture} = d^2 \sqrt{\frac{\pi RT}{32M}}$$

with d being the diameter of the aperture in meters, R is the gas constant, T is temperature, and M is the molar mass of the gas in kg mol^{-1} . The effective pumping speed in each region (S_{eff}) is a function of the pumping speed of the turbopump (S_p) and the conductance of the aperture to the next region as follows:

2.4

$$\frac{1}{S_{eff}} = \frac{1}{S_p} + \frac{1}{C}$$

Finally, the pressure achieved in each differentially pumped region is dependent on the throughput of the gas through the region (Q) and the effective pumping speed:

2.5

$$P = \frac{Q}{S_{eff}}$$

Table 2.1 shows the pressures of each region in a typical experiment while the ion gun was operating. Starting from the ionization source chamber (measured by a cold cathode gauge), the pressure is effectively stepped down in each proceeding region, which allows pressures in the low 10^{-10} to be reached in the main chamber [“Pumping Speed vs Conductance” 2018].

Table 2.1 Pressures (in Torr) of the differentially pumped regions of the SSM

Cold Cathode	R1	R2	R3	R4	MC
2.3×10^{-3}	7.9×10^{-7}	1.5×10^{-7}	2.2×10^{-8}	7.0×10^{-9}	4.7×10^{-10}

2.3 Coldhead Operation

In order to perform analytical experiments at temperatures relevant to surfaces of solar system bodies, the SSM is equipped with a CTI-Cryogenics Cryodyne 1020 coldhead paired with a CTI-Cryogenics 9600 water-cooled compressor. This two-stage Gifford-McMahon (GM) refrigerator is capable of reaching temperatures as low as 50 K at the first stage and 10 K at the second stage. The compressor is used to deliver high pressure helium gas to the coldhead and recycle the gas in a closed loop. Cooling occurs through an adiabatic expansion of the gas, meaning that no heat is lost or gained by the system ($Q = 0$), and the first law of thermodynamics dictates that all the change in internal energy must be in the form of work. The work done by the gas is given by the integral

2.6

$$W = \int_{V_i}^{V_f} P dV$$

Using the adiabatic condition $PV^\gamma = \text{constant}$ (K), where γ is a ratio of the specific heats of the gas (C_p/C_v), then the work integral becomes

2.7

$$W = K \int_{V_i}^{V_f} \frac{dV}{V^\gamma}$$

2.8

$$W = \frac{K(V_f^{1-\gamma} - V_i^{1-\gamma})}{1-\gamma}$$

The final pressure of the gas can be calculated from the adiabatic condition $P_f V_f^\gamma = P_i V_i^\gamma$ and the final temperature is obtained from the ideal gas law

$$T_f = \frac{P_f V_f}{nR}$$

If the initial volume of the expansion space is small, as is the case in a GM cryocooler, one can see from the graph below that there is a nonlinear change in pressure during expansion. The small increase in volume is offset by the large decrease in pressure, causing the temperature to decrease.

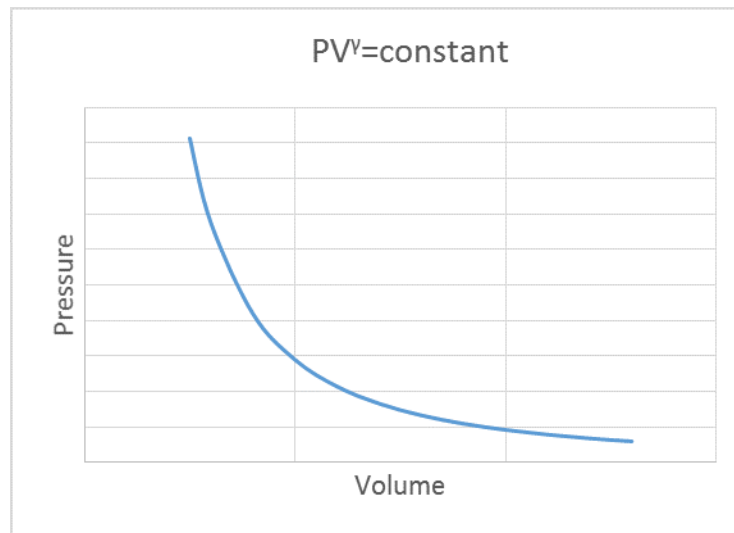


Figure 2.3 Pressure/volume relationship during an adiabatic expansion

For a simple model of how the Gifford-McMahon cycle works, we will first consider a single stage design. The refrigerator is constructed with a freely-suspended displacer contained within a thin-walled stainless steel chamber. The displacer is made of a material with low thermal conductivity to prevent heat transfer between the two volumes it separates at either end of the cylinder. As the displacer moves, gas can travel between these volumes by passing through a regenerator—a porous body, typically cylindrical in shape, made of packed beads or stacked screens oriented perpendicular to the flow direction. Ideally, a constant temperature gradient is maintained across the regenerator such that the gas is cooled as it enters in one direction and is heated as the gas exits in the opposite direction. The cycle proceeds through the following steps:

Step 1-2: With the exhaust valve closed, the helium gas enters the system through the inlet valve at high pressure, P_2 , with the displacer at its lowest position. The pressure in the upper volume and regenerator increases from P_1 to P_2 .

Step 2-3: The inlet valve remains open as the displacer moves up, forcing the gas in the upper volume to move through the regenerator to the lower volume. Due to the temperature gradient in the regenerator created by the previous cycle, the gas is cooled as it passes and more gas can flow through the inlet valve to maintain constant pressure.

Step 3-4: Once the displacer reaches its highest position halfway through the stroke, the inlet valve is closed while the exhaust valve opens simultaneously. This exhaust valve is held at a lower pressure, P_1 , so that when opened, the pressure in the lower volume and regenerator decreases. It is here that the gas in the lower volume undergoes an irreversible adiabatic expansion known as the “Joule-Thompson” effect. While enthalpy remains unchanged, work is done by the gas remaining in the expansion space and there is a decrease in the internal energy, according to the equation $H = U + PV$ (PV increases, so U must decrease). This is the main cooling step.

Step 4-1: As the displacer begins to move down again, the cold gas in the expansion volume is forced out back through the regenerator. Heat is exchanged, and the gas reenters the upper volume at P_1 and near ambient temperature. The regenerator is now precooled for the next cycle.

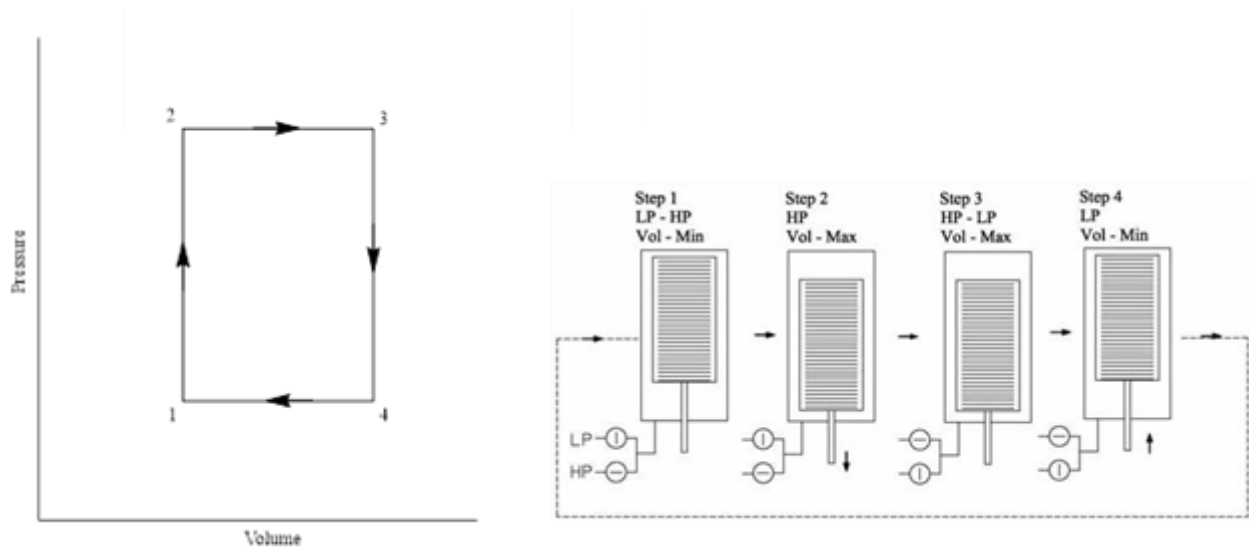


Figure 2.4 (Left) PV diagram of the four steps involved in a Gifford-McMahon cryogenic cycle. (Right) Simplified diagram of a single stage GM cryocooler showing a 2-in-1 displacer/regenerator.

The overall performance of the system is highly dependent on the efficiency of the regenerator. A two stage GM cryocooler, like the one we use, operates through the same cycle described previously, however the second stage is built with a smaller expansion volume which is fed the low temperature gas that leaves the first stage. The displacers for the two stages are locked so that they move in unison. [Gifford 1966; Thirumaleshwar and Subramanyam 1986]

2.4 Irradiation Sources

2.4.1 Charged Particle Source

The SSM is equipped with a SPECS IQE 12/38 ion source for experiments to simulate solar and galactic cosmic protons [Ennis et al. 2011; Ennis and Kaiser 2012; Bennett, Ennis, and Kaiser 2014b]. It has an extractor type ionization chamber that uses an iridium filament coated with yttrium oxide (Y_2O_3) to bombard a gas with energetic electrons. The design of the instrument minimizes the effects of contamination in the ionization chamber compared to other conventional

ion sources, thus allowing for reactive gasses such as O_2 , H_2 , and hydrocarbons to be used in addition to noble gasses. When a pure gas is ionized in the source chamber of the 12/38 ion gun, typically more than one ion species is produced. For this reason, our model is also equipped with a Wien mass filter that allows only a selected *mass-to-charge* ratio to pass through to ensure that the beam produced is free of unwanted ions. The Wien filter works by tuning an electric field held perpendicular to a constant magnetic field produced by a strong magnet. Depending on the molar mass of the gas, there are three separate magnets that can be installed with various strengths. In the following chapters, all experiments were conducted using D_2 gas (99.8%; Icon Isotopes) to form D_2^+ ions.

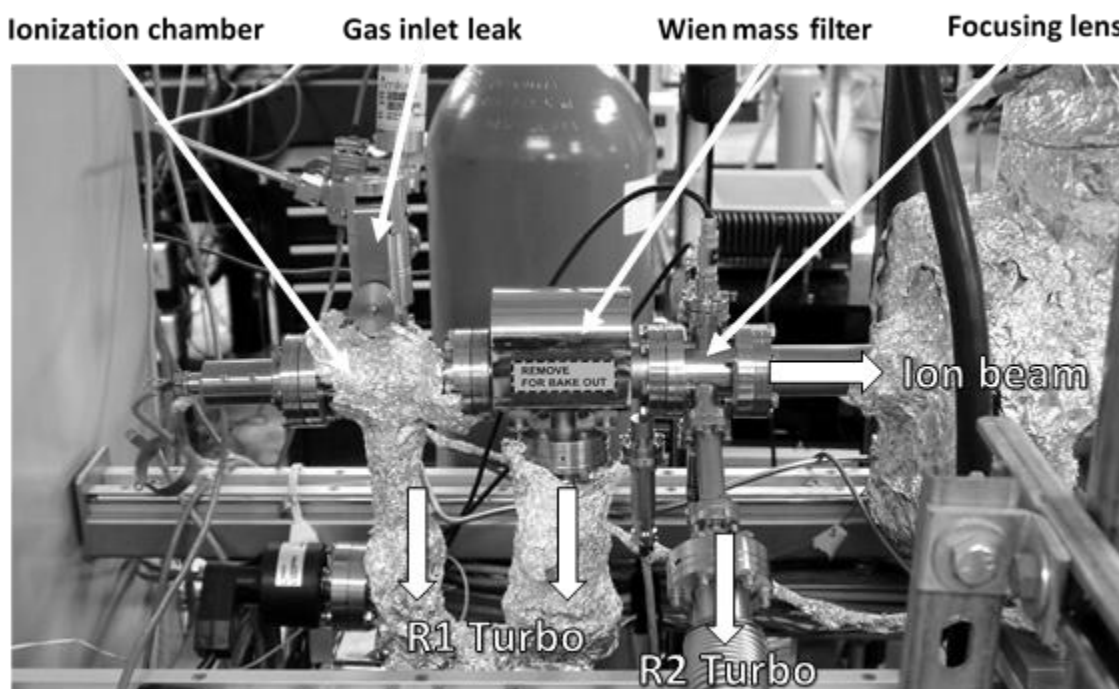


Figure 2.5 Image of the Specs 12/38 ion source installed on the Solid State Machine

2.4.2 Electron Gun

A SPECS EQ22/35 electron source is used in experiments to mimic the effects of secondary electrons that are generated by high-energy (> 1 MeV) galactic cosmic rays in solid targets. 5 keV electrons are emitted from the instrument by heating a tungsten filament with a current of approximately 2.0-2.5 A. The filament itself is negatively biased to accelerate the electrons that are emitted at the desired energy. A Wehnelt extractor sits behind the filament and has a negative voltage applied with respect to the filament potential to fine tune the current of electrons passing the anode aperture into the focusing lens (Einzel lens system). After the electron beam is focused, it passes through deflection plates that can translate the beam in two dimensions to align the beam with the target. Prior to experiments, a phosphor screen was installed on the sample holder to determine the optimized parameters that generated a beam of proper size and alignment.

2.4.3 Infrared CO₂ Laser

Infrared photons (10.6 μm) from a SYNRAD Firestar v40 5 kHz carbon dioxide (CO₂) laser can be used to simulate the effects of micrometeorite impacts on the surface of airless bodies. In the planetary science community, it is well recognized that a CO₂ laser can effectively melt minerals such as olivine to generate chondrule analogues [Cervantes-de la Cruz et al. 2015; Beitz et al. 2013] with microseconds pulse width lasers demonstrated to alter silicate materials [Moroz et al. 1996] and cause lattice disturbance [Kissel and Krueger 1987].

2.5 Mass Spectrometer

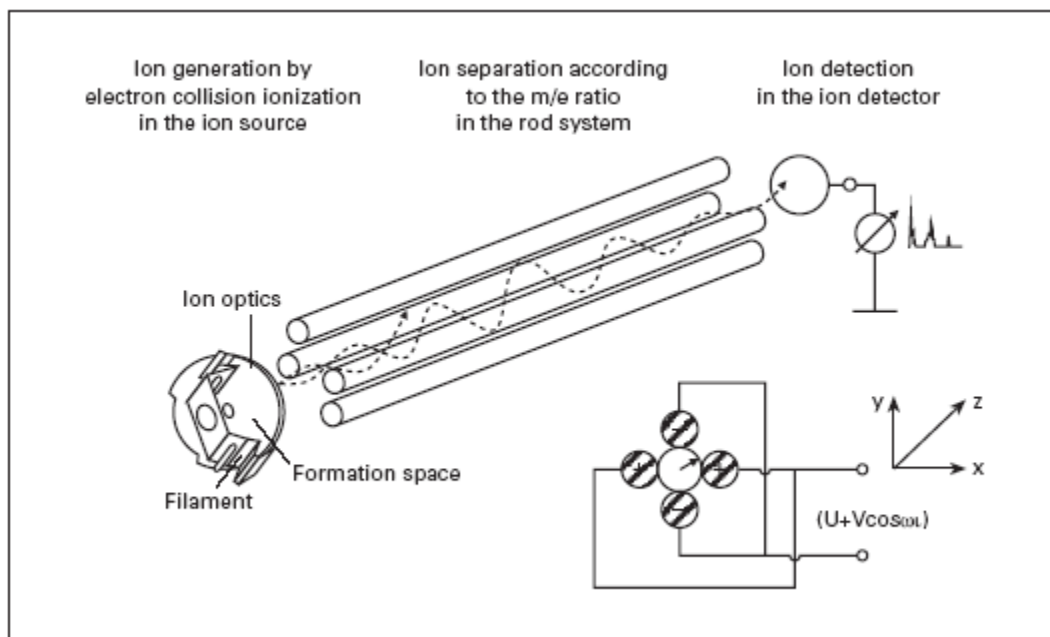


Figure 2.6 Diagram of a quadrupole mass filter. Courtesy of Pfeiffer Vacuum GmbH.

All the experiments described in the following chapters utilize a Pfeiffer Vacuum QMG 422 quadrupole mass spectrometer (QMS) system with a secondary electron multiplier (SEM) detector as the primary instrument for detecting volatile molecules produced from irradiation. The QMS is divided into three main parts: the ion source, the mass filter, and the detector. A brief overview of the working principle for each will be described.

Under UHV conditions, if a gaseous atom or molecule is not pumped out of the system there is a probability that it will come in vicinity of the ion source of the QMS. Our model possesses an axial beam ion source with a rhenium filament that emits electrons with an average energy of 100 eV. A Wehnelt electrode directs the electron flow in the ionization chamber, whereupon they collide with the gas molecules, forming ions. The axial design is useful in that the ions produced

from electron bombardment exhibit a narrow energy distribution, which results in good resolution and high sensitivity of the instrument. This method of electron bombardment is what is sometimes referred to as a “hard” ionization source since the energy of the electrons is one order of magnitude higher than the average energy of a molecular bond. Thus, not only are molecular ions produced and channeled through the instrument, but many molecules are broken up into ion fragments. This results in several signals produced by a single molecule with different *mass-to-charge* ratios. It is still a versatile method, however, since the ionization energies of molecules can differ by several eV and a highly energetic ionization source ensures that all molecules are ionized and can be detected.

After ionization, molecular ions and/or fragments are separated based on their *mass-to-charge* (m/z) ratios by passing through a quadrupole mass filter (Figure 2.6). Here, a combination of radio-frequency (RF) and direct-current (DC) fields with opposite polarities on the pairs of opposing rods create different path oscillations through the rods based on the m/z of the ion. The changing RF field causes the lighter ions to strike the positive poles and the heavier ions to strike the negative poles while allowing only a desired mass to pass through. For our experiments, a dwell time of one second was set, meaning the filter was open for that length of time for each mass of interest. Dwell times can be set to fractions of a μs for faster data acquisition. However, longer dwell times ensures the highest resolution in the data.

The secondary electron multiplier (SEM) of the mass spectrometer is a highly sensitive detector that amplifies the signal of an ion by exploiting a secondary electron cascade across several dynode surfaces. When an ion passes through the quadrupole mass filter and impinges on the first dynode, energetic electrons are released from the surface and are accelerated to the next dynode where additional secondary electrons are released. This continues, and the electron current

increases at every dynode until the last one, whereupon the electrons hit the collector and the current is measured by the electrometer preamplifier. By increasing the voltage of the SEM, the gain of the detector is increased. Overtime, the surfaces of the dynodes deteriorate, which requires the user to increase the SEM voltage to maintain a constant sensitivity.

The quantification of molecules is conducted via calibrating the mass spectrometer for D₂ molecules ($m/z = 4$) before experiments, deriving the absolute number of sublimed D₂ molecules during laser irradiation, and utilizing this value to calculate the sublimed D₂O. Supplementary Figure 2 depicts the scheme for calibrating the mass spectrometer. An Accu-Flow Crimped-Capillary Calibrated Leaks for D₂ molecules (Vacuum Technology Incorporated) was opened to the main chamber for t seconds with leaking rates of $Q = 1.12 \times 10^{-6}$ Torr L s⁻¹ at 298 K. The number of leaked D₂ molecules (n_{D_2}) was calculated using the following formula:

2.10

$$n_{D_2} = \frac{\int_0^t Q dt}{RT}$$

Here, R and T represent the gas constant (62.36 L Torr K⁻¹ mol⁻¹) and temperature (298 K), respectively. The correlation coefficient (K_{QMS}) between the number of D₂ molecules (n_{D_2}) and its molecular ion current ($m/z = 4$, I_{D_2}) profile recorded by QMS was determined by:

2.11

$$K_{QMS} = \frac{n_{D_2}}{\int_0^t I_{D_2} dt}$$

The sublimed D₂ molecules during laser irradiation ($n_{D_2}(\text{IRR})$) was derived based on this coefficient (K_{QMS}) and the $m/z = 4$ signal ($I_{D_2}(\text{IRR})$) using:

2.12

$$n_{D_2}(IRR) = K_{QMS} \int_0^t I_{D_2}(IRR) dt$$

With the electron impact ionization cross sections of D_2 (0.969 \AA) and D_2O (2.348 \AA), the sublimed D_2O molecules during laser irradiation ($n_{D_2O}(IRR)$) was calculated by:

2.13

$$n_{D_2O}(IRR) = \frac{\int_0^t I_{D_2O}(IRR) dt}{\int_0^t I_{D_2}(IRR) dt} \times \frac{0.969 \text{ \AA}}{2.348 \text{ \AA}}$$

where $I_{D_2}(IRR)$ is the D_2O^+ ion current ($m/z = 20$).

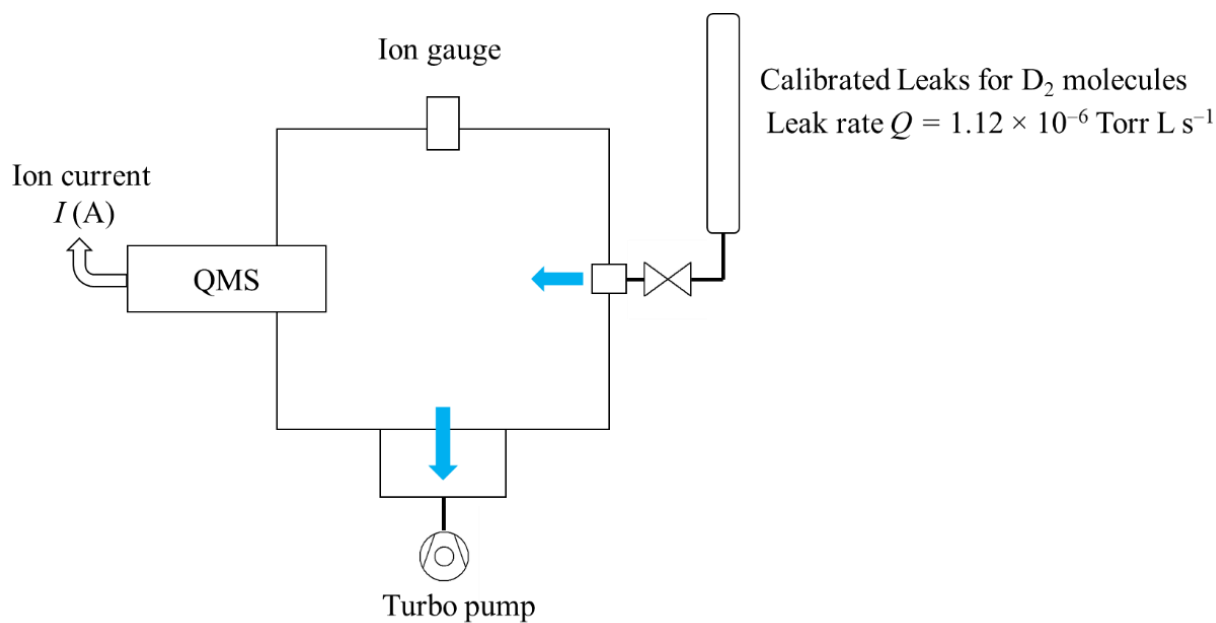


Figure 2.7 Scheme for calibrating the mass spectrometer using an Accu-Flow Crimped-Capillary Calibrated Leaks for deuterium molecules.

2.6 References

- Abplanalp, Matthew J., Aleca Borsuk, Brant M. Jones, and Ralf I. Kaiser. 2015. “On the Formation and Isomer Specific Detection of Propenal (C_2H_3CHO) and Cyclopropanone ($C-C_3H_4O$) in Interstellar Model Ices—a Combined Ftir and Reflectron Time-of-Flight Mass Spectroscopic Study” *The Astrophysical Journal* 814 (1). IOP Publishing: 45. doi:10.1088/0004-637X/814/1/45.
- Beitz, E., J. Blum, R. Mathieu, A. Pack, and D. C. Hezel. 2013. “Experimental Investigation of the Nebular Formation of Chondrule Rims and the Formation of Chondrite Parent Bodies.” *Geochimica et Cosmochimica Acta*. doi:10.1016/j.gca.2012.04.059.
- Bennett, Chris J., Courtney P. Ennis, and Ralf I. Kaiser. 2014a. “Experimental Studies on the Formation of D_2O and D_2O_2 By Implantation of Energetic D^+ Ions Into Oxygen Ices.” *The Astrophysical Journal* 782 (2): 63. doi:10.1088/0004-637X/782/2/63.
- Bennett, Chris J., Courtney P. Ennis, and Ralf I. Kaiser. 2014b. “Implantation of Energetic D^+ Ions into Carbon Dioxide Ices and Implications for Our Solar System: Formation of D_2O and D_2CO_3 .” *The Astrophysical Journal* 794 (1): 57. doi:10.1088/0004-637X/794/1/57.
- Bennett, Chris J., C. Jamieson, Alexander M. Mebel, and Ralf I. Kaiser. 2004. “Untangling the Formation of the Cyclic Carbon Trioxide Isomer in Low Temperature Carbon Dioxide Ices.” *Physical Chemistry Chemical Physics*. doi:10.1039/b315626p.
- Cervantes-de la Cruz, Karina E., Fernando Ortega Gutiérrez, Jesús Solé Viñas, Antígona Segura Peralta, Margarita Adela Reyes Salas, Blanca Sonia ángeles García, María del Consuelo Macías Romo, and Carlos Linares-López. 2015. “Experimental Chondrules by Melting

- Samples of Olivine, Clays and Carbon with a CO₂ laser.” *Boletín de La Sociedad Geológica Mexicana*. doi:10.18268/BSGM2015v67n3a4.
- Dangi, Beni B., Yong S. Kim, Serge A. Krasnokutski, Ralf I. Kaiser, and Charles W. Bauschlicher. 2015. “Toward the Formation of Carbonaceous Refractory Matter in High Temperature Hydrocarbon-Rich Atmospheres of Exoplanets Upon Micrometeoroid Impact.” *Astrophysical Journal* 805 (1). doi:10.1088/0004-637X/805/1/76.
- Ennis, Courtney, Chris J. Bennett, Brant M. Jones, and Ralf I. Kaiser. 2011. “Formation of D₂-Water and D₂-Carbonic Acid in Oxygen-Rich Solar System Ices via D₂⁺ Irradiation.” *Astrophysical Journal* 733 (2). doi:10.1088/0004-637X/733/2/79.
- Ennis, Courtney, and Ralf I. Kaiser. 2012. “On the Formation of Ozone in Solar System Oxygen Ices Exposed To Heavy Ions.” *The Astrophysical Journal* 745 (2): 103. doi:10.1088/0004-637X/745/2/103.
- Ennis, Courtney P., Chris J. Bennett, and Ralf I. Kaiser. 2011. “On the Formation of Ozone in Oxygen-Rich Solar System Ices via Ionizing Radiation.” *Physical Chemistry Chemical Physics* 13 (20): 9469–82. doi:10.1039/c1cp20434c.
- Gifford, W. E. 1966. “The Gifford-McMahon Cycle.” In *Advances in Cryogenic Engineering*, 152–59. doi:10.1007/978-1-4757-0522-5.
- Góbi, Sándor, Matthew J. Abplanalp, and Ralf I. Kaiser. 2016. “Effect of Perchlorates on Electron Radiolysis of Glycine With Application To Mars.” *The Astrophysical Journal* 822 (1): 8. doi:10.3847/0004-637X/822/1/8.
- He, Jiao, Kun Gao, Gianfranco Vidali, Chris J. Bennett, and Ralf I. Kaiser. 2010. “Formation of Molecular Hydrogen From Methane Ice.” *The Astrophysical Journal* 721 (2): 1656–62.

doi:10.1088/0004-637X/721/2/1656.

Hughes, David W. 2004. "Voyage To The Planets: Remote Sensing." *The Open University*.

<https://www.open.edu/openlearn/science-maths-technology/science/physics-and-astronomy/astronomy/voyage-the-planets-remote-sensing>.

Jamieson, Corey S., Chris J. Bennett, Alexander M. Mebel, and Ralf I. Kaiser. 2005. "Investigating the Mechanism for the Formation of Nitrous Oxide [N_2O ($X^1\Sigma^+$)] in Extraterrestrial Ices." *The Astrophysical Journal* 624 (1): 436–47. doi:10.1086/428933.

Kissel, J., and F. R. Krueger. 1987. "Ion Formation by Impact of Fast Dust Particles and Comparison with Related Techniques." *Applied Physics A Solids and Surfaces*. doi:10.1007/BF00618161.

Moroz, L. V., A. V. Fisenko, L. F. Semjonova, C. M. Pieters, and N. N. Korotaeva. 1996. "Optical Effects of Regolith Processes on S-Asteroids as Simulated by Laser Shots on Ordinary Chondrite and Other Mafic Materials." *Icarus*. doi:10.1006/icar.1996.0130.

Poston, Michael J., Gregory A. Grieves, Alexandr B. Aleksandrov, Charles A. Hibbitts, M. Darby Dyar, and Thomas M. Orlando. 2015. "Temperature Programmed Desorption Studies of Water Interactions with Apollo Lunar Samples 12001 and 72501." *Icarus* 255 (0): 24–29. doi:<http://dx.doi.org/10.1016/j.icarus.2014.09.049>.

"Pumping Speed vs Conductance." 2018. *Kurt J. Lesker Company*. https://www.lesker.com/newweb/technical_info/vacuumtech/conductance_01_psvsconductance.cfm.

Thirumaleshwar, M., and S. V. Subramanyam. 1986. "Gifford-McMahon Cycle - a Theoretical Analysis." *Cryogenics* 26 (3): 177–88. doi:10.1016/0011-2275(86)90217-1.

- Turner, Andrew M., Matthew J. Abplanalp, Si Y. Chen, Yu T. Chen, Agnes H. H. Chang, and Ralf I. Kaiser. 2015. "A Photoionization Mass Spectroscopic Study on the Formation of Phosphanes in Low Temperature Phosphine Ices." *Phys. Chem. Chem. Phys.* 17 (41). Royal Society of Chemistry: 27281–91. doi:10.1039/C5CP02835C.
- Vidali, Gianfranco. 2013. "H₂ Formation on Dust Grains." *Chemical Reviews* 113: 8762–82.

Chapter 3

DEGRADATION OF PERCHLORATES ON MARS BY GCRS

This chapter is based on the published paper: P. B. Crandall, S. Góbi, J. Gillis-Davis, and R. I. Kaiser, Can perchlorates be transformed to hydrogen peroxide (H_2O_2) products by cosmic rays on the Martian surface?, J. Geophys. Res. Planets, 122, 1880-1892 (2017)

3.1 Perchlorates and the Martian Environment

The discovery of perchlorates, first at the Phoenix lander site in the northern Martian plains [Hecht et al. 2009] and later by the Curiosity rover in Gale Crater [Glavin et al. 2013], garnered particular interest from the Mars surface chemistry community because the perchlorate anion (ClO_4^-) is known to be a strong oxidizing agent that could play a role in the destruction of organic molecules within the regolith [Steininger et al. 2012; Carrier and Kounaves 2015]. Whether conditions on the planet ever favored the in situ formation of organic molecules remains unknown, however, a model by Flynn and McKay [1990] estimated that between 1.63×10^{-6} to 7.36×10^{-8} kg m⁻² of meteoritic material reach the surface per year. Meteorite samples discovered on Earth, such as the Murchison meteorite, have been found to contain 1-4 % of organic matter, including amino acids, and it is reasonable to extrapolate that these meteorites also deliver exogenously prebiotic molecules to the Martian surface unharmed [Oro and Holzer 1980]. Referencing the model by Flynn and McKay, Ten Kate et al. [2005] calculated an annual flux of about 15 ng m⁻² yr⁻¹ of unaltered amino acids and other organic molecules—a rate that should produce detectable ppb-level concentrations after a geologically short time period of about 1000 years. In 2015, analysis of drill sample data from the Sample Analysis at Mars (SAM) instrument, on board the Curiosity Rover, revealed that elevated levels of chlorobenzene and C₂ to C₄ dichloroalkanes could

not be explained by known instrument background sources; thus, the presence of organic molecules in the Martian soil was confirmed [Freissinet et al. 2015]. However, the abundance of this organic carbon is still well below what is predicted based on current models.

Several hypotheses exist to explain the apparent degradation of organics at or near the surface of Mars [Yen et al. 2000; Shkrob, Chemerisov, and Marin 2010; Poch et al. 2015]; the most widely accepted of these is the presence of oxidative reagents in the regolith such as perchlorates [Ming et al. 2009; Navarro-González et al. 2010]. These inorganic salts have been found at levels of 0.4–0.6 wt. % [Archer and Franz 2013] and are believed to form homogeneously across the Martian surface by means of photocatalytic [Carrier and Kounaves 2015], photooxidative [Schuttlefield et al. 2011], photochemical [Catling et al. 2010], or radiative processes [Kim et al. 2013; Wilson et al. 2016]. Mars' thin, tenuous atmosphere and lack of a strong global magnetic field leave its surface greatly exposed to ionizing radiation. Laboratory experiments investigating the relative importance of these five processes under simulated Martian conditions provide convincing evidence that even complex organic molecules, such as amino acids, are effectively destroyed at faster rates than they can accumulate when in the presence of oxidizing agents, like perchlorates, and exposed to ultraviolet (UV) photons [Oro and Holzer 1980; Stoker and Bullock 1997; Ten Kate et al. 2006] or galactic cosmic ray (GCR) particles [Pavlov et al. 2012; Góbi et al. 2016a; Góbi et al. 2017a]. Hence, UV and GCR radiation are important factors to consider as these energies can drive chemical processes [Pavlov et al. 2012].

We consider now the relative importance between GCRs and UV photons. GCRs provide the most suitable explanation for the destruction of organics beneath the uppermost layer of the surface, despite having an energy flux four orders of magnitude lower than the energy flux of solar photons, because UV photons are completely absorbed within the top few monolayers of the

regolith dust [Muñoz-Caro et al.2006]. Hence, while UV photons are 10,000 times more abundant, GCRs penetrate 1 million times deeper. Pavlov et al. [2012] calculated that solar cosmic rays (SCRs) and GCRs with energies greater than 1 MeV and 20 MeV, respectively, have sufficient kinetic energy to penetrate Mars' tenuous carbon dioxide (CO₂) atmosphere and will reach the surface. These particles can be implanted to depths of up to 2 m. This work concludes by estimating a dosage of 0.07 Gy yr⁻¹ at the surface—a value validated by the Radiation Assessment Detector (RAD) instrument on board the Curiosity Rover—and provides a model for estimating the dose as a factor of depth. Even at depths of 5–10 cm, organic material would decompose under these conditions within 300 Myr.

Having established that GCRs play a vital role in the destruction of organic material beneath the Martian surface and bearing in mind the ubiquitous presence of perchlorates at 0.4–0.6 wt.%, it is crucial to first understand the degradation mechanisms of perchlorates by GCRs before a complete mechanism of the oxidation of organics by perchlorates can be realized. Previous experiments by Turner et al. [2016], conducted at Mars relevant conditions, revealed that irradiation of magnesium perchlorate hexahydrate (Mg(ClO₄)₂·6H₂O) by energetic electrons, which simulated secondary electrons generated by GCRs [Bennett et al. 2005], resulted in the cleavage of a single chlorine–oxygen (Cl–O) bond within the perchlorate anion (ClO₄⁻) to yield the chlorate anion (ClO₃⁻) and atomic oxygen (O). Two O atoms could then recombine to form molecular oxygen (O₂). These findings were further confirmed by a single photon photoionization reflectron time-of-flight mass spectrometric study that was able to detect chlorine dioxide (ClO₂) as a higher order product, which may act as an even more effective oxidizer than molecular oxygen (O₂) formed upon the electron radiolysis of perchlorates. Furthermore, the presence of metastable chlorine oxides (Cl_xO_y, x = 1–2, y = 1–7) was inferred in irradiated magnesium perchlorate

hexahydrate ($\text{Mg}(\text{ClO}_4)_2 \cdot 6\text{H}_2\text{O}$) samples [Góbi et al. 2016b]. This suggests that organics below the surface may not be oxidized by perchlorates alone, but by molecular oxygen (O_2) along with chlorine oxides released from these salts upon bombardment by either GCRs or by secondary electrons of these GCRs.

Here we extend the state of knowledge pertaining to destruction of organics in Martian soils by discussing a set of laboratory experiments designed to investigate the degradation products of solid hydrated perchlorates — specifically magnesium perchlorate hexahydrate ($\text{Mg}(\text{ClO}_4)_2 \cdot 6\text{H}_2\text{O}$) — formed within the tracks of GCRs. Samples were exposed to monoenergetic beams of electrons — once again simulating the secondary electrons in the track of GCRs — and molecular deuterium ions (D_2^+) separately, sequentially, and simultaneously to explore the radiation effects from both GCRs directly and the secondary electrons they produce [Kaiser and Roessler 1997; Jones et al. 2011]. We provide compelling evidence that upon delivering its kinetic energy to the minerals, a GCR, in the form of a proton (H^+), participates after neutralization in the formation of a new oxidizing species — hydrogen peroxide — that may play a role in the oxidative degradation of organics on Mars.

3.2 Experimental Details

The experiments were conducted within a stainless steel ultra-high vacuum (UHV) chamber that was evacuated to $1.5 \pm 0.5 \times 10^{-10}$ torr using oil-free turbomolecular pumps backed by dry scroll pumps [Bennett et al. 2004] (Figure 3.1). Magnesium perchlorate hexahydrate ($\text{Mg}(\text{ClO}_4)_2 \cdot 6\text{H}_2\text{O}$, Sigma Aldrich, 99.0+%) samples were prepared on a polished silver substrate measuring $31.5 \times 31.5 \text{ mm}^2$ that was mounted onto a rotatable copper cold finger attached to a two-stage, closed-cycle helium cryocooler (CTI-Cryogenics Cryodyne 1020, compressor: CTI-

Cryogenics 9600). A thin layer of indium foil was placed between the silver substrate and the cold finger to ensure good thermal conductivity. A Lakeshore DT-470 silicon diode sensor fixed to the cold finger near the substrate was used to monitor the temperature of the sample, which can be controlled within the range of 11–320 K by a 50 Ω heater cartridge powered by a Lakeshore 331 temperature controller.

The sample was cooled to 50.0 ± 0.5 K whereupon it was irradiated by either singly charged molecular deuterium ions (D_2^+), electrons (e^-), or both (Table 3.1). An electron gun (SPECS EQ 22/35) generated the electron beam [Zheng, Jewitt, and Kaiser 2006b], while an ion source (SPECS IQE 12/38), supplied with a 3.0×10^{-3} torr base pressure of high-purity molecular deuterium gas (D_2 : 99.8%; Icon Isotopes), produced the charged particle beam. Located after the ionization and extraction regions of the ion source, a Wien mass filter separated unwanted atomic deuterium (D^+) and trideuterium (D_3^+) ions to produce a monoenergetic beam of 5 keV molecular deuterium ions (D_2^+) directed at the substrate [C. Ennis et al. 2011]. After passing through the mass filter, ions travel through three additional differentially pumped regions, which are in place to maintain a pressure of low 10^{-10} torr in the main chamber while the ion source is in operation. A Faraday cup in the last differentially pumped region (DP4 in Figure 3.1) was used to align the beam to the target, where the spot size was about 1.4 cm^2 , while a second Faraday cup in the main chamber measured the total ion current of either the ions or electrons in front of the sample. During the irradiation, a Balzer QMG 422 electron impact quadrupole mass spectrometer (EI-QMS—operating in residual gas analyzer mode with electron impact energy of 100 eV at a 0.7 mA emission current) monitored any species escaping from the sample. After irradiation, the sample is held isothermally for one hour before being heated to 300 K at a rate of 0.5 K min^{-1} while the

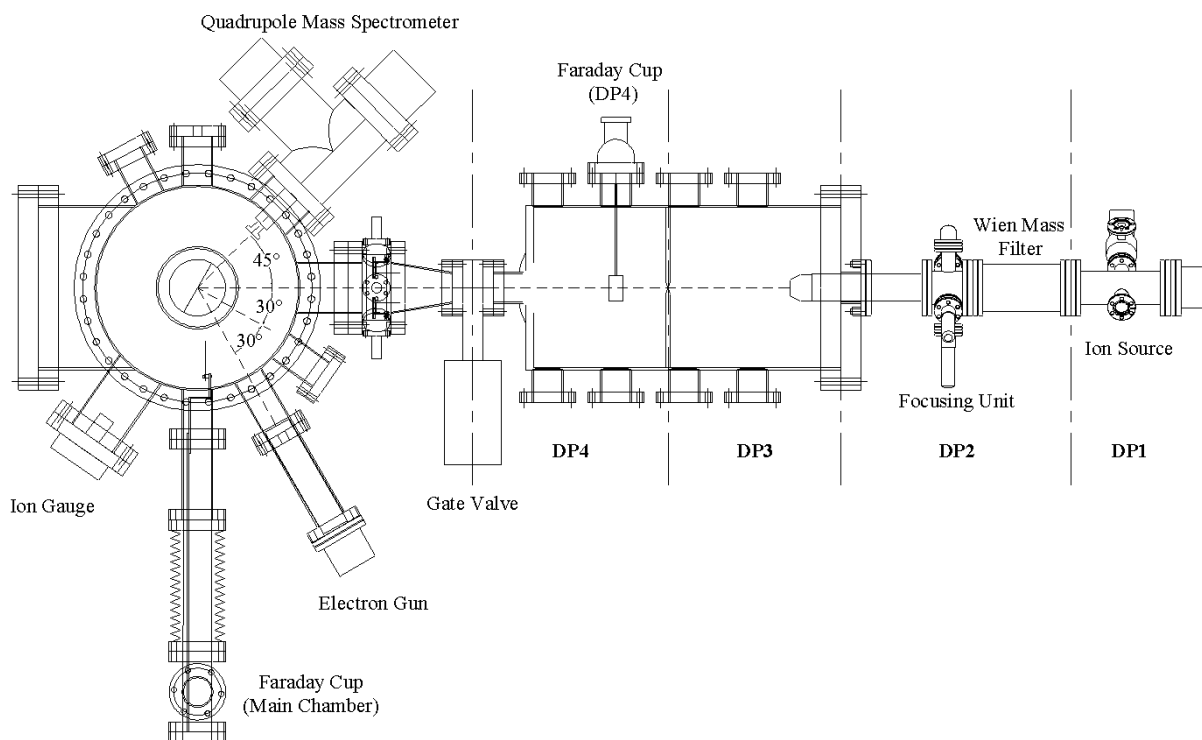


Figure 3.1 Top view of the experimental setup. The differentially pumped (DP) regions of the ion source are indicated.

QMS continues to analyze subliming products during the temperature programmed desorption (TPD). Once 300 K is reached, the sample is again held isothermal for an additional 8 hours to allow products to diffuse out of the solid sample.

At this point, a brief explanation is required for our justification in using molecular deuterium ions (D_2^+) to model GCRs in our experiments. As mentioned previously, the intent of this work is to observe the role of GCRs in the formation of new chemical species when interacting with perchlorates. Since GCRs are approximately 90% protons [Hassler, Zeitlin, Wimmerschweingruber, et al. 2014; Köhler et al. 2016], it is useful to employ deuterium ions (D^+), as the products formed by the incident ions would be isotopically labeled and could not be mistaken as contamination from residual water (H_2O). However, upon ionizing gaseous molecular deuterium (D_2) in the source chamber, the formation of molecular deuterium ions (D_2^+) is highly favored over

D^+ nearly two orders of magnitude. Sigmund et al. [1996] emphasized that “implant profiles of keV diatomic molecular ions are, by and large, equivalent with those of monoatomic ion beams at twice the fluence and half the energy.” While there are considerable limitations to this linear approximation [Arista 2000], nonlinear effects are observed to increase with molecular ion mass. Considering the ‘light’ deuterium, it can therefore be reasonably approximated that for the 5 keV molecular deuterium ions (D_2^+) impinging on a solid target, the molecular ion is dissociated upon impact forming a deuterium ion (D^+) and a D atom, each possessing 2.5 keV of translational energy on average. It should be stressed that no laboratory experiment can precisely simulate the interaction of GCRs/SCRs with the Martian surface. The energy distribution of these particles cover energies spanning several orders of magnitude [Pavlov et al. 2012] and there is no ion source that can provide such a dynamic range. The same is true for modeling secondary electrons produced via electron cascades from a cosmic ray entering the top of the Martian atmosphere. At Mars orbit, the energy distribution of GCRs peaks around 1 GeV [Molina-Cuberos 2001] and much of this energy is lost through ionization events as the GCR travels through the CO_2 atmosphere before being implanted in the regolith. Hence, by selecting beams with an energy of 5 keV, we are effectively simulating the terminal track of GCRs as they come to rest within the Martian soil.

Table 3.1 List and conditions of experiments

Irradiation	Current (μA)	Time (hrs)
Blank	0.0	10
Sole source: D_2^+	2.0	10
Sole source: e^-	2.0	10
Simultaneous: $D_2^+ + e^-$	2.0 each	10
Simultaneous: $D_2^+ + e^-$	2.0 each	100
Sequential: e^- followed by D_2^+	2.0 each	10 each (20 total)
Sequential: D_2^+ followed by e^-	2.0 each	10 each (20 total)

Table 3.2 Summary of magnesium perchlorate hexahydrate ($\text{Mg}(\text{ClO}_4)_2 \cdot 6\text{H}_2\text{O}$) sample preparation by experiment

	D_2^+	e^-	$\text{D}_2^+ + \text{e}^-$ (10 hr)	$\text{D}_2^+ + \text{e}^-$ (100 hr)	$\text{e}^- \rightarrow \text{D}_2^+$	$\text{D}_2^+ \rightarrow \text{e}^-$
Mass of $\text{Mg}(\text{ClO}_4)_2 \cdot 6\text{H}_2\text{O}$ weighed (mg)	249.3 ± 0.1	250.7 ± 0.1	251.6 ± 0.1	248.9 ± 0.1	251.0 ± 0.1	247.9 ± 0.1
Mass of solvent H_2O (g)	15.0331 ± 0.0001	15.0427 ± 0.0001	15.0281 ± 0.0001	14.9926 ± 0.0001	14.9846 ± 0.0001	15.0134 ± 0.0001
Volume of solution used (mL)	0.700 ± 0.005	0.700 ± 0.005	0.700 ± 0.005	0.700 ± 0.005	0.700 ± 0.005	0.700 ± 0.005
Mass of $\text{Mg}(\text{ClO}_4)_2 \cdot 6\text{H}_2\text{O}$ added to substrate (mg)	11.6 ± 4.2	11.7 ± 4.2	11.7 ± 4.2	11.6 ± 4.2	11.7 ± 4.3	11.6 ± 4.2
Density of film (g cm^{-3})	1.98 ± 0.03	1.98 ± 0.03	1.98 ± 0.03	1.98 ± 0.03	1.98 ± 0.03	1.98 ± 0.03
Average Thickness (μm)	6.0 ± 2.2	6.0 ± 2.2	6.0 ± 2.2	6.0 ± 2.2	6.0 ± 2.2	6.0 ± 2.2
Number of molecules in sample ($\times 10^{19}$)	2.11 ± 0.76	2.12 ± 0.77	2.13 ± 0.77	2.11 ± 0.77	2.13 ± 0.77	2.10 ± 0.76

Table 3.3 Summary of TRIM and CASINO simulations for the radiolysis of magnesium perchlorate hexahydrate ($\text{Mg}(\text{ClO}_4)_2 \cdot 6\text{H}_2\text{O}$)

	aD^+		e^-		$\text{D}^+ + \text{e}^-$		$\text{D}^+ + \text{e}^-$	
	Ions	Electrons	Ions	Electrons	Ions	Electrons	Ions	Electrons
Angle of incidence ($^\circ$)	30	-30	-30	-30	30	-30	30	-30
Irradiated area (cm^2)	1.4 ± 0.2	0.46 ± 0.02	0.46 ± 0.02	0.46 ± 0.01	1.4 ± 0.2	0.46 ± 0.01	1.4 ± 0.2	0.46 ± 0.01
Irradiation time (s)	36000 ± 2	36000 ± 2	36000 ± 2	36000 ± 2	36000 ± 2	36000 ± 2	36000 ± 2	36000 ± 2
Applied current (μA)	2.0 ± 0.1	2.0 ± 0.1	2.0 ± 0.1	2.0 ± 0.1	2.0 ± 0.1	2.0 ± 0.1	2.0 ± 0.1	2.0 ± 0.1
Number of ions/electrons generated ($\times 10^{17}$)	$^{\text{a}}8.99 \pm 0.45$	4.49 ± 0.96	4.49 ± 0.96	4.49 ± 0.96	$^{\text{a}}8.99 \pm 0.45$	4.49 ± 0.96	89.9 ± 4.5	44.9 ± 9.6
Initial energy of the ion/electrons (keV)	$^{\text{a}}2.50$	5.00	5.00	5.00	$^{\text{a}}2.50$	5.00	$^{\text{a}}2.50$	5.00
Average energy of the backscattered ions/electrons (keV)	1.5 ± 0.2	2.96 ± 0.07	2.96 ± 0.07	2.96 ± 0.07	1.5 ± 0.2	2.96 ± 0.07	1.5 ± 0.2	2.96 ± 0.07
Average transmitted energy of the ions/electrons (keV)	0.00 ± 0.00	0.00 ± 0.00	0.00 ± 0.00	0.00 ± 0.00	0.00 ± 0.00	0.00 ± 0.00	0.00 ± 0.00	0.00 ± 0.00
Fraction of backscattered ions/electrons (%)	6.9 ± 0.5	15.0 ± 1.1	15.0 ± 1.1	15.0 ± 1.1	6.9 ± 0.5	15.0 ± 1.1	6.9 ± 0.5	15.0 ± 1.1
Fraction of transmitted ions/electrons (%)	0.0 ± 0.0	0.0 ± 0.0	0.0 ± 0.0	0.00 ± 0.00	0.0 ± 0.0	0.00 ± 0.00	0.0 ± 0.0	0.00 ± 0.00
Simulated average penetration depth (nm)	53 ± 4	217 ± 11	217 ± 11	217 ± 11	53 ± 4	217 ± 11	53 ± 4	217 ± 11
Number of exposed molecules ($\times 10^{16}$)	2.67 ± 0.24	3.60 ± 0.39			$^{\text{b}}1.79 \pm 0.25$	$^{\text{c}}2.72 \pm 0.40$	$^{\text{b}}1.79 \pm 0.25$	$^{\text{c}}2.72 \pm 0.40$
					$^{\text{d}}(8.78 \pm 0.77) \times 10^{15}$	$^{\text{d}}(8.78 \pm 0.77) \times 10^{15}$		
Dose per molecule (keV)	80.6 ± 8.3	57.1 ± 6.9			$^{\text{b}}80.6 \pm 8.3$	$^{\text{c}}57.6 \pm 6.2$	$^{\text{b}}806 \pm 83$	$^{\text{c}}576 \pm 62$
					$^{\text{d}}158 \pm 28$		$^{\text{d}}1.58 \pm 0.28 \text{ MeV}$	

[†] This information is applicable to the 10 hour simultaneous irradiation experiment and sequential irradiation experiments listed in Table 3.1

^a This follows the assumption that D_2^+ ions fragment upon impact into a D^+ ion and a D atom [Sigmund et al. 1996]

^b Corresponding to $\text{Mg}(\text{ClO}_4)_2 \cdot 6\text{H}_2\text{O}$ molecules exposed only to D^+ ions

^c Corresponding to $\text{Mg}(\text{ClO}_4)_2 \cdot 6\text{H}_2\text{O}$ molecules exposed only to electrons

^d Corresponding to $\text{Mg}(\text{ClO}_4)_2 \cdot 6\text{H}_2\text{O}$ molecules exposed to both electrons and D^+ ions

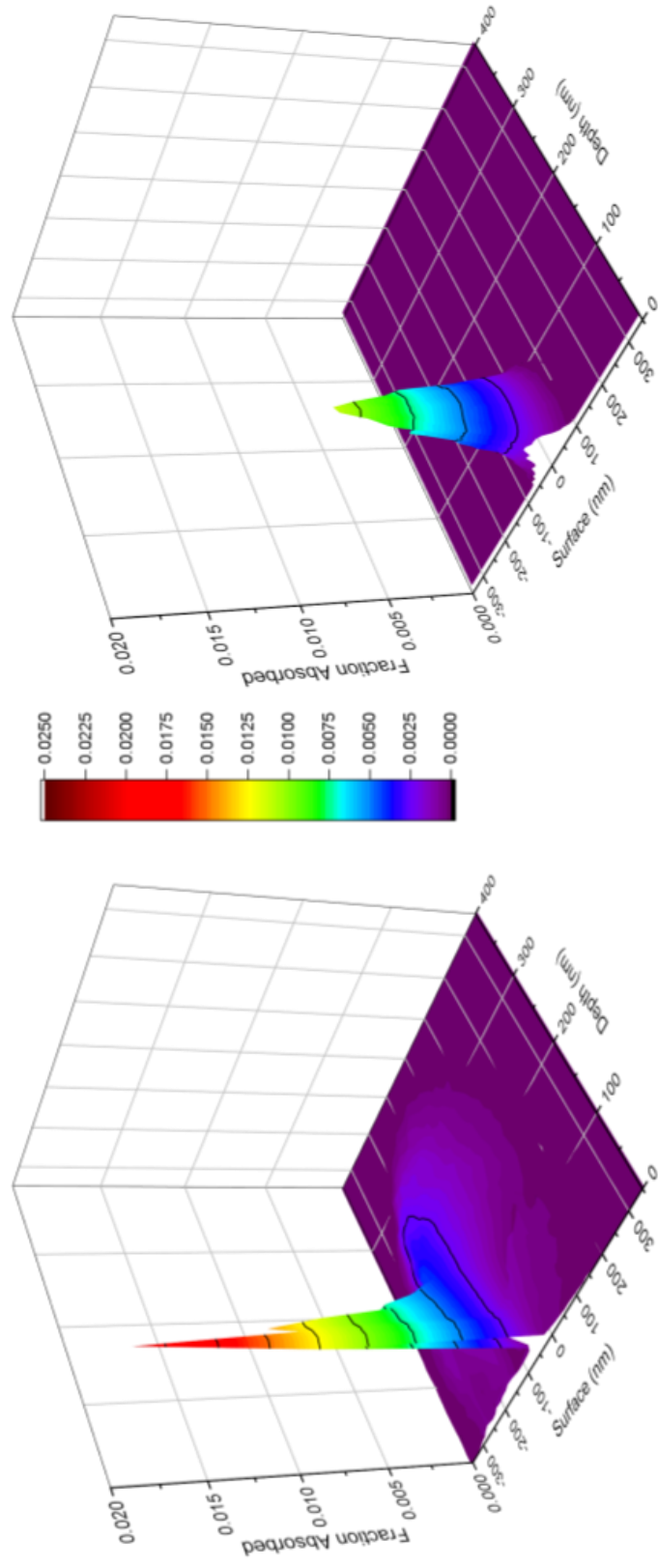


Figure 3.2 3D output of Monte Carlo simulations showing the penetration depth of energetic particles from a 5 keV electron beam at -30° using CASINO (left) and a 2.5 keV D^+ ion beam at 30° using SRIM (right). The Z-axis has been normalized.

To produce a consistent thickness, all samples were prepared by dissolving 0.250 ± 0.002 g $\text{Mg}(\text{ClO}_4)_2 \cdot 6\text{H}_2\text{O}$ in 15.00 ± 0.05 mL of distilled water and adding 0.700 ± 0.005 mL of the solution to the surface of the silver substrate by means of a syringe, after which the water (H_2O) solvent was evaporated by slowly heating up the silver substrate to 320 K on a hot plate and drying to constant mass. Care was taken to ensure that the solution completely covered the full area of the substrate before heating to obtain a sample with an even thickness. The average thickness was then calculated by using the weight difference of the silver wafer before and after the sample preparation, the area of the silver substrate (9.86 cm^2), and the density of the sample film ($1.98 \pm 0.03 \text{ g cm}^{-3}$) [Lewis and Hawley 2007] (Table 3.2).

Before any experiments were carried out, it was necessary to determine the average penetration depth of the ionizing radiation to be used to ensure that the perchlorate samples were prepared with sufficient thickness. This is done to prevent energetic ions and electrons from transmitting through the sample and interacting with the silver substrate. To model the secondary electrons produced in solid magnesium perchlorate crystals by GCRs with energies larger than 20 MeV, a Monte Carlo simulation using the CASINO software [Drouin et al. 2007] was used by considering 5 keV electrons irradiating a sample of pure magnesium perchlorate hexahydrate ($\text{Mg}(\text{ClO}_4)_2 \cdot 6\text{H}_2\text{O}$) at an incident angle of 30° to match the geometry of the experimental chamber (Figure 3.1). The simulation was run for 10^6 trajectories and concluded that the average penetration depth for the electrons is 217 ± 11 nm. Ion trajectories were modeled using the Stopping and Range of Ions in Matter (SRIM) Monte Carlo program [Ziegler, Ziegler, and Biersack 2010]. These calculations showed a mean stopping range of 53 ± 4 nm for deuterium ions (D^+ , 2.000 g mol^{-1}) with an energy of 2.5 keV at an incident angle of 30° . The program input parameters are outlined in Table 3.3 and the three-dimensional output from these simulations indicating the penetration

depth of each simulated particle is displayed in Figure 3.2. Since the samples are much thicker than the maximum penetration depths of the impinging ions (170 nm) and electrons (410 nm), we can safely conclude that there is no interaction with the substrate and that these particles deliver all their kinetic energy to the magnesium perchlorate hexahydrate ($\text{Mg}(\text{ClO}_4)_2 \cdot 6\text{H}_2\text{O}$) layer.

3.3 Results

During TPD, controlled heating of the sample induces the diffusion of reactive species (radicals, atoms) and molecular products formed within the perchlorate during irradiation. As these products sublime, they are ionized by the QMS and a mass-to-charge (m/z) signal is produced. The ion current for each signal can be correlated to the abundance of each species in the gas phase and is presented as a function of temperature in Figures 3.3a–f. It should first be noted that in all experiments besides the blank, a signal was detected at mass-to-charge ratios of $m/z = 16$ and $m/z = 32$ upon the onset of irradiation; the purpose of a blank experiment is to measure the residual gas in the chamber at base pressure and all signals in the succeeding experiments have taken the background into account. These signals are assigned to atomic (O) and molecular (O_2) oxygen respectively. The ratio of these signals matches the fragmentation pattern observed during the calibration of the QMS using pure O_2 gas, signifying that the signal for $m/z = 16$ is due to the dissociative ionization of molecular oxygen (O_2) caused by the impacting 100 eV electrons from the ionizer of the mass spectrometer [Linstrom and Mallard 2014]. Both signals rise sharply to their maximum value within the first few minutes of the experiment before decaying over the next 4–5 hours. No other species—particularly chlorine bearing molecules or known irradiation products of water (H_2O)—could be observed within the detection limits of our mass spectrometer. From here we will discuss the TPD results from each experiment separately.

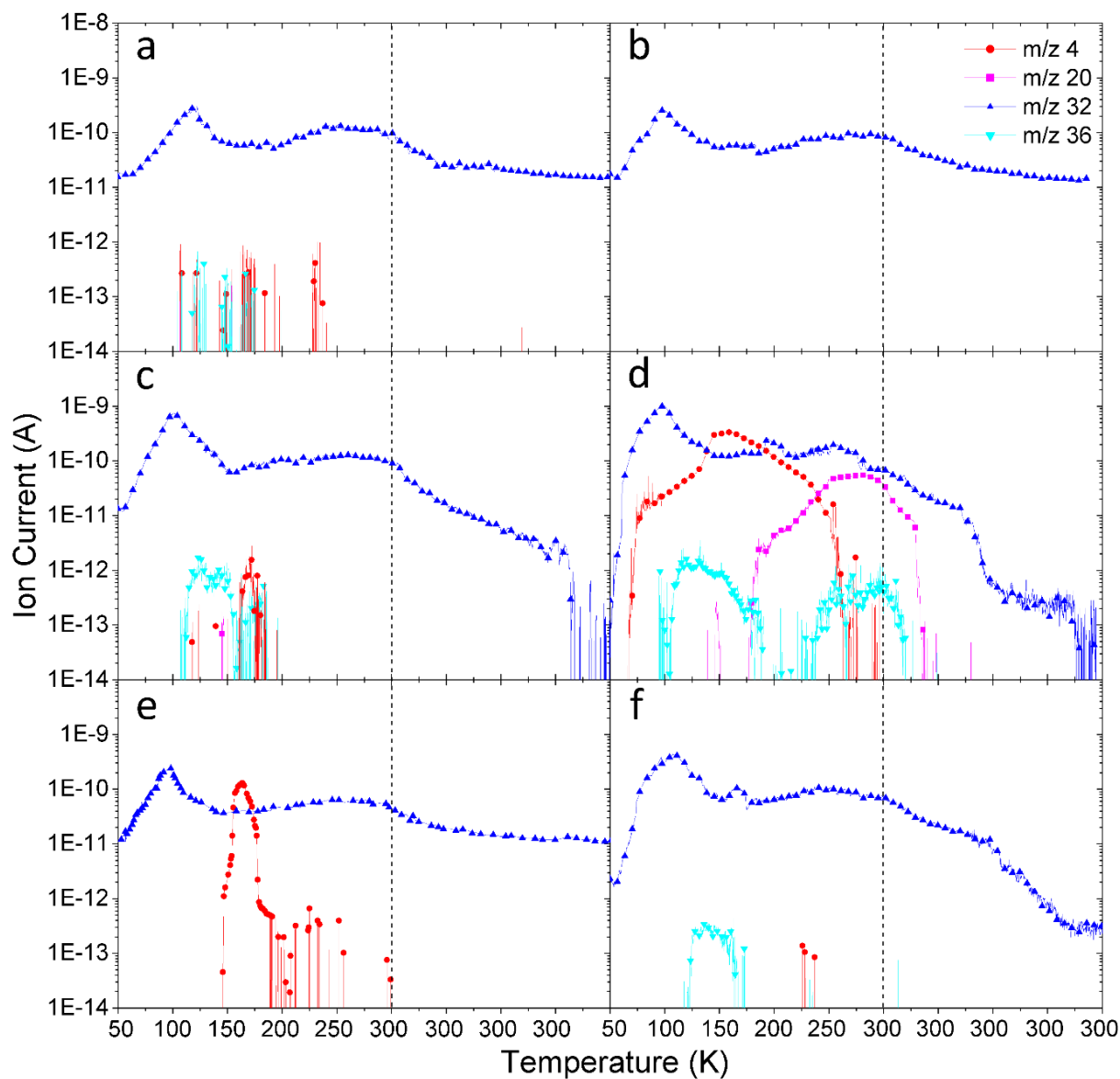


Figure 3.3 Ion currents of subliming species recorded by the EI-QMS during TPD for samples irradiated by: (a) 5 keV D_2^+ ions (10 hrs), (b) 5 keV electrons (10hrs), (c) simultaneous irradiation of 5 keV electrons and D_2^+ ions (10hrs), (d) simultaneous irradiation of 5 keV electrons and D_2^+ ions (100hrs), (e) 5 keV electrons (10 hrs) followed by 5 keV D_2^+ ions (10hrs) and (f) 5 keV D_2^+ ions (10 hrs) followed by 5 keV electrons (10 hrs).. The dotted vertical line indicates when the sample reached 300 K and was held isothermally.

3.3.1 5 keV D₂⁺ Irradiation

A sample was irradiated for 10 hours by a 5 keV D₂⁺ ion beam with a beam current of $2.0 \pm 0.1 \mu\text{A}$, resulting in a total fluence of $(6.6 \pm 1.0) \times 10^{17}$ D nuclei cm⁻². As the sample is heated after irradiation, the signal at $m/z = 32$ begins to rise again around 60 K to a peak ion current of 2.96×10^{-10} A at 118.4 ± 0.1 K as shown in Figure 3.3a. A second, much broader peak appears near 197 K and extends shortly beyond the point when the sample reached 300 K. Also observed were weak signals at $m/z = 4$ (from 104 to 239 K) and $m/z = 36$ (from 104–175 K), which are attributed to molecular deuterium (D₂) and D₂-hydrogen peroxide (D₂O₂) respectively. Hydrogen chloride (HCl) can be ruled out as contributing to the signal at $m/z = 36$ since one should expect to also see a weaker signal at $m/z = 38$, due to the high abundance of chlorine's second isotope (³⁷Cl). However, no such signal was observed. The detection of molecular deuterium (D₂) indicates that, as stated previously, the impinging molecular deuterium ions (D₂⁺) dissociate and neutralize upon impact with the solid surface and are implanted as two deuterium atoms. They may then recombine within the matrix after they have delivered all their kinetic energy to the surroundings.

3.3.2 5 keV Electron Irradiation

Magnesium perchlorate hexahydrate (Mg(ClO₄)₂·6H₂O) was also exposed to a 5 keV electron beam with a beam current of $2.0 \pm 0.2 \mu\text{A}$ for 10 hours. The spot size of the electron beam was approximately $0.46 \pm 0.1 \text{ cm}^2$, resulting in a fluence of $(9.8 \pm 1.0) \times 10^{17}$ electrons cm⁻². Similar to what was observed in the molecular deuterium ion (D₂⁺) irradiation experiment (Section 3.3.1), the signal at $m/z = 32$ begins to increase near 60 K and reaches a maximum value of 2.51×10^{-10} A at 95.7 ± 0.1 K (see Figure 3.3b). No signals were detected at $m/z = 4$, 20, and 36 giving

further evidence that our assignment of these signals to deuterium-containing products is reasonable.

3.3.3 Simultaneous Irradiation

Simultaneous irradiation using both 5 keV D_2^+ ions and electrons was performed in two separate experiments for 10 hours (Figure 3.3c) and 100 hours (Figure 3.3d) with the currents and beam properties kept identical to what was set for the sole source experiments previously described. After a 10 hour exposure, TPD shows the release of molecular oxygen (O_2) from the sample as $m/z = 32$ increases steadily to a maximum ion current of 7.02×10^{-10} A at 99.4 ± 0.1 K—more than twice as high as what was observed in either case when only ions or electrons were used (Section 3.3.1 and 3.3.2). The detection of d_2 -hydrogen peroxide and molecular deuterium is clear, with signals at $m/z = 36$ (D_2O_2) and $m/z = 4$ (D_2) ranging from 110 to 180 K and 160 to 180 K respectively. Lastly, we report the presence of heavy water (D_2O), represented by a small peak at $m/z = 20$, which sublimed from 146 to 148 K.

By increasing the exposure from 10 to 100 hours, the formation of D_2 , D_2O , and D_2O_2 was greatly enhanced. The release of D_2 ($m/z = 4$) was observed much earlier in the TPD than what was seen after a 10 hour exposure, beginning around 68 K and continuing until the sample reached 277 K. This signal peaked near 149 K with a maximum ion current of 3.23×10^{-10} A. Two sublimation events were observed for D_2O ($m/z = 20$); the first occurs near 148 K with a maximum current of 2.50×10^{-13} A and is likely the detection of a small amount of D_2O trapped near the surface of the sample that is forced out by gaseous D_2 being rapidly released from the sample. The second sublimation event begins at 177 K, reaches a maximum peak of 5.29×10^{-11} A around 284 K, and terminates 80 minutes after the sample has reached 300 K. D_2O_2 ($m/z = 36$) also sublimed

during two events that appear to coincide with the release of D₂ and D₂O: the first event ranges from 94 to 191 K with a maximum value of 3.33×10^{-12} A at 132 K and the second begins near 226 K and continues until 40 minutes after the sample reached 300 K. With large fluctuation in the ion current for this second peak, the temperature at which the maximum ion current was reached is ambiguous, but the shape of the peak closely follows that of the D₂O signal.

3.3.4 Sequential Irradiation

As a final set of experiments, pristine samples of magnesium perchlorate hexahydrate (Mg(ClO₄)₂·6H₂O) were again irradiated with both D₂⁺ ions and electrons, only this time the beams were used sequentially (Figures 3.3e and 3.3f). A sample was first irradiated by 5 keV electrons for 10 hours, and then held isothermally for 1 hour before being irradiated again by 5 keV D₂⁺ ions for an additional 10 hours (Figure 3.3e). A current of 2.0 ± 0.1 μA was used for both beams to apply effectively neutralizing charges. The process was repeated on a fresh sample with the order of the energetic particles reversed. These experiments yielded unique results and provide insight on the formation mechanisms of new products. When Mg(ClO₄)₂·6H₂O was irradiated with electrons prior to D₂⁺ ions, TPD shows an increase in $m/z = 32$ from 50 K to a maximum current of 2.46×10^{-10} A at 98.2 ± 0.1 K. As observed previously, a second, much broader peak at $m/z = 32$ appears between 200 and 300 K, though it is far less pronounced than similar peaks in the single source experiments. The only other product detected during TPD by the QMS was molecular deuterium (D₂, $m/z = 4$), appearing first at 146 K and reaching a peak current of 1.34×10^{-10} A at 164 K before trailing off around 200 K.

Reversing the order of irradiation resulted in the virtually complete disappearance of D₂ and the formation of D₂O₂ (Figure 3.3f). A signal with $m/z = 36$ appears in the temperature range

of 120–172 K, similar to what was seen during the simultaneous irradiation experiments only with less intensity by roughly an order of magnitude. Molecular oxygen (O_2), represented by the signal at $m/z = 32$, was also detected; the highest measured abundance in the gas phase was at 110 K with an ion current of 4.21×10^{-10} A.

3.4 Discussion

3.4.1 Production Yields

The release of molecular oxygen (O_2) is the sole common result across all experiments, although the intensity of the mass-to-charge ratio ($m/z = 32$) varies based on the experimental conditions. The sublimation of O_2 between 60 to 100 K is a particularly notable result as these experiments were conducted at a temperature above the sublimation point of O_2 under vacuum (about 30 K) [Bennett et al. 2011; Ennis and Kaiser 2012] and indicates that O_2 is initially trapped inside the solid sample. Accordingly, a higher temperature is required to overcome the barrier to diffusion to be eventually released into the gas phase. The second, broad peak appearing near 200 K has previously been attributed to molecular oxygen forming in situ during TPD from thermal decomposition of chlorine oxides as various chlorine oxides (Cl_xO_y , $x = 1-2$, $y = 1-7$) synthesized during the irradiation become thermally unstable at higher temperatures and decay into chlorine oxides via oxygen loss [Góbi et al. 2016b; Góbi et al. 2017b].

Table 3.4 Total molecules produced via radiolysis of magnesium perchlorate hexahydrate

	D_2^+	e^-	$D_2^+ + e^-$ (10 hr)	$D_2^+ + e^-$ (100 hr)	$e^- \rightarrow D_2^+$	$D_2^+ \rightarrow e^-$
D_2 ($m/z = 4$)	$(1.2 \pm 0.3) \times 10^{13}$	---	$(2.8 \pm 0.6) \times 10^{13}$	$(4.5 \pm 0.9) \times 10^{16}$	$(4.0 \pm 0.8) \times 10^{15}$	---
D_2O ($m/z = 20$)	---	---	---	$(3.5 \pm 0.7) \times 10^{15}$	---	---
O_2 ($m/z = 32$)	$(4.3 \pm 0.9) \times 10^{16}$	$(4.3 \pm 0.9) \times 10^{16}$	$(8.9 \pm 1.4) \times 10^{16}$	$(1.3 \pm 0.3) \times 10^{17}$	$(5.6 \pm 1.1) \times 10^{16}$	$(5.5 \pm 1.1) \times 10^{16}$
D_2O_2 ($m/z = 36$)	$(2.6 \pm 0.5) \times 10^{12}$	---	$(3.0 \pm 0.6) \times 10^{13}$	$(7.6 \pm 1.6) \times 10^{13}$	---	$(7.8 \pm 1.6) \times 10^{12}$

By integrating the ion current for these signals, we extract quantitative information. Considering that Figure 3.3 displays the ion current as a function of temperature and recalling that a change of 1 K during TPD is equivalent to a time of 120 s, the integrated signal can be displayed with units of Ampere seconds which is equal to 1 Coulomb (C). For the D_2^+ irradiation experiment, the total integrated signal at $m/z = 32$ is $(6.0 \pm 0.5) \times 10^{-6}$ C, which includes the abundance of gaseous molecular oxygen (O_2) detected during the irradiation phase. The other two detected signals integrate to $(6.7 \pm 0.7) \times 10^{-10}$ C (D_2 , $m/z = 4$) and $(3.7 \pm 0.4) \times 10^{-10}$ C (D_2O_2 , $m/z = 36$). Since our mass spectrometer has been calibrated for O_2 using the same settings for electron energy, emission current, and secondary electron multiplier voltage, we can use this calibration study to compute the total number of molecular oxygen (O_2) molecules formed in the experiment to be $(4.3 \pm 0.9) \times 10^{16}$ molecules. The total number of molecular deuterium (D_2) and deuterium peroxide (D_2O_2) molecules was also calculated to be $(1.2 \pm 0.3) \times 10^{13}$ and $(2.6 \pm 0.5) \times 10^{12}$ molecules respectively, by taking into account the electron impact ionization cross section for each

molecule at 100 eV and comparing their integrated signals to that of O₂ (refer to Table 3.4) [Y. K. Kim and Rudd 1994, Zheng et. al 2006].

The same treatment was given to data collected during TPD after electron bombardment. Integrating the ion current for $m/z = 32$ over the irradiation phase and TPD gives a value of $(5.9 \pm 0.5) \times 10^{-6}$ C and corresponds to $(4.3 \pm 0.9) \times 10^{16}$ total molecules of molecular oxygen (O₂) produced. The reader should recognize it is by coincidence that this is the same reported value for the production of O₂ under ion irradiation. This result was not expected as the number of magnesium perchlorate hexahydrate (Mg(ClO₄)₂·6H₂O) molecules processed during irradiation is different between the two experiments because the spot sizes and penetration depths of the beams are not equivalent.

After samples were irradiated simultaneously by both radiation sources for 10 hours, four m/z signals appeared during TPD that are assigned to new products, namely, D₂, D₂O, O₂, and D₂O₂. In this case, the signal corresponding to D₂O only barely reaches above the lowest detectable limit of the QMS (about 10^{-14} C) and could not be quantified within the error limits. Integrating the signals for D₂, D₂O₂, and O₂, however, gives $(1.5 \pm 0.2) \times 10^{-9}$ C (D₂), $(4.4 \pm 0.4) \times 10^{-9}$ C (D₂O₂) and $(1.3 \pm 0.1) \times 10^{-5}$ C (O₂); from these values we have determined the absolute number of molecules produced to be $(2.8 \pm 0.6) \times 10^{13}$, $(3.1 \pm 0.6) \times 10^{13}$, and $(8.9 \pm 1.4) \times 10^{16}$, respectively. The abundance of these products changes when the exposure time is extended to 100 hours, thereby increasing the dose by an order of magnitude. The integrated ion current for O₂ in this case was $(1.8 \pm 0.2) \times 10^{-5}$ C, which is equivalent to $(1.3 \pm 0.3) \times 10^{17}$ molecules—an increase by a factor of about 1.5. Thus, we see that at high doses the production of O₂ does not increase linearly with exposure. The same is true for the formation of D₂, D₂O, and D₂O₂. The total integrated ion currents for signals at $m/z = 4$, 20, and 32 after 100 hours of irradiation were $(2.4 \pm 0.2) \times 10^{-5}$ C,

$(4.5 \pm 0.5) \times 10^{-7}$ C, and $(1.1 \pm 0.1) \times 10^{-8}$ C, respectively. This translates to $(4.5 \pm 0.9) \times 10^{16}$ molecules for D_2 , $(3.5 \pm 0.7) \times 10^{15}$ molecules for D_2O , and $(7.6 \pm 1.6) \times 10^{13}$ molecules for D_2O_2 (Table 3.4).

3.4.2 O₂ Mass Balance

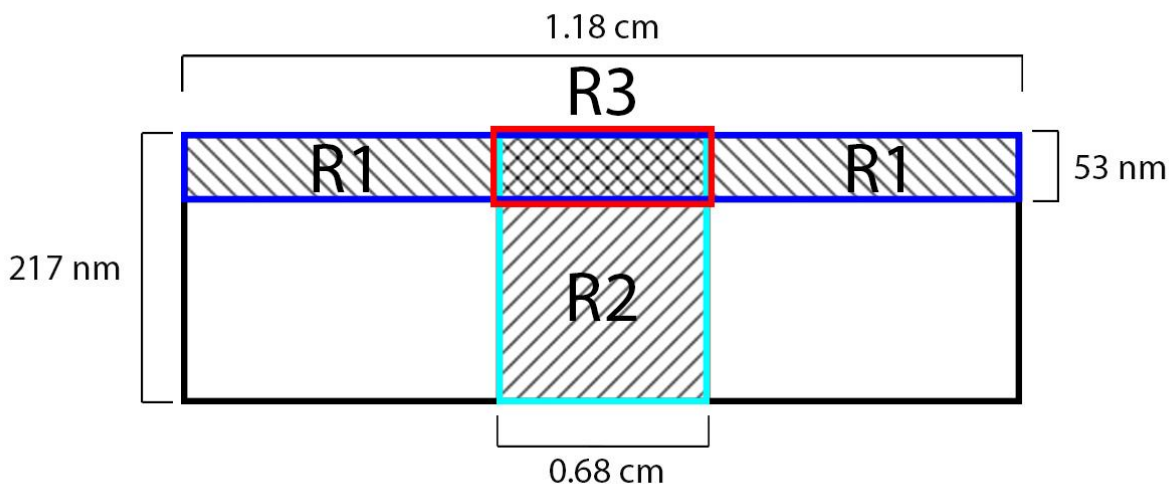
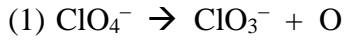


Figure 3.4 Simplified model depicting the depth profile of a sample exposed to both D^+ ions and electrons based on TRIM and CASINO calculations. R1 represents the volume exposed to D^+ ions, whereas R2 is the volume of the samples irradiated by electrons. The region in the sample where these particles overlap is indicated by R3.

Under each experimental condition, the energetic processing of magnesium perchlorates results in the formation of molecular oxygen (O_2) as the major product by decomposition of the perchlorate anion (ClO_4^-). Here we make a comparison between the destruction of ClO_4^- and the formation of O_2 for each experiment. For the purpose of discussion, it is useful to visualize the irradiated volume defined by the boundaries of the spot size of the beam and the average penetration depth of the energetic particles calculated from the Monte Carlo simulations (Figure 3.4). Knowing this volume and the density of the sample, we can then compute the number of molecules processed during the experiment. When magnesium perchlorate hexahydrate

(Mg(ClO₄)₂·6H₂O) was irradiated with molecular deuterium ions (D₂⁺), $(2.7 \pm 0.2) \times 10^{16}$ molecules were exposed and resulted in the formation of $(4.3 \pm 0.9) \times 10^{16}$ oxygen molecules (O₂)—a ratio of 1.6 ± 0.4 O atoms produced per perchlorate unit (ClO₄[−]) destroyed. It is likely that with a ratio higher than one oxygen atom per destroyed perchlorate anion, a portion of the exposed parent molecules decomposed to form other chlorine oxide species, such as chlorine dioxide (ClO₂) [Góbi et al. 2016b], though no such products were detected by the QMS due to lack of sensitivity. Irradiation of the sample by 5 keV electrons resulted in the destruction of $(3.6 \pm 0.4) \times 10^{16}$ magnesium perchlorate hexahydrate molecules and the formation of $(4.3 \pm 0.9) \times 10^{16}$ O₂ molecules. A ratio of 1.2 ± 0.2 O atoms per destroyed perchlorate unit was determined from these values. From these two experiments, we conclude that the primary process in the radiolysis of perchlorates by GCRs is the formation of free atomic oxygen. Oxygen atoms can then combine to produce molecular oxygen (O₂) [A.M. Turner, Abplanalp, and Kaiser 2016].



The boundary for the region where ions and electrons overlapped in the sample during the simultaneous and sequential irradiation experiments (R3 in Figure 3.4) is determined by the spot size of the electron beam and the average penetration depth of the ions. Using these values, the number of magnesium perchlorate hexahydrate (Mg(ClO₄)₂·6H₂O) molecules exposed to both radiation sources was $(8.8 \pm 0.8) \times 10^{15}$. An additional $(1.8 \pm 0.3) \times 10^{16}$ molecules were irradiated by molecular deuterium ions (D₂⁺) alone (R1 in Figure 3.4) while another $(2.7 \pm 0.4) \times 10^{16}$ molecules were below the penetration depth of the ions and thus only processed by the electrons (R2 in Figure 3.4). As reported earlier, $(8.9 \pm 1.4) \times 10^{16}$ oxygen molecules (O₂) were produced during the 10 hour simultaneous irradiation experiment, resulting in an average ratio of 1.7 ± 0.3 O atoms per perchlorate unit destroyed. Upon first glance, this result would seem to imply that

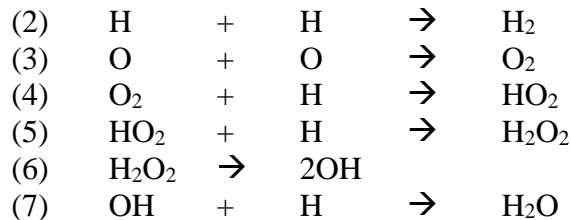
simultaneous irradiation of ions and electrons does not greatly increase the production of oxygen molecules (O_2) when compared to the single source experiments. However, we can go one step further to determine the contribution of O_2 produced within the overlap region and compare it to the total yield. By subtracting the volume of the overlap region (R3) from the volume subject to ion exposure, we determine the volume and number of magnesium perchlorate hexahydrate ($\text{Mg}(\text{ClO}_4)_2 \cdot 6\text{H}_2\text{O}$) molecules that were only exposed to deuterium ions (D^+) during the simultaneous irradiation experiment (R1). Since the beam conditions and the duration of exposure were identical to the set parameters of the single source experiments, we argue that the molecules in this region received the same dose of energy that was calculated for the D_2^+ experiment ($80.6 \pm 8.3 \text{ keV molecule}^{-1}$) and would still produce an average of 1.6 ± 0.4 O atoms per perchlorate unit (ClO_4^-) destroyed, corresponding to $(2.9 \pm 0.8) \times 10^{16}$ oxygen molecules (O_2). The volume of the sample only exposed to electrons is found in the same manner (R2), however, since the electrons will give up a portion of their initial energy while traveling through the first 53 nm of the sample, we cannot assume that the average dose for this region is equivalent to the $57.1 \pm 6.9 \text{ keV molecule}^{-1}$ we reported previously. CASINO calculations reveal that 99.8% of all electrons which are not backscattered will transmit beyond 53 nm and still retain on average 69.8% of their initial energy. From this information we determined that the dose received by molecules in the range from 53 to 217 nm is $57.6 \pm 6.2 \text{ keV molecule}^{-1}$ —an increase of less than 1% of the dose delivered in the electron irradiation experiment. Thus, we rationalize that there is essentially no change in the production ratio of 1.2 ± 0.2 O atoms per perchlorate unit destroyed and attribute $(3.2 \pm 0.8) \times 10^{16}$ oxygen molecules (O_2) from sole exposure to electrons. The remaining $(2.9 \pm 1.5) \times 10^{16} \text{ O}_2$ must come from the overlapping region, which translates to a ratio of 3.3 ± 1.8 O atoms per perchlorate unit (ClO_4^-) destroyed.

3.4.3 H₂O₂ on Mars

Turner et al. [2016] describes how the radiolytic decomposition of perchlorates (ClO₄⁻) by energetic electrons results in a chlorine–oxygen bond rupture to yield chlorate (ClO₃⁻) plus atomic oxygen (O) as shown in equation (1). Additionally, [Góbi et al. 2016b] reported the first in situ detection of chlorine dioxide (ClO₂) via photoionization reflectron time-of-flight mass spectrometry. Chlorine dioxide was also found to form as a result of gamma ray exposure to calcium perchlorates in a CO₂ atmosphere, in addition to molecular oxygen (O₂) and hypochlorite (ClO⁻) [Quinn et al. 2013]. While the source of ionizing radiation to simulate GCRs varies amongst previous studies, it can be shown that the resulting products and their abundances are commensurate when comparing similar energy doses. Our experiments presented here show the production of O₂ in concentrations similar to previous studies, but also serve as the first experimental study to identify the possible formation of hydrogen peroxide (H₂O₂) in the Martian regolith as a degradation product of perchlorates by GCRs. H₂O₂ has long been considered to serve an important role as an oxidant in the Martian subsurface ever since the Viking landers failed to detect any organic molecules above a 1ppb detection limit [Biemann et al. 1977]. Even prior to its first confirmed detection by ground-based telescopes in 2003 at a mixing ratio between 20 to 40 ppb [Clancy et al. 2004; Encrenaz et al. 2004], the formation of H₂O₂ has been predicted by several photochemical models [Parkinson and Hunten 1972; Krasnopolsky 1993; McElroy, Kong, and Yung 1977] and has more recently been proposed to also form by the dissociation of atmospheric CO₂ and H₂O in electrostatic fields generated by dust storms [Atreya et al. 2006; T. Encrenaz et al. 2012]. Our experiments suggest that the formation of hydrogen peroxide via degradation of perchlorates might represent a significant contribution to the global yield – even generated below the surface. As it may diffuse through the regolith towards the surface, H₂O₂ along with O₂ create

a highly oxidative environment that would accelerate the degradation of organic material. This would help to explain why exogenous organic material has not been found to accumulate to levels above 1 ppb in the Martian subsurface despite being shielded from UV light and atmospheric oxidants.

Having established the identity of the reaction products and their dependence on the dose, we are now proposing realistic formation routes based on previous laboratory experiments in our group accounting for the current experimental findings. First, previous studies exposed that atomic hydrogen can recombine to molecular hydrogen (H_2) releasing the 4.5 eV binding energy to the matrix [Kaiser et al. 1997; He et al. 2010]. Similarly, atomic oxygen – once released from the perchlorate ion – recombined to molecular oxygen (O_2). Considering that low radiation doses lead to hydrogen peroxide (H_2O_2), but not to water (H_2O), which requires enhanced radiation exposure, hydrogen peroxide is likely formed via successive reduction (hydrogenation) of molecular oxygen via the hydroperoxy radical (HO_2) [Kaiser et al. 1995], which then recombined barrierlessly with a second hydrogen atom to hydrogen peroxide (H_2O_2). Enhanced radiation exposure can lead to a homolytic bond rupture in hydrogen peroxide forming two hydroxy radicals (OH) [Kaiser et al. 1995]. Here, hydroxyl radicals can easily react with atomic hydrogen to form water (H_2O). Although alternative formation routes to water and hydrogen peroxide have been proposed such as the reaction of atomic oxygen with hydrogen and oxygen insertion into the H-O bond of water forming hydrogen peroxide [Bennett et al. 2014], these suggested pathways are not in accord with our experimental findings of a delayed production of water compared to hydrogen peroxide.



We reiterate that these experiments have been carried out under ultra-high vacuum conditions (10^{-10} torr) at 50 K for the purpose of investigating whether impinging ions can participate directly in the formation of new products. While these conditions do not closely replicate the ambient Martian environment at or below the surface, such conditions were favorable to minimize the possibility of contamination of the samples from residual gases, particularly molecular oxygen (O₂) and water (H₂O). The low temperature also serves to limit the thermal diffusion of products in the sample before TPD to differentiate between newly formed species and sputtered material. Additional experiments with conditions more representative of the Martian environment would prove useful to the planetary science community. Specifically, the work by Turner et al. [2016] revealed that O₂ production by radiolytic processing was temperature dependent; follow-up studies to determine the temperature dependency of H₂O₂ formation would provide actual rate constants to be incorporated into models. Furthermore, experiments conducted under a simulated carbon dioxide (CO₂) atmosphere could result in an increase in the production of H₂O₂ since molecular oxygen (O₂) levels would rise from the decomposition of CO₂ by proton irradiation [Anderson and Best 1966].

3.5 Conclusion

The objective of this work was to investigate the degradation of perchlorates within the terminal track of galactic and solar cosmic rays in the Martian regolith to more fully understand the role these oxidizing agents play in the destruction of organic molecules. The experiments we conducted show that not only is molecular oxygen (O_2) produced by the radiolysis of perchlorates, but also provide proof-of-concept that GCRs, which are mostly made up of protons, can take part in the formation of new products after they have been supplanted in the soil. Using electron impact quadrupole mass spectrometry, we have detected for the first time the formation of hydrogen peroxide, another known strong oxidizer, in addition to molecular oxygen (O_2) and molecular deuterium (D_2). At higher doses, heavy water (D_2O) was also detected. Kinetic studies for destruction and formation rates of products was beyond the scope of this work, but future experiments investigating these rates would reveal the mechanistic pathways towards the production of hydrogen peroxide. With application to Mars chemistry, this study contributes to the statements made by Turner et al. [2016] and Góbi et al. [2016b] that not only can GCRs destroy organic molecules up to 2 m below the surface [Pavlov et al. 2012], but they also generate the destruction of perchlorates into volatile compounds with greater oxidizing power than perchlorates themselves.

3.6 References

- Anderson, A. R., & Best, J. V. F. (1966). Proton Radiolysis of Carbon Dioxide. *Transactions of the Faraday Society*, 62, 610–618. <https://doi.org/10.1039/TF9666200610>
- Archer, P. D., & Franz, H. B. (2013). Abundances and implications of volatile-bearing species from evolved gas analysis of the Rocknest aeolian deposit, Gale Crater, Mars. *Journal of Geophysical Research: Planets*, 237–254. <https://doi.org/10.1002/2013JE004493>. Received
- Arista, N. R. (2000). Stopping of molecules and clusters. *Nuclear Instruments and Methods in Physics Research, Section B: Beam Interactions with Materials and Atoms*, 164, 108–138. [https://doi.org/10.1016/S0168-583X\(99\)01069-1](https://doi.org/10.1016/S0168-583X(99)01069-1)
- Atreya, S. K., Wong, A.-S., Renno, N. O., Farrell, W. M., Delory, G. T., Sentman, D. D., Catling, D. C. (2006). Oxidant enhancement in Martian dust devils and storms: Implications for life and habitability. *Astrobiology*, 6(3), 439–450. <https://doi.org/10.1089/ast.2006.6.439>
- Bennett, C. J., Ennis, C. P., & Kaiser, R. I. (2014). Experimental Studies on the Formation of D₂O and D₂O₂ By Implantation of Energetic D⁺ Ions Into Oxygen Ices. *The Astrophysical Journal*, 782(2), 63. <https://doi.org/10.1088/0004-637X/782/2/63>
- Bennett, C. J., Hama, T., Kim, Y. S., Kawasaki, M., & Kaiser, R. I. (2011). Laboratory Studies on the Formation of Formic Acid (Hcooh) in Interstellar and Cometary Ices. *The Astrophysical Journal*, 727(1), 27. <https://doi.org/10.1088/0004-637X/727/1/27>
- Bennett, C. J., Jamieson, C., Mebel, A. M., Kaiser, R. I., & Keynes, M. (2004). Untangling the formation of the cyclic carbon trioxide isomer in low temperature carbon dioxide ices. *Physical Chemistry Chemical Physics*, 6(4), 735. <https://doi.org/10.1039/b315626p>

- Bennett, C., Jamieson, C., Osamura, Y., & Kaiser, R. (2005). A combined experimental and computational investigation on the synthesis of acetaldehyde in interstellar ices. *The Astrophysical Journal*, 624, 1097–1115. <https://doi.org/10.1086/429119>
- Biemann, K., Oro, J., Toulmin III, P., Orgel, L. E., Nier, A. O., Anderson, D. M., ... Simmonds, P. G. (1977). The search for organic substances and inorganic volatile compounds in the surface of Mars. *Journal of Geophysical Research*, 82(28), 4641–4658. <https://doi.org/10.1029/JS082i028p04641>.
- Carrier, B. L., & Kounaves, S. P. (2015). The origins of perchlorate in the Martian soil. *Geophysical Research Letters*, 42, 3739–3745. <https://doi.org/10.1002/2013GL058489>.
- Catling, D. C., Claire, M. W., Zahnle, K. J., Quinn, R. C., Clark, B. C., Hecht, M. H., & Kounaves, S. (2010). Atmospheric origins of perchlorate on mars and in the Atacama. *Journal of Geophysical Research E: Planets*, 115(1). <https://doi.org/10.1029/2009JE003425>
- Clancy, R. T., Sandor, B. J., & Moriarty-Schieven, G. H. (2004). A measurement of the 362 GHz absorption line of Mars atmospheric H₂O₂. *Icarus*, 168 (1), 116–121. <https://doi.org/10.1016/j.icarus.2003.12.003>
- Drouin, D., Couture, A. R., Joly, D., Tastet, X., Aimez, V., & Gauvin, R. (2007). CASINO V2.42 - A fast and easy-to-use modeling tool for scanning electron microscopy and microanalysis users. *Scanning*, 29(3), 92–101. <https://doi.org/10.1002/sca.20000>
- Encrenaz, T., Bézard, B., Greathouse, T. . K., Richter, M. . J., Lacy, J. . H., Atreya, S. . K., ... Forget, F. (2004). Hydrogen peroxide on Mars: evidence for spatial and seasonal variations. *Icarus*, 170(2), 424–429. <https://doi.org/10.1016/j.icarus.2004.05.008>
- Encrenaz, T., Greathouse, T. K., Lefèvre, F., & Atreya, S. K. (2012). Hydrogen peroxide on Mars:

- Observations, interpretation and future plans. In *Planetary and Space Science* (Vol. 68, pp. 3–17). <https://doi.org/10.1016/j.pss.2011.03.019>
- Ennis, C., Bennett, C. J., Jones, B. M., & Kaiser, R. I. (2011). Formation of D₂-Water and D₂-Carbonic Acid in Oxygen-Rich Solar System Ices Via D₂⁺ Irradiation. *Astrophysical Journal*, 733(2). <https://doi.org/10.1088/0004-637x/733/2/79>
- Ennis, C., & Kaiser, R. I. (2012). On the Formation of Ozone in Solar System Oxygen Ices Exposed To Heavy Ions. *The Astrophysical Journal*, 745(2), 103. <https://doi.org/10.1088/0004-637X/745/2/103>
- Flynn, G. J., & McKay, D. S. (1990). An Assessment of the Meteoritic Contribution to the Martian Soil. *Journal of Geophysical Research*, 95, 14497–14509.
- Freissinet, C., Glavin, D. P., Mahaffy, P. R., Miller, K. E., Eigenbrode, J. L., Summons, R. E., ... Zorzano, M. P. (2015). Organic molecules in the Sheepbed Mudstone, Gale Crater, Mars. *Journal of Geophysical Research E: Planets*, 120(3), 495–514. <https://doi.org/10.1002/2014JE004737>
- Glavin, D. P., Freissinet, C., Miller, K. E., Eigenbrode, J. L., Brunner, A. E., Buch, A., ... Mahaffy, P. R. (2013). Evidence for perchlorates and the origin of chlorinated hydrocarbons detected by SAM at the Rocknest aeolian deposit in Gale Crater. *Journal of Geophysical Research E: Planets*, 118(10), 1955–1973. <https://doi.org/10.1002/jgre.20144>
- Góbi, S., Abplanalp, M. J., & Kaiser, R. I. (2016). Effect of Perchlorates on Electron Radiolysis of Glycine With Application To Mars. *The Astrophysical Journal*, 822(1), 8. <https://doi.org/10.3847/0004-637X/822/1/8>
- Góbi, S., Bergantini, A., & Kaiser, R. I. (2016). In situ detection of chlorine dioxide (ClO₂) in the

- radiolysis of perchlorates and implications for the stability of organics on mars. *The Astrophysical Journal*, 832(2), 2–7.
- Góbi, S., Bergantini, A., & Kaiser, R. I. (2017). Degradation of Adenine on the Martian Surface in the Presence of Perchlorates and Ionizing Radiation: A Reflectron Time-of-flight Mass Spectrometric Study. *The Astrophysical Journal*, 838(2), 84–105. Retrieved from <https://doi.org/10.3847/1538-4357/aa653f>
- Góbi, S., Förstel, M., Maksyutenko, P., & Kaiser, R. I. (2017). A Reflectron Time-of-Flight Mass Spectrometric Study on the Degradation Pathways of Glycine on Mars in the Presence of Perchlorates and Ionizing Radiation. *The Astrophysical Journal*, 835(2), 241. <https://doi.org/10.3847/1538-4357/835/2/241>
- Hassler, D. M., Zeitlin, C., Wimmer-schweingruber, R. F., Ehresmann, B., Rafkin, S., Eigenbrode, J. L., Team, M. S. L. S. (2014). Mars' Surface Radiation Environment, 343 (January), 1–7.
- He, J., Gao, K., Vidali, G., Bennett, C. J., & Kaiser, R. I. (2010). Formation of Molecular Hydrogen From Methane Ice. *The Astrophysical Journal*, 721(2), 1656–1662. <https://doi.org/10.1088/0004-637X/721/2/1656>
- Hecht, M. H., Kounaves, S. P., Quinn, R. C., West, S. J., Young, S. M. M., Ming, D. W., ... Smith, P. H. (2009). Detection of Perchlorate and the Soluble Chemistry of Martian Soil at the Phoenix Lander Site. *Science*, 325(July), 64–67. <https://doi.org/10.1126/science.1172466>
- Jones, B. M., Bennett, C. J., & Kaiser, R. I. (2011). Mechanistical Studies on the Production of Formamide (H₂NCHO) Within Interstellar Ice Analogs. *The Astrophysical Journal*, 734(2), 78. <https://doi.org/10.1088/0004-637X/734/2/78>
- Kaiser, R. I., Eich, G., Gabrysch, a., & Roessler, K. (1997). Theoretical and Laboratory Studies

- on the Interaction of Cosmic-Ray Particles with Interstellar Ices. II. Formation of Atomic and Molecular Hydrogen in Frozen Organic Molecules. *The Astrophysical Journal*, 484(1), 487–498. <https://doi.org/10.1086/304316>
- Kaiser, R. I., Gabtysch, A., & Roessler, K. (1995). Cosmic ray simulator : A versatile apparatus for quantitative studies on the interaction of cosmic rays with frozen solids by on line and in sift quadrupole mass spectrometry and Fourier transform infrared spectroscopy, 66(4).
- Kaiser, R. I., & Roessler, K. (1997). Theoretical and laboratory studies on the interaction of cosmic-ray particles with interstellar ices. I. Synthesis of polycyclic aromatic hydrocarbons by a cosmic-ray induced multicenter mechanism. *The Astrophysical Journal*, 475, 144–154.
- Kim, Y. K., & Rudd, M. E. (1994). Binary-encounter-dipole model for electron-impact ionization. *Physical Review A*, 50(5), 3954–3967. <https://doi.org/10.1103/PhysRevA.50.3954>
- Kim, Y. S., Wo, K. P., Maity, S., Atreya, S. K., & Kaiser, R. I. (2013). Radiation-induced formation of chlorine oxides and their potential role in the origin of martian perchlorates. *Journal of the American Chemical Society*, 135(13), 4910–4913. <https://doi.org/10.1021/ja3122922>
- Köhler, J., Wimmer-Schweingruber, R. F., Appel, J., Ehresmann, B., Zeitlin, C., Hassler, D. M., ... Rafkin, S. (2016). Electron/positron measurements obtained with the mars science laboratory radiation assessment detector on the surface of mars. *Annales Geophysicae*, 34(1), 133–141. <https://doi.org/10.5194/angeo-34-133-2016>
- Krasnopolsky, V. (1993). Photochemistry of the Martian Atmosphere (Mean Conditions). *Icarus*, 101(2), 313–332. <https://doi.org/10.1006/icar.1993.1027>
- Lewis, R. J., & Hawley, G. G. (2007). *Hawley's Condensed Chemical Dictionary* (15th ed.).

Chichester : Wiley.

Linstrom, P. J., & Mallard, W. G. (2014). *NIST Chemistry webBook, NIST Standard Reference Database Number 69. National Institute of Standards and Technology.*

<https://doi.org/citeulike-article-id:3211271>

McElroy, M. B., Kong, T. Y., & Yung, Y. L. (1977). Photochemistry and Evolution of Mars' Atmosphere: A Viking Perspective. *Journal of Geophysical Research*, 82(28), 4379–4388.

<https://doi.org/10.1029/JS082i028p04379>

Ming, D. W., Lauer, H. V, Archer, P. D., Sutter, B., Golden, D. C., Morris, R. V, ... Boynton, W. V. (2009). Combustion of Organic Molecules by the Thermal Decomposition of Perchlorate Salts: Implications for Organics at the Mars Phoenix Scout Landing Site. *40th Lunar and Planetary Science Conference, (Lunar and Planetary Science XL), 40, 2241.*

<https://doi.org/10.1029/2008JE003083>.

Molina-Cuberos, G. (2001). Cosmic Ray and UV Radiation Models on the Ancient Martian Surface. *Icarus*, 154(1), 216–222. <https://doi.org/10.1006/icar.2001.6658>

Muñoz-Caro, G. M., Mateo-Martí, E., & Martínez-Frías, J. (2006). Near-UV Transmittance of Basalt Dust as an Analog of the Martian Regolith: Implications for Sensor Calibration and Astrobiology. *Sensors*, 6(6), 688–696. <https://doi.org/10.3390/s6060688>

Navarro-González, R., Vargas, E., De La Rosa, J., Raga, A. C., & McKay, C. P. (2010). Reanalysis of the Viking results suggests perchlorate and organics at midlatitudes on Mars. *Journal of Geophysical Research E: Planets*, 115(12), 1–11. <https://doi.org/10.1029/2010JE003599>

Oro, J., & Holzer, G. (1980). The Photolytic Degradation and Oxidation of Organic Compounds Under Simulated Martian Conditions. *Journal of Molecular Evolution*, 16, 69–72.

- Parkinson, T. D., & Hunten, D. M. (1972). Spectroscopy and Aeronomy of O₂ on Mars. *Journal of the Atmospheric Sciences*, 29(7), 1380–1390. [https://doi.org/10.1175/1520-0469\(1972\)029<1380:SAAOOO>2.0.CO;2](https://doi.org/10.1175/1520-0469(1972)029<1380:SAAOOO>2.0.CO;2)
- Pavlov, A. A., Vasilyev, G., Ostryakov, V. M., Pavlov, A. K., & Mahaffy, P. (2012). Degradation of the organic molecules in the shallow subsurface of Mars due to irradiation by cosmic rays. *Geophysical Research Letters*, 39(13), 5–9. <https://doi.org/10.1029/2012GL052166>
- Poch, O., Jaber, M., Stalport, F., Nowak, S., Georgelin, T., Lambert, J.-F., ... Coll, P. (2015). Effect of nontronite smectite clay on the chemical evolution of several organic molecules under simulated Martian surface ultraviolet radiation conditions. *Astrobiology*, 15(3), 221–237. <https://doi.org/10.1089/ast.2014.1230>
- Quinn, R. C., Martucci, H. F. H., Miller, S. R., Bryson, C. E., Grunthaner, F. J., & Grunthaner, P. J. (2013). Perchlorate radiolysis on Mars and the origin of martian soil reactivity. *Astrobiology*, 13(6), 515–520. <https://doi.org/10.1089/ast.2013.0999>
- Schuttlefield, J. D., Sambur, J. B., Gelwicks, M., Eggleston, C. M., & Parkinson, B. A. (2011). Photooxidation of Chloride by Oxide Minerals: Implications for Perchlorate on Mars. *Journal of the American Chemical Society*, 133(44), 17521–17523. <https://doi.org/10.1021/ja2064878>
- Shkrob, I. a., Chemerisov, S. D., & Marin, T. W. (2010). Photocatalytic decomposition of carboxylated molecules on light-exposed martian regolith and its relation to methane production on Mars. *Astrobiology*, 10(4), 425–436. <https://doi.org/10.1089/ast.2009.0433>
- Sigmund, P., Bitsensky, I. S., & Jensen, J. (1996). Molecule and cluster bombardment: energy loss, trajectories, and collision cascades. *Nuclear Instruments and Methods in Physics Research*

Section B: Beam Interactions with Materials and Atoms, 112(1–4), 1–11.
[https://doi.org/10.1016/0168-583X\(95\)01125-0](https://doi.org/10.1016/0168-583X(95)01125-0)

Steininger, H., Goesmann, F., & Goetz, W. (2012). Influence of magnesium perchlorate on the pyrolysis of organic compounds in Mars analogue soils. *Planetary and Space Science*, 71(1), 9–17. <https://doi.org/10.1016/j.pss.2012.06.015>

Stoker, C. R., & Bullock, M. A. (1997). Organic degradation under simulated Martian conditions. *J. Geophys. Res.*, 102(E5), 10881–10888. <https://doi.org/10.1029/97JE00667>

Ten Kate, I. L., Garry, J. R. C., Peeters, Z., Foing, B., & Ehrenfreund, P. (2006). The effects of Martian near surface conditions on the photochemistry of amino acids. *Planetary and Space Science*, 54(3), 296–302. <https://doi.org/10.1016/j.pss.2005.12.002>

Ten Kate, I. L., Garry, J. R. C., Peeters, Z., Quinn, R., Foing, B., & Ehrenfreund, P. (2005). Amino acid photostability on the Martian surface. *Meteoritics and Planetary Science*, 40(8), 1185. <https://doi.org/10.1111/j.1945-5100.2005.tb00183.x>

Turner, A. M., Abplanalp, M. J., & Kaiser, R. L. (2016). Mechanistic Studies on the Radiolytic Decomposition of Perchlorates on the Martian Surface. *The Astrophysical Journal*, 820(2), 127. <https://doi.org/10.3847/0004-637X/820/2/127>

Wilson, E. H., Atreya, S. K., Kaiser, R. I., & Mahaffy, P. R. (2016). Perchlorate formation on Mars through surface radiolysis-initiated atmospheric chemistry: A potential mechanism. *Journal of Geophysical Research: Planets*, 121, 1472–1487. <https://doi.org/10.1002/2015JE004832>.

Yen, A. S., Kim, S. S., Hecht, M. H., Frant, M. S., & Murray, B. (2000). Evidence that the reactivity of the martian soil is due to superoxide ions. *Science*, 289, 1909–1912. <https://doi.org/10.1126/science.289.5486.1909>

- Zheng, W., Jewitt, D., & Kaiser, R. I. (2006a). Formation of Hydrogen, Oxygen, and Hydrogen Peroxide in Electron-irradiated Crystalline Water Ice. *The Astrophysical Journal*, 639(1), 534–548. <https://doi.org/10.1086/499231>
- Zheng, W., Jewitt, D., & Kaiser, R. I. (2006b). Temperature Dependence of the Formation of Hydrogen, Oxygen, and Hydrogen Peroxide in Electron-Irradiated Crystalline Water Ice. *The Astrophysical Journal*, 648(1), 753–761. <https://doi.org/10.1086/505901>
- Ziegler, J. F., Ziegler, M. D., & Biersack, J. P. (2010). SRIM - The stopping and range of ions in matter (2010). *Nuclear Instruments and Methods in Physics Research, Section B: Beam Interactions with Materials and Atoms*, 268(11–12), 1818–1823. <https://doi.org/10.1016/j.nimb.2010.02.091>

Chapter 4

H₂ IN THE LUNAR EXOSPHERE

This chapter is based on a manuscript that has been submitted to Nature Communications for consideration. Co-authors include Crandall, P.B., Gillis-Davis, J.J., and Kaiser, R.I.

4.1 Introduction

Prior to the Apollo missions, planetary scientists suspected that the Moon possesses a tenuous atmosphere comprised of outgassed materials from the radioactive decay of minerals deep within its crust [Bernstein et al. 1963; Johnson 1971]. *In situ* measurements of the Apollo landings exploiting the cold cathode gauge experiments (CCGE) of Apollo 14 and 15 as well as the surface neutral mass spectrometer (SNMS) of Apollo 17 provided the first evidence of a lunar exosphere at a level of about 10^{-9} mbar consisting of atoms and light molecular species like argon, helium, neon, sodium, potassium, and hydrogen [Lucey 2006; Scientific and Technical Information Office National Aeronautics and Space Administration 1973; Stern 1999]. The concentration of these species varies depending on the time of day and suggests that the solar wind represents the primary source for all but a few trace elements [Colaprete et al. 2016; Sarantos et al. 2012; Feldman and Morrison 1991]. Of these volatiles, molecular hydrogen (H₂) has drawn considerable attention from the lunar science community as hydrogen is not only chemically reactive, but also represents the molecular constituent in highest abundance. The tenuous lunar atmosphere is therefore suggested to be critically connected to the formation of surface water (H₂O) and/or hydroxyl radicals (OH) - as detected via the 2.8 μ m band by the Moon Mineralogy Mapper (M³) – through exposure of silicates by the solar wind [C M Pieters et al. 2009; Clark 2009; Sunshine et al. 2009], but the inherent source of atmospheric hydrogen has been unknown so far.

As solar wind protons encounter the Moon, protons are implanted into regolith grains at energies of typically 1 to 2 keV amu⁻¹ and are also neutralized along the trajectories [Johnson 1990]. These energies result in penetration depths of up to 100 nm over which the grains become amorphized at exposure times of close to 100 years [Keller and McKay 1997]. The disruption of the crystal lattice by ionizing radiation creates lattice vacancies and interstitials that may serve as effective catalytic sites for the recombination of two hydrogen atoms to form molecular hydrogen (H₂) or a reaction between trapped hydrogen and free oxygen atoms [Chatelain, Kolopus, and Weeks 1970] to possibly form water (H₂O) and/or hydroxyl (OH) [Managadze et al. 2011]. Both mechanisms, along with the potential formation of Si-O-H functional groups, can be induced via non-equilibrium, high energy processes and by the diffusion of thermalized hydrogen atoms together with tunneling [Kuwahata et al. 2015]. At Earth's distance from the Sun, the density of solar protons is 6 to 8 H⁺ cm⁻³ traveling at an average velocity of 450 km s⁻¹, although these values vary based upon solar activity [Starukhina and Shkuratov 2000; Poppe et al. 2013]. Since the Moon only possesses an atmosphere of volatiles with virtually infinite mean free paths, i.e. an exosphere, the surface is entirely exposed to an average incident flux of about 3×10^8 H⁺ cm⁻² s⁻¹. At this rate, a saturation level of irradiation damage within a lunar regolith grain is reached after a period of only typical 100 years [Starukhina 2006]. However, micrometeorites and larger impacts garden the upper surface. The regolith reworking depth by micrometeorites is estimated to be close to 2 μm over 100 years based on numerical modeling with a 99 % chance of 100 turns [Costello, Ghent, and Lucey 2018] and ²⁶Al analyses of some lunar drill cores [Fruchter et al. 1977]. Based on the analysis of drive tube cores collected during Apollo 17, it would take approximately 14 million years for the upper centimeter to be mature [Lauer, Morris, and Gose 1978], and the upper 50 cm would be mature within approximately 450 million years [Morris 1978]. This means that on a

relatively short geologic time scale the upper tens of centimeters would be saturated with solar wind implanted hydrogen. Thus, the concentration of molecular hydrogen in the exosphere is likely in a steady state condition, which is bound by the local flux of the solar wind and the temperature of the regolith [Dana M. Hurley et al. 2017]. The source of hydrogen is affected by diurnal variation and could explain changes in hydroxyl (OH) measurements [C M Pieters et al. 2009; Clark 2009; Sunshine et al. 2009].

Here, we conduct sophisticated laboratory experiments exploiting deuterium ions as a proxy of hydrogen ions to simulate the interaction between lunar silicates and the solar wind and observe the temperature dependence of the formation of molecular deuterium from 10 K to 250 K. The exploitation of deuterium is driven by the stipulation to discriminate between products formed as a result of the irradiation (D_2) compared to residual gases in particular traces of molecular hydrogen (H_2), which are present in any vacuum chamber even under ultra-high vacuum (UHV) conditions as the result of outgassing from the stainless steel material of the recipient. The present study unravels the key role of lunar silicate minerals to efficiently store molecular deuterium and how this process depends on the temperature. The capability of silicates to store *and* to effectively release molecular deuterium upon annealing provides solid experimental evidence that the solar wind represents a potential key source of molecular hydrogen in the tenuous lunar atmosphere thus changing our perception on the origin of tenuous exospheres not only of the Moon, but of airless bodies in our Solar System in general.

4.2 Methods

To simulate the interaction of solar wind protons with the lunar regolith experimentally, we exposed powdered San Carlos olivine ($[\text{Mg}_{1.8}\text{Fe}_{0.2}]\text{SiO}_4$, $< 45 \mu\text{m}$) samples to a 5 keV D_2^+ molecular ion beam for a total fluence of $(1.17 \pm 0.06) \times 10^{18}$ deuterium nuclei cm^{-2} , equivalent to 130 ± 10 years of irradiation at the lunar surface on average, under ultra-high vacuum conditions at temperatures ranging from 10 to 250 K (Table 4.1). Olivine has been used as a typical proxy of the lunar material that has been widely used to simulate space weathering effects on the Moon [Burke et al. 2011a; Djouadi et al. 2011; Loeffler, Dukes, and Baragiola 2009; Lord 1968]. The experiments were conducted within a stainless steel ultrahigh vacuum (UHV) chamber, evacuated to $1.5 \pm 0.5 \times 10^{-10}$ torr using oil-free turbomolecular pumps backed by dry scroll pumps [Crandall et al. 2017; Turner, Abplanalp, and Kaiser 2016; Ennis et al. 2011]. Samples were prepared via grinding and dry sieving and 0.8 ± 0.1 g of material was pressed onto a silver wafer ($3.1 \times 3.1 \text{ cm}^2$). The wafer was affixed to a rotatable copper cold finger (CTI-Cryogenics Cryodyne 1020, compressor: CTI-Cryogenics 9600) and a thin layer of indium foil was placed between the silver substrate and the cold finger to ensure good thermal conductivity. A Lakeshore DT-470 silicon diode sensor mounted near the substrate was used to monitor the temperature of the sample, which can be controlled within the range of 10–300 K by a 25Ω heater cartridge powered by a Lakeshore 336 temperature controller.

A quadruply differentially pumped ion source (SPECS IQE 12/38), supplied with a 3.0×10^{-3} torr base pressure of high-purity molecular deuterium gas (D_2 : 99.999%; Icon Isotopes), produced the charged particle beam. Located after the ionization and extraction regions of the ion source, a Wien mass filter separated unwanted atomic deuterium (D^+) and trideuterium (D_3^+) ions to produce a monoenergetic beam of 5 keV molecular deuterium ions (D_2^+) directed at the

substrate. After passing through the mass filter, ions travel through three additional differentially pumped regions held at 1.2×10^{-6} , 3.5×10^{-8} , and 2.0×10^{-9} torr, which are in place to maintain a pressure of low 10^{-10} torr in the main chamber while the ion source is in operation. A Faraday cup in the main chamber measured the total ion current of the ions at the sample. This operation scans the ion beam over a sample area of $1 \times 1 \text{ cm}^2$ at a current of $2,000 \pm 100 \text{ nA}$. As described in Section 3.2 of this thesis, the use of deuterium ions is to distinguish between products formed as a result of irradiation in contrast to contaminate residual gases present in any ultra-high vacuum. With our particular ion source, molecular deuterium (D_2^+) ions are readily produced at fluxes higher than three orders of magnitude compared to D^+ ions. However, Sigmund *et al.* [1996] established that upon impact on the olivine surface, each molecular ion (D_2^+) dissociates *quantitatively* into a D atom and D^+ implant possessing 2.5 keV kinetic energy on average each. This energy correlates nicely with the range of the kinetic energy of solar wind particles of 1 – 2 keV amu^{-1} .

Table 4.1 Parameters for the ion irradiation source.

Kinetic energy of the ions (keV)	5.0
Ion flux ($\text{cm}^{-2} \text{s}^{-1}$)	$(1.25 \pm 0.06) \times 10^{13}$
Irradiated area (cm^2)	1.10 ± 0.2
Irradiation time (min)	780
Total deuterium nuclei (cm^{-2})	$(1.17 \pm 0.06) \times 10^{18}$
Solar wind proton flux on Moon ($\text{cm}^{-2} \text{s}^{-1}$) *	$(3.0 \pm 0.5) \times 10^8$
Simulated time (year)	130 ± 10

*[Blanford et al. 1986]

A Balzer QMG 422 electron impact quadrupole mass spectrometer (EI-QMS) operating in the residual gas analyzer mode with electron impact energies of 100 eV at a 0.7 mA emission current and secondary electron multiplier (SEM) operated at 3,000 V was used to quantify the deuterium yield with the help of a leak valve. A positive shut-off capillary calibrated leak valve (Vacuum Technologies Incorporated) was connected to a deuterium gas reservoir and to the ultra-high vacuum chamber; this device provided a stable leak rate of 1.12×10^{-6} Torr L s⁻¹ of deuterium gas into the chamber. The number of leaked deuterium molecules (n_{D_2}) is determined by equation (4.1), where R and T represent the gas constant (8.314 J K⁻¹ mol⁻¹) and temperature (293 K), respectively.

4.1

$$n_{D_2} = \frac{\int_0^t Q dt}{RT}$$

The proportionality constant (K_{QMS}) between the number of deuterium molecules (n_{D_2}) and the molecular ion current in A ($m/z = 4$, I_{D_2}) profile is defined via equation (4.2) with the time t in s and was determined to be $8.95 \pm 0.24 \times 10^{19}$ molecules C⁻¹:

4.2

$$K_{QMS} = \frac{n_{D_2}}{\int_0^t I_{D_2} dt}$$

The deuterium molecules detected during the TPD in the gas phase ($n_{D_2}(TPD)$) was derived based on this constant and the current of the $m/z = 4$ signal measured by the SEM of the mass spectrometer ($I_{D_2}(TPD)$) via equation (4.3):

$$n_{D_2}(TPD) = K_{QMS} \int_0^t I_{D_2}(TPD) dt$$

Ion trajectories were modeled using the Stopping and Range of Ions in Matter (SRIM) Monte Carlo program [Ziegler et al. 2010]. A density of 3.35 g/cm^3 was used for San Carlos olivine ($[\text{Mg}_{1.8}\text{Fe}_{0.2}]\text{SiO}_4$) and the layer was given a width of 300 nm. Deuterium was selected for the simulated ions with a mass of 2 amu and an energy of 2.5 keV. To calculate the damage of the substrate and the implantation profile, we selected “Detailed Calculation with Full Damage Cascades” for the TRIM calculation method and simulated a total of 99,999 trajectories. Results of these simulations calculated the average penetration depth to be $39 \pm 4 \text{ nm}$ (Figure 4.4).

4.3 Lunar Environment Simulations

Six sets of experiments were carried out where the olivine sample was held isothermally during the irradiation at 10, 40, 80, 120, 200, and 250 K, after which the sample was heated to 300 K at a ramp rate of 1 K min^{-1} (temperature programmed desorption; TPD). During this period, the controlled heating of the sample induces the diffusion of deuterium atoms, which are trapped within the olivine during irradiation, and also of molecular deuterium. During this process, deuterium atoms can recombine to molecular deuterium with the excess energy from the formation of a deuterium-deuterium bond released to the surrounding mineral thus stabilizing molecular deuterium. As these volatiles diffuse out of the sample, the gases are ionized via electron impact by a quadrupole mass spectrometer (QMS) yielding a mass-to-charge (m/z) ion signal (current) at $m/z = 4$ that is directly proportional to the partial pressure and hence number density of each species in the gas phase. The results from this TPD are compared to blank experiments, in which all experimental conditions are repeated save that no ion beam is introduced to the chamber.

Figure 4.1a depicts the results from the TPD phase plotting the signal at $m/z = 4$, which is assigned to the formation of molecular deuterium (D_2), at distinct temperatures. No molecular deuterium formation was observed in the blank experiments during the TPD phase revealing that deuterium gas from the ion source chamber does not contribute to any background signal. These graphs visualize qualitatively that as the temperature increases from 10 K to 250 K, less molecular deuterium is being released from the minerals during the warm up into the gas phase. This in turn suggests that as the temperature rises, the capability of the silicate to store molecular deuterium is diminished. Since our QMS is calibrated, we integrated the signal intensity at $m/z = 4$ to quantify the total amount of deuterium molecules produced during the TPD phase (Figure 4.1b, solid line). The data points could be fitted using the function defining the number of molecules (N) as $N = (1.80 \times 10^{16})e^{-\frac{T}{58.02}} - 1.87 \times 10^{13}$, where T defines the irradiation temperature in Kelvin (K). The results support the aforementioned qualitative observations. As the irradiation temperature increases, the production of molecular deuterium and hence capability to store deuterium in the silicates decreases. Since the diffusion of atomic and molecular deuterium within the silicate is enhanced as the temperature is raised, the reduced storage yield at higher irradiation temperatures is likely the effect of an enhanced diffusion of atomic deuterium and reaction to molecular deuterium followed by diffusion of the latter out of the silicates into the gas phase during the irradiation. This in turn leaves fewer deuterium atoms and molecules to be stored inside the minerals at, for instance, 250 K versus 10 K. Further, accounting for the irradiation current, exposure time, and average backscattering of the ions calculated by SRIM, we determine the total number of deuterium nuclei implanted into the silicate target to be $1.09 \pm 0.05 \times 10^{18}$. $1.49 \pm 0.27 \times 10^{16}$ deuterium molecules were detected thus equating to an efficiency of $2.73 \pm 0.51 \%$ of the deuterium storage at 10 K as derived from the gas phase deuterium molecules. Finally, it is

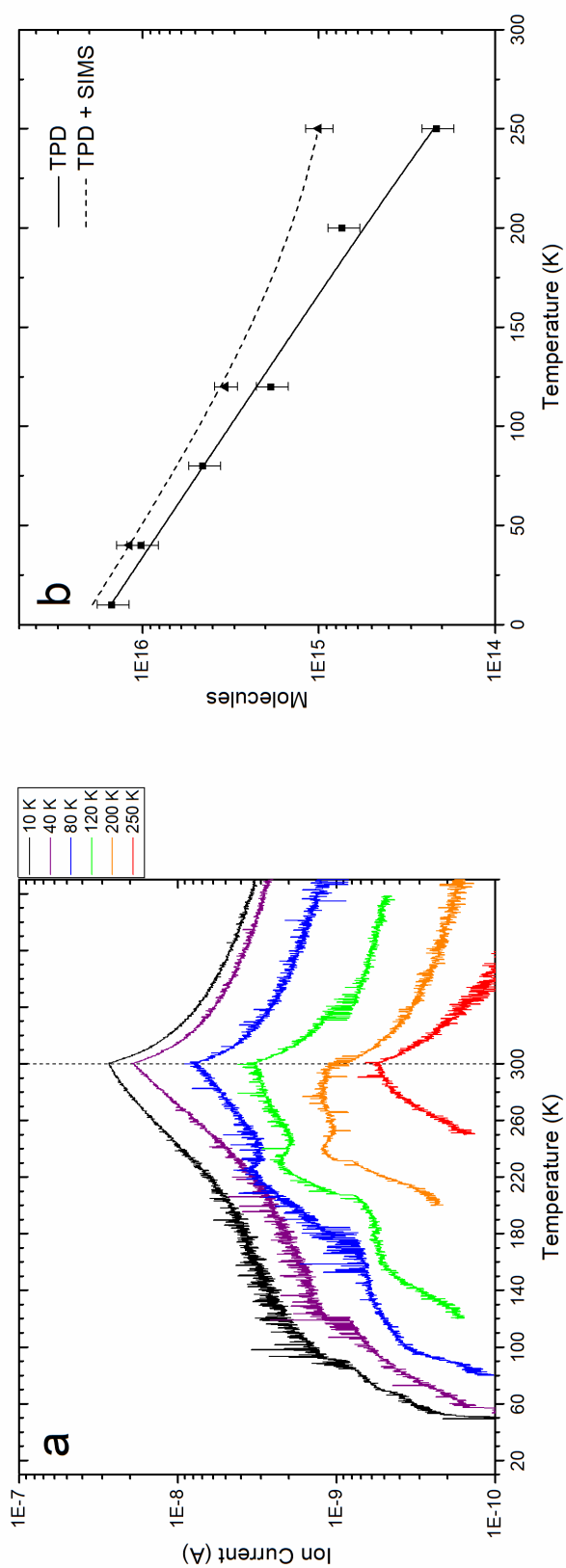


Figure 4.1 (a) Quantification of molecular deuterium detected via the parent molecular ion at mass-to-charge $m/z = 4$ as a function of irradiation temperature. After the irradiation, each sample underwent TPD to 300 K (dotted line). (b) Total number of deuterium molecules detected during TPD (solid line) from various irradiation temperatures as derived by integration of signal at mass-to-charge $m/z = 4$ exploiting a calibrated mass spectrometer. The addition contributions of trapped deuterium at 300 K are represented as a dashed line. The error bars were calculated based on the uncertainty of the of irradiation flux and error propagation of the calibration of the mass spectrometer.

important to note that in each experiment, no increase in the signal of $m/z = 20$ (D_2O) compared to the blank was observed in the irradiation and TPD phases. Consequently, if deuterated water formed from the interaction of deuterium ions with olivine and diffused out of the sample, it is below the detection limit of the spectrometer of approximately 10^8 molecules s^{-1} .

Table 4.2 Quantified deuterium molecules (N) in the TPD phase.

Irradiation Temperature (K)	Deuterium Molecules (N)	Percentage Efficiency*
10 (Blank)	N/A	N/A
10	$(1.49 \pm 0.27) \times 10^{16}$	2.55 ± 0.47
40	$(1.02 \pm 0.18) \times 10^{16}$	1.74 ± 0.32
80	$(4.54 \pm 0.81) \times 10^{15}$	0.78 ± 0.14
120	$(1.87 \pm 0.33) \times 10^{15}$	0.32 ± 0.06
200	$(7.35 \pm 1.30) \times 10^{14}$	0.13 ± 0.02
250	$(2.15 \pm 0.38) \times 10^{14}$	0.04 ± 0.01

*number of detected deuterium molecules (TPD phase) divided by the implanted molecular deuterium ions multiplied by 100.

4.4 Ion Microprobe Analysis of Irradiated Grains

Having detected molecular deuterium in the TPD phase, we are exploring now if the silicates still store deuterium at 300 K. Three samples, which were irradiated at temperatures relevant to the lunar surface at high to mid latitudes (40, 120, and 250 K), were analyzed by a CAMECA SIMS 1280 ion microprobe to measure the $D/^{18}O$ ratio as a function of depth (Figure 4.2). Cesium ions (Cs^+) were rastered over eight analysis sites per sample with a $50 \times 50 \mu m^2$ area

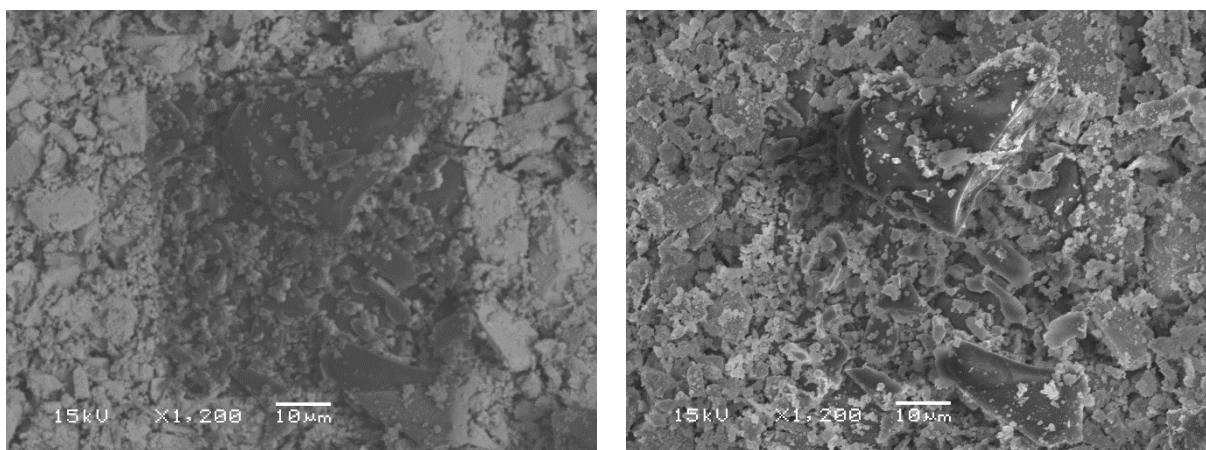


Figure 4.2 Backscattered (left) and secondary (right) electron analysis of a representative SIMS site of the irradiated sample. These images were utilized to identify regions of uniform composition and topography when extracting depth profile data for comparing deuterium storage in the samples.

while sputtered material was monitored for concentrations of D and ^{18}O for 200 cycles. These investigations revealed that ^{18}O concentrations were stable regardless of depth so a D/ ^{18}O ratio provides the most accurate results to determine the depth-dependent deuterium concentrations. Up to 80 profiles from each sample were averaged and compared (Figure 4.3). A comparison of the peak maxima of the depth profiles with the results from the SRIM Monte Carlo calculations suggests a sputtering rate of about 1 nm per cycle. Taking an average value of the D/ ^{18}O ratio over the range for each profile, the amount of deuterium atoms still trapped inside the samples at the time of SIMS analysis can be quantified (Figure 4.4).

These observations can be rationalized by the following arguments. First, the width of the simulated depth profile (SRIM) is narrower than the experimentally obtained profiles at 40, 120, and 250 K. This is likely the effect of the thermal diffusion of the deuterium atoms within the minerals. SRIM does not include temperature dependent, thermal diffusion processes, but only energy transfer processes from the implant to the atoms in the solid within the binary collision

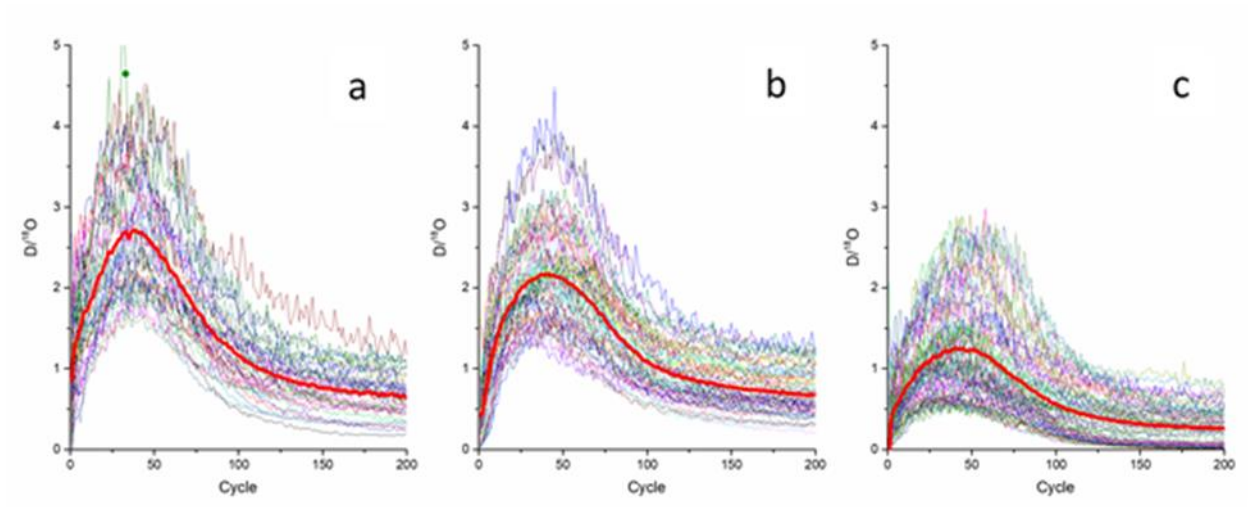


Figure 4.3 Depth profiles of $\delta D/^{18}O$ ratios taken from samples irradiated by D_2^+ ions at 40 K (a), 120 K (b), and 200 K (c). The sites were selected using SEM images to find grains with smooth surfaces normal to the incident Cs^+ ions of the microprobe.

approximation at 0 K [Ziegler, Ziegler, and Biersack 2010]. This in turn terminates the trajectory of the implant at a defined kinetic energy of 0.5 eV; at this time, the implanted species comes to rest in the simulated solid. However, under ‘real’ conditions, these species diffuse thus leading to a broader distribution compared to the SRIM simulated profile. The inward diffusion of deuterium in particular is observed experimentally in all three samples revealing significant sputtering yields at depths beyond 100 nm, i.e. the maximum penetration depth determined by SRIM calculations. Second, the sputtering profiles reveal that as the temperature is lowered from 250 K to 40 K, the more deuterium is retained in the silicates. This result correlates with the aforementioned finding that with increasing temperature, the diffusion of deuterium throughout the solid and release into the gas phase translates into a significantly reduced storage capacity of the silicates as the temperature of the silicates is enhanced. Second, accounting for the irradiation area, the density of the olivine, the $D/^{18}O$ ratio, the calculated penetration depth, and the fraction of naturally occurring ^{18}O (Table 4.1; Figure 4.2), the amount of deuterium still trapped in the samples at 300 K can be

determined and added to the deuterium released in the TPD phase (Tables 4.2 and 4.3). The overall yields are plotted in Figure 4.1b (dashed line) and can be fitted with the function $N = (2.19 \times 10^{16})e^{-\frac{-T}{59.8}} + 6.73 \times 10^{14}$ with N defining the number of deuterium molecules and T the temperature in Kelvin.

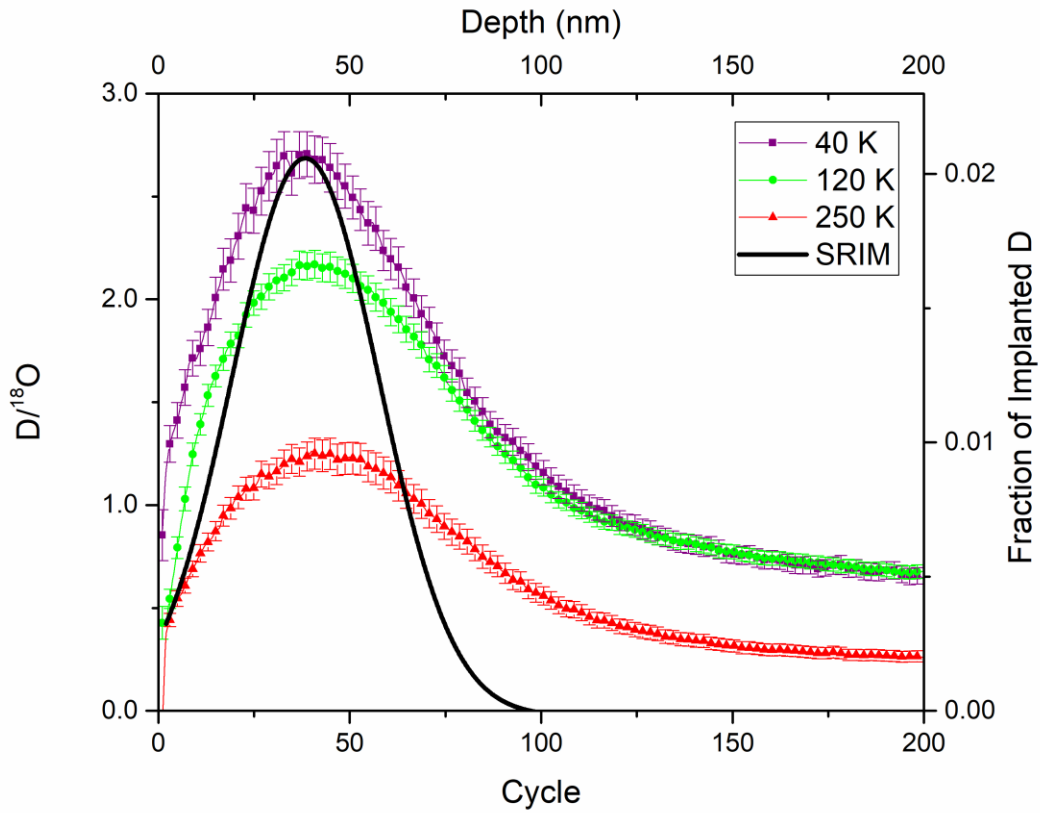


Figure 4.4 Depth profiles of the D/¹⁸O ratio determined by SIMS for samples irradiated at 40 K, 120 K, and 250 K, with error bars shown as the standard error of the mean. These profiles are compared with the calculated irradiation depth profile from SRIM (black curve) of implanted deuterium ions in olivine. The sputtering rate is determined to be close to 1 nm per cycle.

Table 4.3 Parameters for the quantification of D₂ trapped in samples at 300 K via SIMS

Density (g/cm ³)	3.36 ± 0.20		
Molar Mass (g/mol)	146.40		
Irradiated area (cm ²)	1.1 ± 0.2		
Depth of SIMS site (m)	$(2.00 \pm 0.40) \times 10^{-5}$		
Exposed volume (cm ³)	$(2.20 \pm 0.48) \times 10^{-5}$		
Mass of olivine (g)	$(7.38 \pm 0.16) \times 10^{-5}$		
¹⁸ O atoms in exposed volume	$(2.45 \pm 0.54) \times 10^{15}$		
O atoms in exposed volume	$(1.21 \pm 0.27) \times 10^{18}$		
	40 K	120 K	250 K
Average D/ ¹⁸ O ratio	1.41 ± 0.49	1.24 ± 0.29	0.65 ± 0.16
Deuterium molecules stored	$(1.72 \pm 0.42) \times 10^{15}$	$(1.52 \pm 0.39) \times 10^{15}$	$(7.92 \pm 2.20) \times 10^{14}$

4.5 Discussion and Conclusion

The present study provides compelling evidence and authenticates the proof-of-concept on the formation, storage, and liberation of molecular deuterium in and from olivine upon deuterium ion implantation over the range of 10 K to 250 K effectively simulating solar proton implantation into lunar silicates over a time span of 130 ± 10 years. In the lunar environment, surface temperatures can range from 26 K in permanently shadowed craters near the poles [Vasavada et al. 2012] to 380 K in equatorial regions at midday [Paige et al. 2010]. As evidenced by the SIMS analysis, even at 300 K, the ion implanted olivine still stores deuterium thus expecting that even at the highest lunar temperatures, the regolith grains would still be highly hydrogen enriched. This was found to be the case with regolith samples returned from the Apollo missions [Hintenberger et al. 1970]. On the Moon, the thermal processing of the regolith as the night cycles to day allows trapped hydrogen atoms to diffuse through the silicate thus recombining to molecular hydrogen

(H₂) that contributes to the total concentration of molecular hydrogen in the lunar exosphere. These investigations signify the first step toward a systematic comprehension on the formation and release of molecular hydrogen from lunar silicates and its contribution to the lunar exosphere. As for every simulation study, no single laboratory experiment can mimic the chemical and physical complexity of the lunar environment simultaneously. The laboratory simulation experiments reveal a fraction of deuterium conversion from the solar wind proxy to molecular deuterium of up to 3.51 ± 0.55 % accounting for the deuterium released in the TPD phase and stored at 300 K as determined via the SIMS analysis. This yield is lower than the estimated efficiency by Hurley et. al [2017] proposing that at close to 10 % of the incoming solar wind protons would need to be converted to molecular hydrogen (H₂) to account for the observed molecular hydrogen density of $1,200 \text{ cm}^{-3}$ in the lunar exosphere. However, the kinetic energy distribution of hydrogen as it leaves represents a critical unknown in Hurley's model; this might critically reduce the required yield to a few per cent as observed experimentally in our study.

The aforementioned data demonstrate also that the irradiated olivine in our simulation experiments still stores deuterium at 300 K, which can be released by micrometeorite impact on the lunar surface reaching peak temperatures of close to 1,500 K. Lord [1968] demonstrated that for single-crystal San Carlos olivine nodules irradiated with 2 keV protons at 300 K, the release of trapped hydrogen continues well above 800 K. The author suggested that protons are neutralized upon impact and may bond to oxygen atoms in the lattice forming hydroxyl functional groups as supported by more recent infrared studies [Managadze et al. 2011]. Demyk et. al [2004] exposed that the irradiation of crystalline silicates with 10 keV H⁺ ions at a fluence of $10^{18} \text{ ions cm}^{-2}$ resulted in changes of the infrared spectrum with two bands emerging at 9.7 – 10.3 μm and 17 – 18 μm as attributed to the stretching and bending modes of the Si–O and O–Si–O bands in

amorphized silicates. Experiments by Schaible et. al [2014a] revealed that the irradiation of San Carlos olivine with 5 keV H^+ ions at 250 K produced a broad band at 2.8 μm , which is characteristic of O–H stretching. By calculating the column density of the OH functional groups formed during irradiation, it was determined that the OH yield per implanted ion is initially as high as 0.9 OH bonds/proton and decreases to a saturation point at higher fluences. Thus, to release the chemically bound hydrogen, higher temperatures than those necessary for diffusion alone are required to break the O–H bonds. Further experiments are clearly necessary to explore the question how the conversion yield depends on the texture, grain size, and chemical composition of the silicates within the lunar soil. Likewise, energetic solar photons and in particular heavier solar wind ions, although having fluxes at least one order of magnitude lower than solar wind protons, pre-damage the silicates thus generating defects in which hydrogen might be stored more efficiently. In addition, constraints on the average concentration of stored hydrogen in the lunar regolith are still largely misrepresented. Novel methods measuring protons ejected by galactic cosmic rays are expected to promote a better understanding of the diurnal variation of hydrogen on the surface of the moon [Schwadron et al. 2018].

Nevertheless, despite these open questions, our proof-of-concept study defines a critical benchmark toward a better comprehension on the origin, storage, and release of hydrogen in lunar silicates and its contribution to the lunar exosphere and on other airless bodies in our Solar System such as Mercury. These data also reveal that cold traps on the Moon store molecular hydrogen more efficiently than regions at elevated temperatures (Fig. 4.1b) thus providing a possible explanation of the low neutron albedo of the cold traps in the Moon as observed by the Lunar Crater Observation and Sensing Satellite (LCROSS) where subsurface temperatures are estimated to be 38 K [Paige et al. 2010].

4.6 References

- Bernstein, W., R. W. Fredricks, J. L. Vogl, and William A. Fowler. 1963. “The Lunar Atmosphere and the Solar Wind.” *Icarus* 2 (C): 233–48. doi:10.1016/0019-1035(63)900204.
- Biersack, J. P., and J. F. Ziegler. 1982. “The Stopping and Range of Ions in Solids.” In *Ion Implantation Techniques*. doi:10.1007/978-3-642-68779-2_5.
- Blanford, G., Børgesen, P., Maurette, M., Möller, W. & Monart, B. “On-line” analyses of simulated solar wind implantations of terrestrial analogs of lunar materials. *J. Geophys. Res.-Sol. Ea.* **91**, 467-472, (1986)
- Burke, D. J., C. A. Dukes, J. H. Kim, J. Shi, M. Famá, and R. A. Baragiola. 2011. “Solar Wind Contribution to Surficial Lunar Water: Laboratory Investigations.” *Icarus*. doi:10.1016/j.icarus.2010.11.007.
- Chatelain, A., J. L. Kolopus, and R. A. Weeks. 1970. “Radiation Effects and Oxygen Vacancies in Silicates.” *Science* 168 (3931): 570–71. doi:10.1126/science.168.3931.570.
- Clark, Roger N. 2009. “Detection of Adsorbed Water and Hydroxyl on the Moon.” *Science* (New York, N.Y.) 326 (5952): 562–64. doi:10.1126/science.1178105.
- Colaprete, A., M. Sarantos, D. H. Wooden, T. J. Stubbs, A. M. Cook, and M. Shirley. 2016. “Lunar Atmosphere: How Surface Composition and Meteoroid Impacts Mediate Sodium and Potassium in the Lunar Exosphere.” *Science* 351 (6270): 219–52. doi:10.1126/science.aad2380.
- Costello, Emily S., Rebecca R. Ghent, and Paul G. Lucey. 2018. “The Mixing of Lunar Regolith:

Vital Updates to a Canonical Model.” *Icarus*, accepted.

Crandall, Parker B., Sándor Góbi, Jeffrey Gillis-Davis, and Ralf I. Kaiser. 2017. “Can Perchlorates Be Transformed to Hydrogen Peroxide (H₂O₂) Products by Cosmic Rays on the Martian Surface?” *Journal of Geophysical Research: Planets*. doi:10.1002/2017JE005329.

Demyk, K., L. D’Hendecourt, H. Leroux, A. P. Jones, and J. Borg. 2004. “IR Spectroscopic Study of Olivine, Enstatite and Diopside Irradiated with Low Energy H⁺ and He⁺ Ions.” *Astronomy & Astrophysics* 420: 233–43. doi:10.1051/0004-6361:20040091.

Djouadi, Z., F. Robert, L. Le Sergeant d’Hendecourt, S. Mostefaoui, H. Leroux, a. P. Jones, and J. Borg. 2011. “Hydroxyl Radical Production and Storage in Analogues of Amorphous Interstellar Silicates: A Possible ‘Wet’ Accretion Phase for Inner Telluric Planets.” *Astronomy & Astrophysics* 531: A96. doi:10.1051/0004-6361/201116722.

Ennis, Courtney, Chris J Bennett, Brant M Jones, and Ralf I Kaiser. 2011. “Formation of D₂-Water and D₂-Carbonic Acid in Oxygen-Rich Solar System Ices Via D₂⁺ Irradiation.” *Astrophysical Journal* 733 (2). doi:10.1088/0004-637x/733/2/79.

Feldman, Paul D., and Daniel Morrison. 1991. “The Apollo 17 Ultraviolet Spectrometer: Lunar Atmosphere Measurements Revisited.” *Geophysical Research Letters* 18 (11): 2105–8. doi:10.1029/91GL01998.

Fruchter, J S, L A Rancitelli, R W Perkins, and J C Laul. 1977. “Lunar Regolith Dynamics Based on Analysis of the Cosmogenic Radionuclides Na-22, Al-26, and Mn-53.” *Lunar Science Conference*.

Hintenberger, H., H . W . Weber, H . Voshage, H . Wänke, F . Begemann, E . Vilscek, and F . Wlotzka. 1970. “Rare Gases , Hydrogen , and Nitrogen : Concentrations and Isotopic

- Composition in Lunar Material.” *Science* 167 (3918): 543–45.
- Hurley, Dana M., Jason C. Cook, Kurt D. Retherford, Thomas Greathouse, G. Randall Gladstone, Kathleen Mandt, Cesare Grava, et al. 2017. “Contributions of Solar Wind and Micrometeoroids to Molecular Hydrogen in the Lunar Exosphere.” *Icarus* 283: 31–37. doi:10.1016/j.icarus.2016.04.019.
- Johnson, Francis S. 1971. “Lunar Atmosphere.” *Reviews of Geophysics* 9 (3): 813–23. doi:10.1029/RG009i003p00813.
- Johnson, Richard E. 1990. “Energetic Charged-Particle Interactions with Atmospheres and Surfaces.” *Physics and Chemistry in Space* ; v. 19. Berlin: Springer-Verlag. doi:10.1007/978-3-642-48375-2.
- Keller, Lindsay P, and David S Mckay. 1997. “The Nature and Origin of Rims on Lunar Soil Grains.” *Geochimica et Cosmochimica Acta* 61 (I): 2311–41. doi:10.1016/S0016-7037(97)00085-9.
- Kuwahata, K, T Hama, A Kouchi, and N Watanabe. 2015. “Signatures of Quantum-Tunneling Diffusion of Hydrogen Atoms on Water Ice at 10 K.” *Physical Review Letters* 115 (13). American Physical Society: 133201. doi:10.1103/PhysRevLett.115.133201.
- Lauer H. V., Jr., R V Morris, and W A Gose. 1978. “Depositional and Surface Exposure History of the Shorty Crater Core 74001/2 - FMR and Magnetic Studies.” *Lunar and Planetary Science Conference*.
- Loeffler, M. J., C. A. Dukes, and R. A. Baragiola. 2009. “Irradiation of Olivine by 4 KeV He⁺: Simulation of Space Weathering by the Solar Wind.” *Journal of Geophysical Research E: Planets* 114 (3). doi:10.1029/2008JE003249.

- Lord, H C. 1968. "Hydrogen and Helium Ion Implantation into Olivine and Enstatite - Retention Coefficients Saturation Concentrations and Temperature-Release Profiles." *Journal of Geophysical Research* 73 (16): 5271-. doi:Doi 10.1029/Jb073i016p05271.
- Lucey, P. 2006. "Understanding the Lunar Surface and Space-Moon Interactions." *Reviews in Mineralogy and Geochemistry*. doi:10.2138/rmg.2006.60.2.
- Managadze, G.G., V.T. Cherepin, Y.G. Shkuratov, V.N. Kolesnik, and a.E. Chumikov. 2011. "Simulating OH/H₂O Formation by Solar Wind at the Lunar Surface." *Icarus* 215 (1): 449–51. doi:10.1016/j.icarus.2011.06.025.
- Morris, R V. 1978. "In Situ Reworking /Gardening/ of the Lunar Surface - Evidence from the Apollo Cores." *Lunar and Planetary Science Conference*.
- Paige, D. A., M. C. Foote, B. T. Greenhagen, J. T. Schofield, S. Calcutt, A. R. Vasavada, D. J. Preston, et al. 2010. "The Lunar Reconnaissance Orbiter Diviner Lunar Radiometer Experiment." *Space Science Reviews* 150 (1–4): 125–60. doi:10.1007/s11214-009-9529-2.
- Paige, David A., Matthew A. Siegler, Jo Ann Zhang, Paul O. Hayne, Emily J. Foote, Kristen A. Bennett, Ashwin R. Vasavada, et al. 2010. "Diviner Lunar Radiometer Observations of Cold Traps in the Moon's South Polar Region." *Science*. doi:10.1126/science.1187726.
- Pieters, C M, J N Goswami, R N Clark, M Annadurai, J Boardman, B Buratti, J-P P. Combe, et al. 2009. "Character and Spatial Distribution of OH/H₂O on the Surface of the Moon Seen by M3 on Chandrayaan-1." *Science* 326 (5952): 568–72. doi:10.1126/science.1178658.
- Poppe, A. R., J. S. Halekas, M. Sarantos, and G. T. Delory. 2013. "The Self-Sputtered Contribution to the Lunar Exosphere." *Journal of Geophysical Research: Planets* 118 (9): 1934–44. doi:10.1002/jgre.20148.

- Sarantos, M., R. E. Hartle, R. M. Killen, Y. Saito, J. A. Slavin, and A. Glocer. 2012. "Flux Estimates of Ions from the Lunar Exosphere." *Geophysical Research Letters* 39 (13): 6–11. doi:10.1029/2012GL052001.
- Schaible, Micah J., and Raúl A. Baragiola. 2014. "Hydrogen Implantation in Silicates: The Role of Solar Wind in SiOH Bond Formation on the Surfaces of Airless Bodies in Space." *Journal of Geophysical Research: Planets* 119: 2017–28. doi:10.1002/2014JE004650.
- Schwadron, N.A., J.K. Wilson, A.P. Jordan, M.D. Looper, C. Zeitlin, L.W. Townsend, H.E. Spence, et al. 2018. "Using Proton Radiation from the Moon to Search for Diurnal Variation of Regolith Hydrogenation." *Planetary and Space Science* 162 (November). Pergamon: 113–32. doi:10.1016/J.PSS.2017.09.012.
- Scientific and Technical Information Office National Aeronautics and Space Administration. 1973. "Apollo 17: Preliminary Science Report." Washington, DC.
- Sigmund, P., I.S. Bitsensky, and J. Jensen. 1996. "Molecule and Cluster Bombardment: Energy Loss, Trajectories, and Collision Cascades." *Nuclear Instruments and Methods in Physics Research Section B: Beam Interactions with Materials and Atoms* 112 (1–4): 1–11. doi:10.1016/0168-583X(95)01125-0.
- Starukhina, L. V. 2006. "Polar Regions of the Moon as a Potential Repository of Solar-Wind-Implanted Gases." *Advances in Space Research* 37 (1): 50–58. doi:10.1016/j.asr.2005.04.033.
- Starukhina, Larissa V., and Yuriy G. Shkuratov. 2000. "The Lunar Poles: Water Ice or Chemically Trapped Hydrogen?" *Icarus* 147 (2): 585–87. doi:10.1006/icar.2000.6476.
- Stern, S A. 1999. "The Lunar Atmosphere: History, Status, Current Problems, and Context." *Rev.*

Geophys. 37(4): 453–491. doi:10.1029/1999RG900005.

Sunshine, Jessica M., Tony L. Farnham, Lori M. Feaga, Olivier Groussin, Frédéric Merlin, Ralph E. Milliken, and Michael F. A'Hearn. 2009. "Temporal and Spatial Variability of Lunar Hydration as Observed by the Deep Impact Spacecraft." *Science* 326 (5952): 565–68. doi:10.1126/science.1179788.

Turner, A.M., M.J. Abplanalp, and R.L. Kaiser. 2016. "Mechanistic Studies on the Radiolytic Decomposition of Perchlorates on the Martian Surface." *The Astrophysical Journal* 820 (2): 127. doi:10.3847/0004-637X/820/2/127.

Vasavada, Ashwin R., Joshua L. Bandfield, Benjamin T. Greenhagen, Paul O. Hayne, Matthew A. Siegler, Jean Pierre Williams, and David A. Paige. 2012. "Lunar Equatorial Surface Temperatures and Regolith Properties from the Diviner Lunar Radiometer Experiment." *Journal of Geophysical Research E: Planets* 117 (4): 1–12. doi:10.1029/2011JE003987.

Ziegler, James F., M. D. Ziegler, and J. P. Biersack. 2010. "SRIM - The Stopping and Range of Ions in Matter (2010)." *Nuclear Instruments and Methods in Physics Research, Section B: Beam Interactions with Materials and Atoms* 268 (11–12): 1818–23. doi:10.1016/j.nimb.2010.02.091.

Chapter 5

LUNAR WATER FROM SOLAR WIND AND MICROMETEORITES

This chapter is based on a manuscript currently under review. As a co-first author, Cheng Zhu made significant contributions to the writing of this chapter. Co-authors include Zhu, C., Crandall, P.B., Gillis-Davis, J.J., Ishii, H., Bradley, J., Corley, L., and Kaiser, R.I.

5.1 Water on the Moon

The unraveling of the formation and liberation of water in lunar silicates is critical in aiding our fundamental understanding of the water cycle on the Moon - in particular whether lunar water ices are primordial water expelled from the interior of the Moon by geologic processes [Saal et al. 2008; Needham and Kring 2017], delivered via comets and water-rich asteroids [Berezhnoi and Klumov 1998; Ong et al. 2010; Greenwood et al. 2010; Stewart et al. 2011], or produced *in-situ* in the lunar regolith by bombardment of oxygen-rich silicate minerals by solar wind protons (H^+) at energies of about 1 to 2 keV [Zeller, Ronca, and Levy 1966]. Although the origin of water on the Moon is still a mystery, during the past two decades, the presence of lunar water ice was suggested based on radar (Clementine, Arecibo) [Nozette et al. 1996; Stacy, Campbell, and Ford 1997] and neutron spectrometer data (Lunar Prospector) [Feldman et al. 1998]. The identification of lunar water culminated in the Lunar Crater Observation and Sensing Satellite excavation of water ice from the permanently-shadowed crater Cabeus [Colaprete et al. 2010] along with the first spectroscopic observation of surface exposed water ice (Chandrayaan-1) [Li et al. 2018]. Further, three independent spacecraft instruments detected absorption bands at 3 μm to identify H_2O/OH in polar regions (Moon Mineralogy Mapper (M^3), Chandrayaan-1 [C M Pieters et al. 2009; Li and Milliken 2017; Milliken and Li 2017]; Visual and Infrared Mapping Spectrometer (VIMS), Cassini

[Clark 2009]; High Resolution Instrument–Infrared Spectrometer (HRI-IR), Deep Impact [Sunshine et al. 2009]. Recent Earth-based telescopic observations of lunar surface water [Honniball et al. 2018] revealed fascinating latitude and time-of-day systematics consistent with measurements by Cassini [Clark 2009] and Deep Impact [Sunshine et al. 2009].

The data from the M³ mission - revealing that H₂O/OH is present on the Moon at all latitudes at a given local time and terrain type [Li and Milliken 2017; Honniball et al. 2018; Bandfield et al. 2018] - strongly implicate the involvement of solar wind protons in the production of water. However, laboratory experiments, which attempted to unravel the solar wind induced synthesis of H₂O/OH in lunar silicates, yielded conflicting findings. Experiments conducted under high vacuum conditions between 10⁻⁸ and 10⁻⁶ torr observed either an $\nu(\text{O-H})$ stretching mode in the 2.70 μm (3700 cm⁻¹) to 3.33 μm (3000 cm⁻¹) region exploiting infrared spectroscopy [Ichimura et al. 2012; Yoshida et al. 2004] along with secondary-ion mass spectrometry (SIMS) [Managadze et al. 2011] and Valence Electron Energy Loss Spectroscopy (VEEL) [Bradley et al. 2014]. However, contradictory studies yielded no evidence of H₂O/OH in proton bombarded minerals once these experiments were performed under ultrahigh vacuum (10⁻¹⁰ to 10⁻⁹ torr) [Burke et al. 2011b]. Orlando et al. [2018] proposed that proton bombardment of lunar regolith simulants produces chemically bound hydroxyl (–OH) groups as potential precursors to water at elevated temperatures of at least 450 K - well above the equilibrium temperature of the sunlit Moon of 400 K. The authors concluded that solar proton irradiation of lunar regolith does not contribute significantly to the origin of water. Therefore, despite compelling evidence on the presence of water and/or hydroxyl radicals in the lunar soil, an intimate understanding of the underlying pathways to form and release lunar water from the silicates and how its abundance might vary on diurnal time scales is still in its infancy.

In this chapter, we uncover via laboratory simulation experiments combined with imaging analysis a versatile pathway to generate and liberate water in lunar silicates by synergistic effects of solar wind proton implantation combined with thermal excursion events such as micrometeorite impacts, but not by proton implantation alone. This is achieved by exploiting deuterium ions as a proxy of hydrogen ions of the solar wind to simulate the interaction with anhydrous olivine ($[\text{Mg,Fe}]_2\text{SiO}_4$) - a typical surrogate of the lunar material that has been widely used to simulate space weathering effects on the Moon [Managadze et al. 2011; Sasaki et al. 2001; Schaible and Baragiola 2014] – over a temperature range of 10 K to 300 K followed by thermal shock processing of the irradiated silicates to mimic heating effect of micrometeorite impacts under ultra-high vacuum conditions. These studies disclose systematically the capability of lunar silicates to first efficiently store water from ion implantation over a broad temperature range from 10 K to 300 K and the key role of a successive thermal shock exposure of the irradiated silicates to release water into the gas phase. The intertwined solar wind processing followed by micrometeorite impact provides compelling evidence on the decisive contribution of thermal shocks to liberate water from solar wind implanted minerals thus revolutionizing our understanding of the origin and distribution of water on the Moon and on airless bodies in our Solar System such as Mercury and asteroids.

5.2 Methods

The experiments were carried out in the SSM, a contamination-free, ultrahigh vacuum, stainless chamber, which is evacuated to 2×10^{-10} Torr by using two magnetically suspended turbo molecular pumps backed by an oil-free scroll pump [Bennett, Jamieson, Mebel, and Kaiser 2004]. San Carlos olivine powder ($[\text{Mg}_{1.8}\text{Fe}_{0.2}]\text{SiO}_4$) with grain sizes of less than 45 μm was pressed on

a polished silver mirror interfaced via indium foil for thermal conductivity to a rotatable oxygen-free high conductivity copper cold finger attached to a two-stage, closed-cycle helium compressor (CTI-Cryogenics Cryodyne 1020, compressor: CTI-Cryogenics 9600). A silicon diode sensor (Lakeshore DT-470) was fixed to the cold finger near the wafer to monitor the temperature of the sample, which was controlled within the range of 10 to 300 K using a Lakeshore 336 temperature controller.

5.2.1 Irradiation of Olivine Samples

The sample was cooled to 10.0 ± 0.5 K whereupon it was irradiated by singly charged, 5 keV molecular deuterium ions (D_2^+), generated by a SPECS IQE 12/38 ion gun. The use of deuterium is driven by the necessity to distinguish between products formed as a result of the irradiation like D₂-water (D_2O) in contrast to residual gases in particular traces of water (H_2O), which are present in any vacuum chamber even under UHV conditions. Molecular deuterium ions (D_2^+) are generated at fluxes higher than three orders of magnitude compared to D^+ ions in the ion source demonstrating that experiments could not have been carried out successfully with D^+ ion beam currents of a few nA. Sigmund *et al.* [1996] demonstrated that upon impact on the silicate surface, each molecular ion (D_2^+) dissociates resulting in a D atom and D^+ implant each possessing 2.5 keV kinetic energy on average. This energy falls in the range of the kinetic energy of solar wind particles of $1 - 2$ keV amu^{-1} . The penetration profile of the incident ions are simulated using the Stopping Range of Ions in Matter (SRIM) program [Ziegler, Ziegler, and Biersack 2010]. Ion trajectories and ion distributions were modeled using the Stopping and Range of Ions in Matter (SRIM) Monte Carlo program. A density of 3.35 g cm^{-3} was entered for San Carlos olivine ($[Mg_{1.8}Fe_{0.2}]SiO_4$) and the layer was thickness of 300 nm, which is larger than the maximum penetration depth of the implanted ions. Deuterium was selected for the simulated ions with a mass

of 2 amu with a kinetic energy of 2.5 keV. 99,999 trajectories were simulated, and the average penetration depth was calculated to be 39 ± 4 nm. The total fluence of deuterium nuclei from implanted ions (D_2^+) was $(1.17 \pm 0.06) \times 10^{18}$. For an area of 1.1 ± 0.2 cm², this dose is equivalent to 130 ± 10 years of irradiation at the lunar surface on average (Table 5.1), which has generally been shown to be the saturation point for olivine [Blanford et al. 1986].

After irradiation by D_2^+ ions, two sets of experiments were carried out (Table 5.2). In the first set, the sample was heated to 300 K at a rate of 1 K min⁻¹ (TPD). In the second set, the ion implanted sample was exposed to pulsed infrared laser photons from a SYNRAD Firestar v40 5 kHz carbon dioxide (CO₂) laser to simulate micrometeorite impact and heating of the ion implanted olivine. After laser exposure, the sample was warmed up to 300 K at a rate of 1 K min⁻¹, held isothermal for 2 h, and then irradiated by the CO₂ laser for 30 min twice with 30 min intervals. For both sets of experiments, control experiments were also performed by conducting the identical experimental sequence, but without irradiating the olivine with molecular deuterium ions. During the full duration of the experiment, mass spectra of the species released into the gas phase were recorded using a calibrated Balzer QMG 422 electron impact quadrupole mass spectrometer (EI-QMS) operated at an electron impact energy of 100 eV with 0.7 mA emission current. A quantification of the sublimed heavy water molecules during the laser irradiation was conducted via calibrating the mass spectrometer for D₂ molecules ($m/z = 4$) before experiments using the method described in Section 2.5 of this thesis.

Table 5.1 Parameters for irradiation sources

Parameters	D ₂ ⁺ ion gun
Initial energy of the ions (keV)	5
Proton flux (cm ⁻² s ⁻¹)	$(1.25 \pm 0.06) \times 10^{13}$
Irradiated area (cm ²)	1.4 ± 0.2
Irradiation time (min)	780
Total D nuclei (cm ⁻²)	$(1.17 \pm 0.06) \times 10^{18}$
Proton flux on moon (cm ⁻² s ⁻¹) [Blanford, G. et al. 1986]	$(3.0 \pm 0.5) \times 10^8$
Simulated time (year)	130 ± 10
Parameters	CO ₂ -laser
Wavelength of the laser (μm)	10.6
Laser power (W cm ⁻²)	2.4 ± 0.3
Irradiated area (cm ²)	1.0 ± 0.1
Single round irradiation time (min)	30
Total deposited laser energy (J m ⁻²)	$(4.3 \pm 0.4) \times 10^7$
Micrometeorite dose on moon (J m ⁻² year ⁻¹) [Lucey 2006]	10
Simulated time (year)	4.3×10^6

Table 5.2 List of experiments

Sources	Stages and parameters				
1. D ₂ irradiation (Blank)	D ₂ (gas)	TPD	---	----	---
	10 K, 780 min	10 to 300 K, 290 min			
2. D ₂ ⁺ ion irradiation	D ₂ ⁺ ion	TPD	---	---	---
	10 K, 780 min	10 to 300 K, 290 min			
3. D ₂ + laser irradiation (Blank)	D ₂ (gas)	Laser	TPD	Laser	Laser
	10 K, 780 min	10 K, 30 min	10 to 300 K, 290 min	10 K, 30 min	10 K, 30 min
4. D ₂ ⁺ ion + laser irradiation	D ₂ ⁺ ion	Laser	TPD	Laser	Laser
	10 K, 780 min	10 K, 30 min	10 to 300 K, 290 min	10 K, 30 min	10 K, 30 min

5.2.2 Focused Ion Beam – Scanning Electron Microscopy (FIB-SEM)

Following irradiation, the olivine samples were transferred to a conductive mount and carbon-coated for focused ion beam – scanning electron microscopy (FIB-SEM) using an FEI Helios 660 dual beam focused ion beam instrument (FIB) [Bradley et al. 2014]. Surfaces of grains were imaged by secondary electron imaging to identify melted textures, and grains with melt and surface pits were selected for preparation of electron-transparent thin sections. Standard FIB section preparation procedures were followed to create electron-transparent thin section. A protective strap of electron beam-deposited platinum (Pt) followed by ion beam-deposited Pt was first deposited to protect the region of interest during subsequent 30 keV Ga⁺-ion milling steps to remove a cross-section of the olivine sample. The section was removed as an approximately 1 µm thick slab and Pt-welded to a copper half-grid where it was further thinned by ion milling to electron transparency (100 nm thickness). The amorphous damaged kerf generated by 30 keV ion milling was removed by a 5 keV ion cleaning step on each side of the final FIB cross-section. The FIB cross-sections of the irradiated olivine grain were then imaged by 300 keV brightfield and high angle annular dark field (HAADF) transmission electron microscopy in a FEI high-base Titan G2 60-300 monochromated and dual aberration-corrected (scanning) transmission electron microscope or (S)TEM. Valence electron energy loss (VEEL) spectra were collected at 300 keV using an incident electron probe 2 Å in diameter and 100 pA probe current with an intrinsic energy resolution of 0.18 eV. To minimize damage to the specimen we used diffraction-coupled, point-count mode, a slightly under focused probe and short (3 sec) acquisitions. Spectra were acquired from the olivine substrate, multiple locations within the amorphous rim and a brucite (Mg(OH)₂) mineral standard provided courtesy of Falko Langenhorst, Friedrich Schilling Universität, Jena, Germany. Elemental composition measurements using an EDAX Genesis 4000 Si(Li) solid state

energy dispersive X-ray spectrometer with ultrathin window in the Titan (S)TEM do not reveal differences between substrate and rim; however, the experimental error was sufficiently large that small composition changes would be indistinguishable.

5.3 Mass Spectra and VEELS Analysis

In the first set of experiments, the sample was exposed to 5 keV D_2^+ ions at 10 K for 13 hours before TPD. This is a similar experiment to those performed in Chapter 4 at 10 K. Neither during the irradiation phase nor during the TPD period were ion counts of $m/z = 20$ (D_2O^+) detected above background level. In other words, the exposure of olivine did not produce any detectable amounts of D2-water, or chemically bound D1-hydroxyl groups linked to silicon ($-Si-O-D$) along with D2-water are possibly ‘trapped’ within the olivine and could not be released even at 300 K. Therefore, deuterium ion exposure alone is insufficient to generate and release D2-water from the silicate samples. This finding is consistent with previously reported results that proton irradiation of silicates fails to produce water under UHV conditions [Burke et al. 2011b; Schaible and Baragiola 2014]. However, as is evident from observed ion counts at $m/z = 4$ (D_2^+), the TPD phase revealed that olivine can store implanted deuterium, which can be released upon warming up the irradiated grains to 300 K (as in Figure 4.1a). It should be highlighted that control experiments carried out under identical conditions - except the ion irradiation of the minerals - did not detect any ion counts at $m/z = 4$ (D_2^+). Consequently, the molecular deuterium detected in the TPD phase of the irradiated olivine is clearly linked to the ion implantation demonstrating the capability of olivine to store deuterium (Refer to section 4.5).

For the second set of experiments, it was hypothesized that alternative energy sources might assist in the formation and liberation of D2-water molecules and/or D1-hydroxyl radicals

potentially stored in the silicates. This processing might also lead to the formation of D₂-water via condensation of two silicon-bound D₁-hydroxyl groups (–Si–O–D) leading to D₂-water along with an oxygen bridged –Si–O–Si– moiety [Roskosz et al. 2018]. To test this hypothesis, anhydrous olivine samples were again prepared and exposed to a D₂⁺ ion beam under identical conditions as in the first set of experiments but were then irradiated by a pulsed infrared laser after ion irradiation and before the TPD phase. Laser pulses can create intense heating events reaching temperatures higher than 1,400 K, which is well above maximum diurnal temperatures of 400 K but close to temperatures produced by micrometeorite impacts [Sasaki et al. 2001; Wu et al. 2017; Moroz et al. 1996]. After the TPD phase, the sample was exposed to the laser twice more to examine whether water could still be generated via micrometeorite impact at surface temperatures closely approximating lunar daytime temperatures of up to 400 K. Hence, micrometeorite impacts were simulated at both 10 and 300 K, representing the thermal equilibrium temperature extremes allowed by our instrument and symbolizing extreme temperatures in lunar permanently shadowed regions (10–20 K) [Sefton-Nash et al. 2013] and mid-latitude/mid-morning temperatures (400 K) [Williams et al. 2017], respectively. Control experiments (i.e., experiments conducted under equal conditions, but without exposing the silicate to ion implantation) were performed as well to rule out potential contaminations (Table 5.2).

Upon exposure of the deuterium implanted silicates to the carbon dioxide laser at 10 K, an intense ion count signal is generated at $m/z = 20$ (Figure 5.1). Ions at $m/z = 20$ could be detected during the full laser exposure phase and sharply dropped once the laser irradiation terminated thus demonstrating that signal at $m/z = 20$ is strongly laser correlated. Neither in the irradiation nor in the blank experiments, signal could be detected at $m/z = 40$ (Ar⁺) from ionized argon. Therefore, the ion counts at $m/z = 20$ can be assigned to the molecular parents of isotope-substituted water

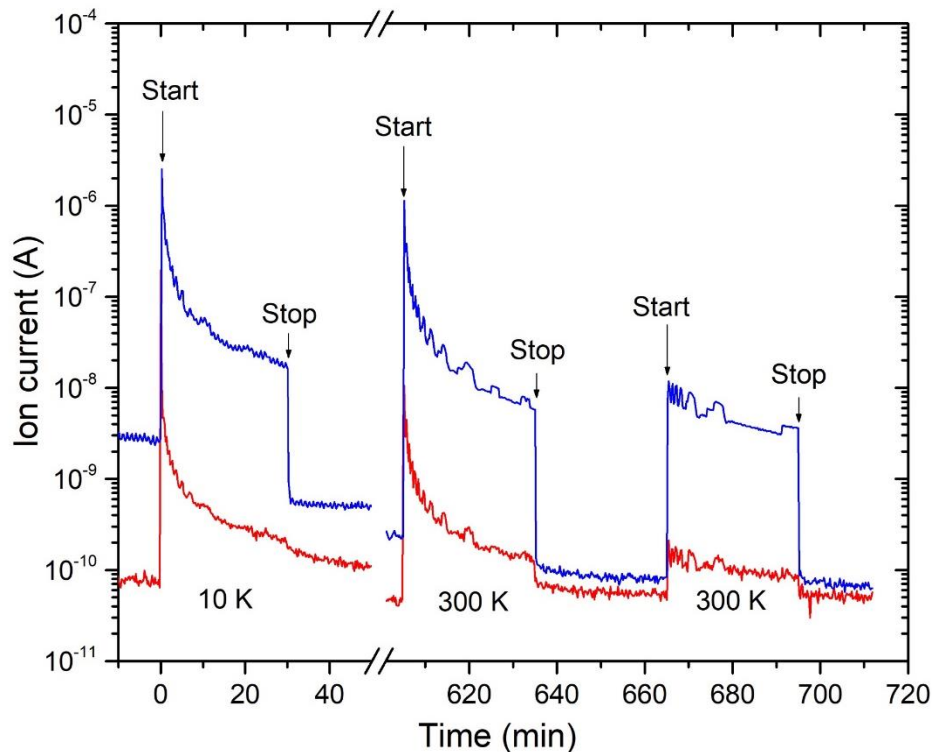


Figure 5.1 Quadrupole mass spectrometry profiles recorded during the simulated micrometeorite impact. Data are shown for mass-to-charge ratio of $m/z = 4$ (D_2^+ , blue) and 20 (D_2O^+ , red) during the laser irradiation of deuterium implanted olivine at 10 K and after the TPD at 300 K. The start and end times of the laser were annotated.

(D_2O^+ and/or $H_2^{18}O^+$), but not to doubly ionized argon ($^{40}Ar^{2+}$). To eliminate contaminating, naturally occurring ^{18}O -water as the source of the signal at $m/z = 20$, we calculated the ratio of the ion count signals recorded at $m/z = 20$ and 18 (Figure 5.2). In the laser irradiation phase, the $m/z = 20$ to $m/z = 18$ ratio of up to 2 is considerably higher by up to three orders of magnitude than the natural abundance of $H_2^{18}O$ and D_2O in normal water (0.002). This confirms that the observed signal at $m/z = 20$ originates from the laser-induced production and sublimation of newly formed D_2 -water. For the duration of the subsequent TPD phase to 300 K, no ions above background level could be detected at $m/z = 20$. Once the sample reached 300 K, the minerals were subjected to a laser irradiation, simulated micrometeorite impact once again to see if the olivine still stores

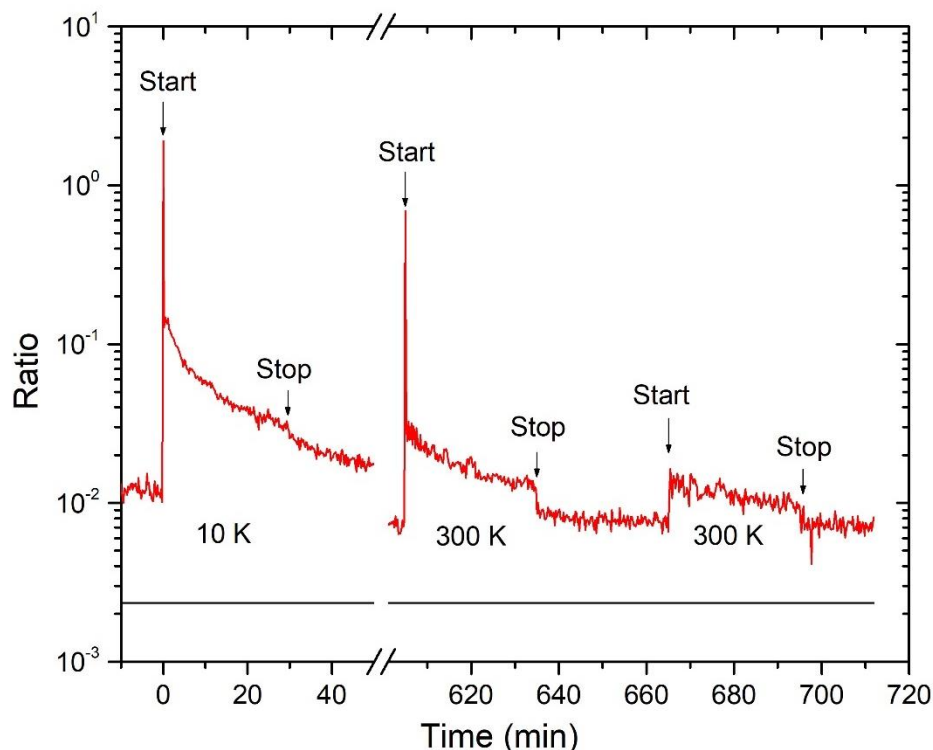


Figure 5.2 Ratio of ion counts recorded at mass-to-charge $m/z = 20$ to $m/z = 18$ (red) during the simulated micrometeorite impact after ion implantation (10 K) and TPD phase (300 K). The total natural abundance of H_2^{18}O (0.2 %) and D_2O (0.02 %) in H_2O (blue) is plotted for comparison. The start and end times of the laser were annotated.

(precursors to) D2-water. As evident from Figures 5.1 and 5.2, D2-water was identified via its molecular parent ion at $m/z = 20$. This suggests that the olivine grains still store (precursors to) D2-water at 300 K, and that with enhanced micrometeorite impact (laser irradiation time) the minerals get depleted of D2-water to be released into the gas phase. Finally, it is interesting to address that in addition to D2-water as detected via $m/z = 20$, molecular deuterium ($m/z = 4$) was released upon laser irradiation of the ion implanted sample at 10 K and 300 K suggesting that the minerals still have the capability to store (chemically bound) deuterium as a precursor to form D2-water. However, since the D_2^+ ion counts in the laser processed samples are lower by a factor of seven compared to the non-laser processed samples, the deuterium was either released from the

mineral to the gas phase during the laser processing and/or reacted to (precursors of) D₂-water. Considering the blank experiments, neither $m/z = 20$ nor $m/z = 4$ was observable. Therefore, these experiments provide compelling evidence that deuterium implantation into olivine followed by pulsed laser heating as proxies for solar wind ion irradiation of lunar silicates succeeded by thermal excursion via micrometeorite impact represent a plausible pathway to generate and liberate water on the Moon.

Following the ion beam exposure and laser irradiation, olivine grains were carbon- and platinum-coated for focused ion beam – scanning electron microscopy (FIB-SEM) examinations. The primary goal of these examinations is to probe the formation of D₂-water (D₂O) along with potential precursors such as –OD moieties within the olivine. First, we explore via imaging by secondary electron microscopy (SEM) generated by a focused ion beam (FIB) the hypothesis that D₂-water and/or their precursors are first synthesized within the olivine sample and then released upon thermal processing by simulated micrometeorite impact into the gas phase resulting in potholes (pits) generated by the pressure build-up of gaseous D₂-water. Second, the existence of D₂-water and/or D₁-hydroxyl functional groups in the olivine is explored by valence electron energy loss spectroscopy (VEEL). The high resolution images of the olivine reveal melted textures as the result of the thermal shock processing from the laser irradiation (Figure 5.3a) and the existence of numerous surface pits along with caps (lids) covering the pits prior to the pressure-induced obliteration of the vesicles (Figure 5.3b). On a typical area of about 20 μm^2 , eight pits can be visualized (Figure 5.3b). These images also expose a dense, interconnected vesiculation extending through the amorphous rim. Grains with surface pits were selected for the preparation of electron-transparent sliced images (Figure 5.4). These thin cross sections exposed the existence of 45 ± 5 nm deep pits within olivine, which was amorphized by the combined effects of the

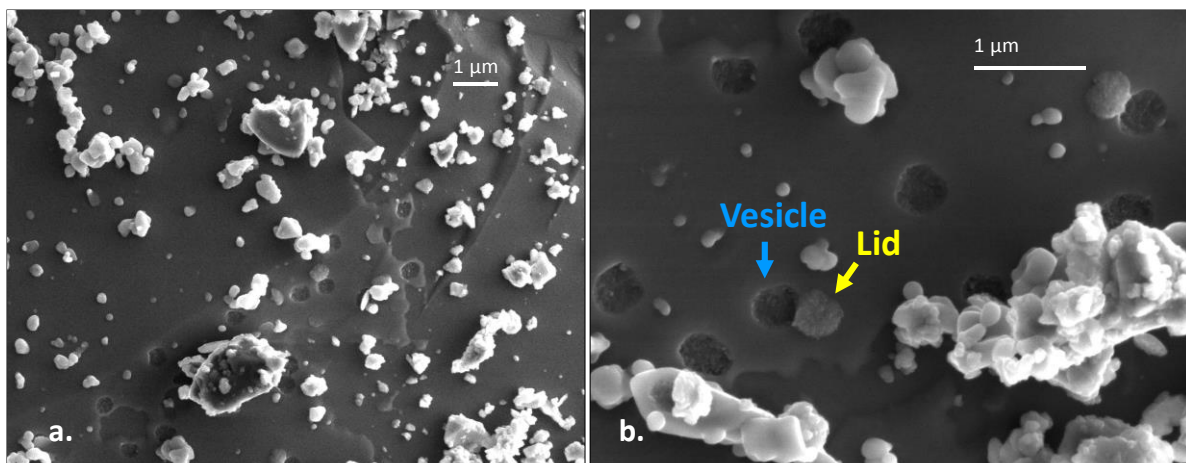


Figure 5.3 Secondary electron images of ion-implanted and laser-processed olivine grains. Low (a) and (b) high resolution images of the olivine disclosing melted textures and the existence of surface pits along with lids covering the pits prior to the pressure-induced obliteration of the vesicles. The orange line indicates the approximate location of the focused ion beam (FIB) thin cross-section extracted from this grain; the blue arrows denote the same particle in each image; selected pits and lids are indicated by red and green arrows, respectively.

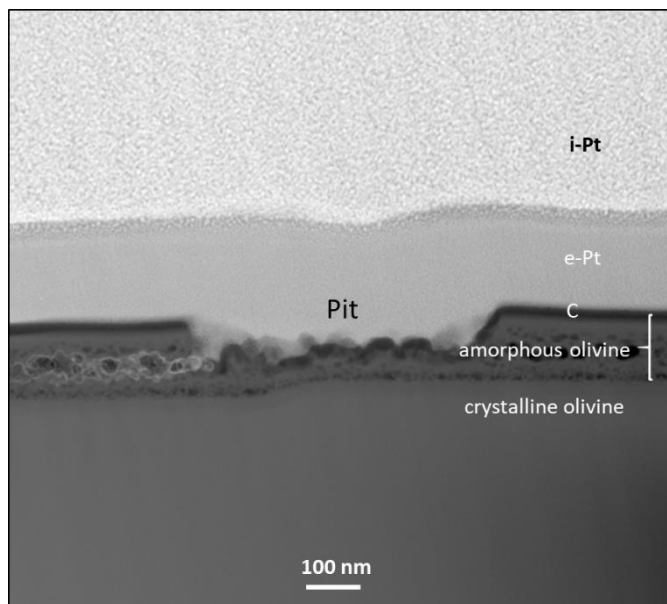


Figure 5.4 Scanning transmission electron microscope (STEM) image of an ion implanted and laser processed olivine sample. The image reveals vesiculation extending through most of an amorphous olivine rim on top of crystalline olivine. Carbon (C), electron-beam-deposited platinum (e-Pt), and ion-beam-deposited platinum (i-Pt) were deposited on the grain as part of the focused ion beam (FIB) preparation. The pit along the top surface of the grain formed when the upper half of the amorphous rim was expelled as vesicles coalesced and overcame the tensile strength of the amorphous rim.

deuterium ion – laser beam exposure over a depth of 125 ± 30 nm. It is important to highlight that this depth matches nicely the maximum penetration depth of implanted 2.5 keV D^+ ions as simulated by the SRIM program of 100 ± 8 nm. Further, the average penetration depth of the 2.5 keV D^+ ions of 39 ± 4 nm as simulated by SRIM correlates nicely with the typical depths of the pits of 45 ± 5 nm. These data provide a solid justification that implanted 5 keV D_2^+ ions split into D^+/D upon impact of the surface each carrying 2.5 keV kinetic energy on average. Finally, VEEL spectra were acquired from the olivine substrate at multiple locations within the amorphous rim. Upon penetrating a sample, the inelastic scattering of the electrons leads to an energy loss via, e.g., phonon excitation, inter- and intra-band transitions, and plasmon excitations. In case of the olivine (Figure 5.5), an absorption band can be clearly seen at 8.6 eV in the low energy loss region. A comparison with VEEL spectra of reference samples of brucite ($Mg(OH)_2$) and water (H_2O) [Grand, Bernas, and Amouyal 1979] provides conclusive proof that the 8.6 eV feature can be linked to D1-hydroxyl ($-OH$) groups and/or D2-water (D_2O). The data of the reference samples reveal that it is not feasible to discriminate between D1-hydroxyl and D2-water since both exhibit an absorption at 8.6 eV resulting from valence electron loss; the presence or absence of the broad absorption peak from the hydrogen K-edge feature from 11.5 to 15.5 eV in water critically depends on the preparation history of the sample as well as the confinement of the water and hence cannot be used for a positive identification of water [Bradley et al. 2014]. The VEEL spectra for water/D2-water and hydroxy/D1-hydroxyl are similar in the range of 6.0 eV to 9.7 eV [Leapman and Sun 1995]; likewise, the VEEL data of chemically bound hydroxyl groups to, e.g., silicon in the olivine and hydroxyl ions as in brucite are indistinguishable in this range of the spectrum [Crozier, Aoki, and Liu 2016]. Nevertheless, the VEEL studies demonstrate unambiguously that even at 300 K, the processed olivine samples still contain possibly D1-hydroxyl ions, but most likely D1-hydroxyl

groups and/or D₂-water even after simulated micrometeorite impacts reaching sample temperatures as high as 1,400 K.

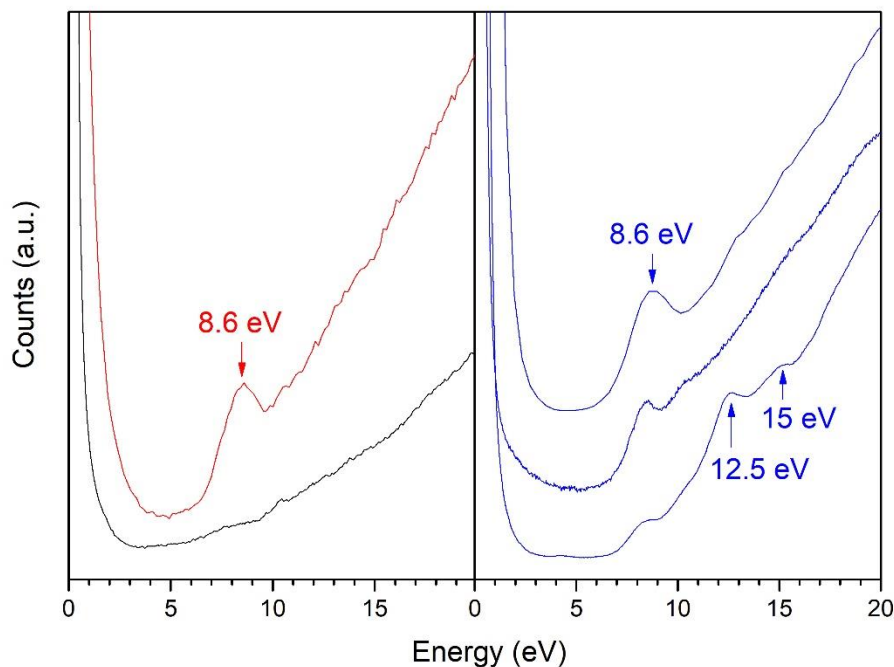


Figure 5.5 Valence electron energy loss (VEEL) spectra of the surface of an ion implanted and laser processed olivine sample. Black: unprocessed olivine substrate; red: ion implanted and laser processed olivine sample; blue: reference samples of brucite (top) and water (middle and bottom).

5.4 The Role of Micrometeorite Impacts

The laboratory simulation experiments along with imaging analysis present compelling evidence on the formation and liberation of D₂-water (D₂O) from deuterium ion implanted anhydrous olivine ([Mg,Fe]₂SiO₄) upon thermal excursion events effectively mimicking the interaction of solar wind proton implantation into lunar silicates superseded by micrometeorite impacts. These studies unveil the potential of lunar silicates to efficiently store (precursors to) water from solar wind proton implantation and the critical role of thermal shock exposure in form

of micrometeorite impacts to release water into the gas phase as evidenced by a combined mass spectrometric (QMS) and valence electron energy loss spectroscopy (VEEL) analysis. Although overall yields of the conversion of implanted deuterium to D₂-water released in the gas phase are less than 1 %, VEEL data revealed that a fraction of the D₂-water and/or their D₁-hydroxyl precursors still survives within the silicates at temperatures of up to 1,400 K upon simulated micrometeorite impact thus providing only lower limits of the conversion yields (Table 5.3). These processes involve the initial synthesis of D₂-water and/or their D₁-hydroxyl precursors during the ion implantation phase followed by the release of D₂-water from vesicles in the amorphous rim of the mineral upon simulated micrometeorite impact into the gas phase resulting in pits created by the pressure build-up of gaseous D₂-water. These investigations also substantiate the exploitation of olivine as a proxy for lunar silicates [Managadze et al. 2011; Sasaki et al. 2001; Schaible and Baragiola 2014], since vesicular rims were also observed within rims on lunar grains and proposed to be generated by synergistic effects of solar-wind and pulse-heating event [Keller and Mckay 1997]. Similar to the lunar vesicular rims, the rims formed in our studies do not contain inclusions of submicroscopic or nanophase phase iron.

Table 5.3 Number of released deuterium and D₂-water molecules during the laser exposure of ion implanted olivine samples.

Species	Laser irradiation 1	Laser irradiation 2	Laser irradiation 3	Total
D ₂	$(8.48 \pm 0.85) \times 10^{14}$	$(3.60 \pm 0.40) \times 10^{14}$	$(0.46 \pm 0.05) \times 10^{14}$	$(1.25 \pm 0.09) \times 10^{15}$
D ₂ O	$(1.04 \pm 0.82) \times 10^{12}$	$(2.27 \pm 0.28) \times 10^{12}$	$(2.3 \pm 0.3) \times 10^{11}$	$(1.3 \pm 0.1) \times 10^{13}$

Having established the formation and release of D2-water, we now discuss the possible formation mechanisms. As stated, upon interaction with the surface of the sample, 5 keV D₂⁺ ion undergoes bond cleavage yielding D atom and a D⁺ ion possessing 2.5 keV of kinetic energy on average. The D⁺ ion is neutralized by exchanging charge with the sample [Hodges 2011]. As implanted into the olivine, each deuterium loses energy via inelastic and elastic energy transfer processes [Weber et al. 2015] as determined by SRIM to be 85 % and 15 %, respectively. The inelastic energy losses may lead to, for instance, silicon-oxygen (Si–O) bond cleavage by coupling the kinetic energy of the implant into the vibrational modes of beyond the dissociation limit of the Si–O bond [Hühn et al. 2017]; elastic collisions generate collision cascades entraining the atomic constituents of the olivine. SRIM simulations reveal that each deuterium implant generates 5 ± 1 oxygen recoil atoms (Figure 5.6). This leads to an overall production of $(5.0 \pm 1.0) \times 10^{18}$ oxygen atoms during the ion irradiation phase, of which a fraction of $(2.6 \pm 0.3) \times 10^{-4}$ are accounted for by the detected D2-water molecules in the gas phase (Table 5.3). The remaining oxygen atoms remain in the silicates as oxides of magnesium and iron and/or react with the silicon to silicon oxides or ‘recycle’ silicate. At the end of their trajectories, the deuterium atoms come to rest and may react with free oxygen atoms previously released in the collision cascade to D1-hydroxyl radicals followed by successive reaction with a second deuterium atom to D2-water (Figure 5.7); alternatively, deuterium may react with the silicates to form deuterated silanol groups (Si–O–D) [Farrell, Hurley, and Zimmerman 2015b]. It is important to note that any (precursor to) D2-water generated in these processes remain trapped in the silicates since no D2-water was detected in the irradiation or TPD phase prior to the simulated micrometeorite impact. The laser exposure of the ion irradiated olivine locally heats the sample and can cause a recombination of free deuterium and oxygen atoms, helps to overcome the activation energy critical for D2-water to diffuse outside

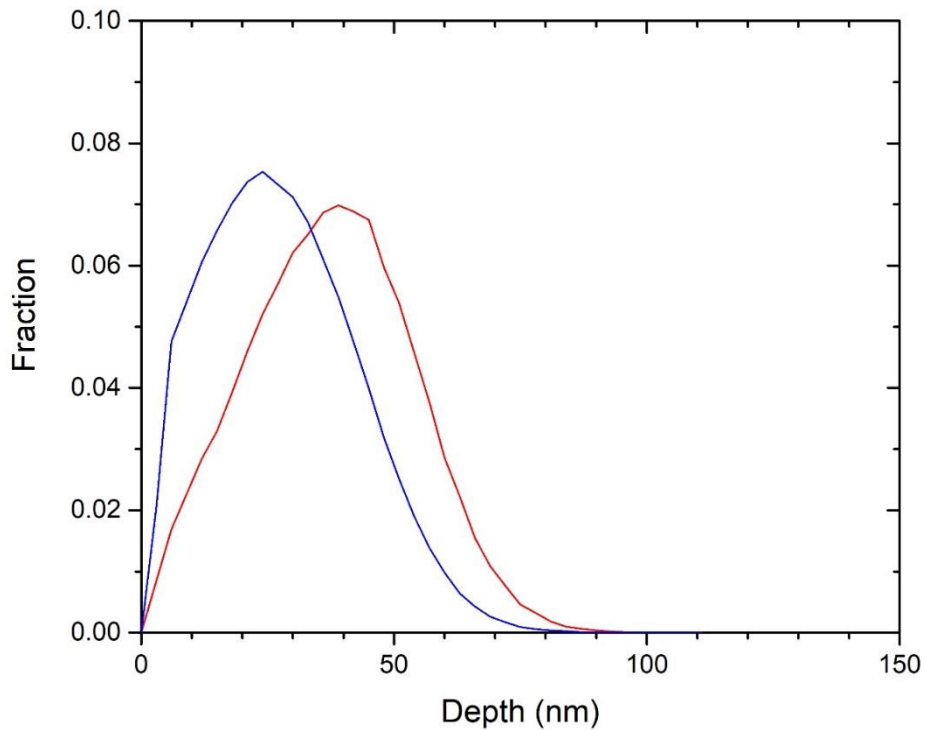


Figure 5.6 Calculated implantation profiles from SRIM of 2.5 keV D^+ ions into olivine (red) overlaid by the recoil distribution of the oxygen recoil atoms (blue). The range of the amorphized olivine as determined via imaging of 125 ± 30 nm agrees nicely with the maximum penetration depth of implanted 2.5 keV D^+ ions simulated by SRIM of 100 ± 8 nm. Also, the average penetration depth of the 2.5 keV D^+ ions of 39 ± 4 nm as simulated by SRIM matches well with the existence of 45 ± 5 nm deep pits within olivine.

the mineral, and/or may trigger the reaction of two Si–O–D groups if they are in close proximity (recombinative desorption) [Orlando et al. 2018]. The recombinative desorption of water from chemically bonded –OH in silicates requires temperatures of at least 450 K, which is well above the maximum temperature of 300 K in our experiments prior to the laser heating and higher than equilibrium surface temperatures of 400 K on the lunar surface at the subsolar point. On the Moon, micrometeorite impacts generate peak temperatures of over 1,000 K [Love and Brownlee 1991] as simulated in our study via laser exposure of the ion implanted olivine samples reaching

temperatures of up to 1,400 K. This temperature is enough to initiate the recombinative desorption (Figure 5.7). Through these processes, D₂-water vapor forms in the rim and can collect to produce the vesicles (Figures 5.3 and 5.4). This explanation is consistent with the prior detection of water in rims on solar wind-exposed interplanetary dust that experienced pulse-heating during atmospheric entry [Bradley et al. 2014] and how vesiculated rims are inferred to form on lunar grains [Keller and McKay 1997]. The complex layering observed in our experiments, with large vesicles sandwiched between layers of finer vesicles could be the result of the distribution of the terminal penetration depth of the implanted deuterium, which is consistent with SRIM simulations (Figure 5.6). Experimental vesicle layers may not be typical of extraterrestrial grains since grain surfaces in lunar regolith are not flat and oriented orthogonal to both the solar wind and extreme heating events. When pressure inside a vesicle is greater than the tensile strength of the amorphous rim, water is released and detected by the mass spectrometer, resulting in round pits on the grain surface (Figures 5.3 and 5.4). The typical depth of the pits corresponds to the depth of the bottom surface of the largest vesicles that string across the midsection of the amorphous rim, which supports pit formation as the result of vesicle coalescence and bursting through the surface. Note that the molecular deuterium released upon laser irradiation of the ion irradiated sample may be a source of the observed molecular hydrogen in the lunar exosphere [Stern et al. 2013; Gladstone et al. 2010]. Stochastic heat-generating events, like micrometeorite impacts, in solar wind-saturated regolith may release molecular hydrogen in the same manner.

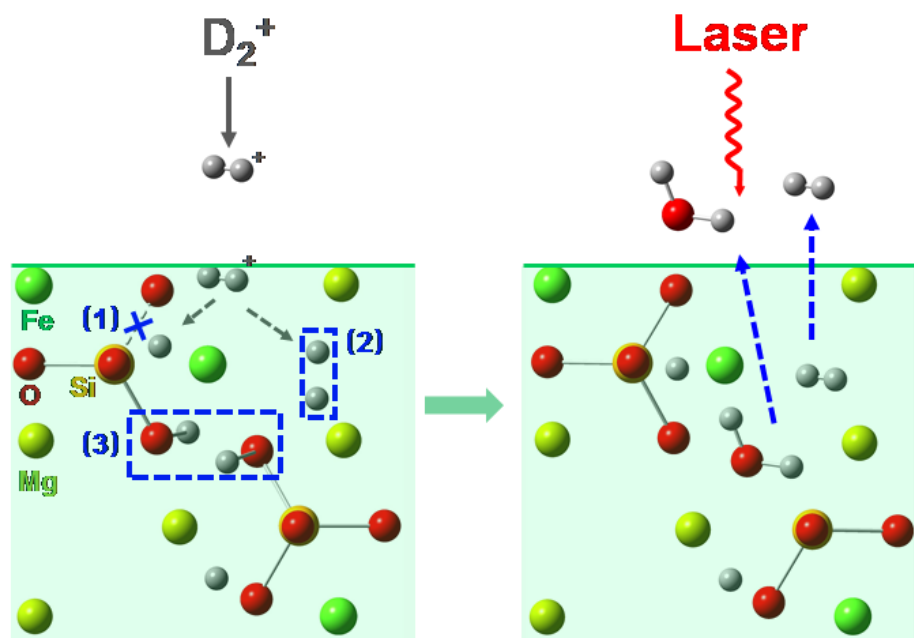


Figure 5.7 Schematic view of olivine ((Mg, Fe) $_2$ SiO $_4$) irradiated by deuterium ions (left) and subsequently irradiated by CO $_2$ -laser (right)

5.5 Conclusion

The present study provides persuasive experimental and analytical evidence on the formation and liberation of (precursors to) D $_2$ -water from 10 K to 300 K in anhydrous olivine upon deuterium ion implantation succeeded by thermal shock heating up to 1,400 K effectively simulating the synergistic effects of solar proton implantation into lunar silicates followed by micrometeorite impact. These investigations represent the first step toward a systematic understanding on the formation and release of (precursors to) lunar water in silicates. Indeed, the Neutral Mass Spectrometer (NMS) on board the Lunar Atmosphere and Dust Environment Explorer (LADEE) spacecraft has detected sporadic water signal in the exosphere of the Moon [Dana M. Hurley and Benna 2017; Benna et al. 2015; Dana M. Hurley et al. 2018] with occurrence rate coinciding with periods of major annual meteoroid events [Jenniskens 1994]. As for every simulation study, no single laboratory experiment can mimic the chemical and physical complexity

of the lunar environment simultaneously. Future experiments are needed to explore the question of whether a particular lithology (texture, grain size, chemical composition) within the lunar soil has a significant effect on the water synthesis and how the water production yields depend on the initial temperature of the lunar soil and the maximum temperature during micro meteorite impact. Likewise, ions such as helium (He^{2+}) and heavier ions, although holding fluxes at least one order of magnitude lower than solar wind protons, can pre-damage the silicates and induce collision cascades with oxygen recoil atoms thus presenting a facile mechanism of generating oxygen atoms [Dukes, Baragiola, and McFadden 1999], which may then react with hydrogen to form water. Despite these open questions, our proof-of-concept study of a symbiotic solar wind – micrometeorite induced formation of water in lunar silicates provides a critical benchmark toward a better understanding of the water production on the Moon as well as on airless bodies in our Solar System such as Mercury and asteroids like 433 Eros [Rivkin et al. 2018] and 24 Themis [Campins et al. 2010; Rivkin and Emery 2010; Küppers et al. 2014].

5.6 References

- Bandfield, Joshua L., Michael J. Poston, Rachel L. Klima, and Christopher S. Edwards. 2018. “Widespread Distribution of OH/H₂O on the Lunar Surface Inferred from Spectral Data.” *Nature Geoscience*. doi:10.1038/s41561-018-0065-0.
- Benna, Mehdi, Dana M. Hurley, T J Stubbs, Paul R Mahaffy, and R. C. Elphic. 2015. “Observations of Meteoroidal Water in the Lunar Exosphere by the LADEE NMS Instrument.” In *Annual Meeting of the Lunar Exploration Analysis Group*, 2059.
- Bennett, Chris J., C. Jamieson, Alexander M. Mebel, and Ralf I. Kaiser. 2004. “Untangling the Formation of the Cyclic Carbon Trioxide Isomer in Low Temperature Carbon Dioxide Ices.” *Physical Chemistry Chemical Physics*. doi:10.1039/b315626p.
- Berezhnoi, A. A., and B. A. Klumov. 1998. “Lunar Ice: Can Its Origin Be Determined?” *Journal of Experimental and Theoretical Physics Letters*. doi:10.1134/1.567840.
- Blanford, G., Børgesen, P., Maurette, M., Möller, W. & Monart, B. 1986. “‘On-line’ Analyses of Simulated Solar Wind Implantations of Terrestrial Analogs of Lunar Materials.” *J. Geophys. Res.-Sol. Ea.* 91: 467–72.
- Bradley, John P, Hope A Ishii, Jeffrey J Gillis-Davis, James Ciston, Michael H Nielsen, Hans A Bechtel, and Michael C Martin. 2014. “Detection of Solar Wind-Produced Water in Irradiated Rims on Silicate Minerals.” *Proceedings of the National Academy of Sciences of the United States of America* 111 (5): 1732–35. doi:10.1073/pnas.1320115111.
- Burke, D. J., C. A. Dukes, J. H. Kim, J. Shi, M. Famá, and R. A. Baragiola. 2011. “Solar Wind

- Contribution to Surficial Lunar Water: Laboratory Investigations.” *Icarus* 211 (2): 1082–88.
doi:10.1016/j.icarus.2010.11.007.
- Campins, Humberto, Kelsey Hargrove, Noemi Pinilla-Alonso, Ellen S. Howell, Michael S. Kelley, Javier Licandro, T. Mothé-Diniz, Y. Fernández, and Julie Ziffer. 2010. “Water Ice and Organics on the Surface of the Asteroid 24 Themis.” *Nature*. doi:10.1038/nature09029.
- Clark, Roger N. 2009. “Detection of Adsorbed Water and Hydroxyl on the Moon.” *Science* (New York, N.Y.) 326 (5952): 562–64. doi:10.1126/science.1178105.
- Colaprete, Anthony, Peter Schultz, Jennifer Heldmann, Diane Wooden, Mark Shirley, Kimberly Ennico, Brendan Hermalyn, et al. 2010. “Detection of Water in the LCROSS Ejecta Plume.” *Science* (New York, N.Y.) 330 (6003): 463–68. doi:10.1126/science.1186986.
- Crozier, Peter A., Toshihiro Aoki, and Qianlang Liu. 2016. “Detection of Water and Its Derivatives on Individual Nanoparticles Using Vibrational Electron Energy-Loss Spectroscopy.” *Ultramicroscopy*. doi:10.1016/j.ultramic.2016.06.008.
- Dukes, C. a., R. a. Baragiola, and L. a. McFadden. 1999. “Surface Modification of Olivine by H^+ and He^+ Bombardment.” *Engineering* 104 (E1): 1865–72. doi:10.1029/98JE02820.
- Farrell, W. M., D. M. Hurley, and M. I. Zimmerman. 2015. “Solar Wind Implantation into Lunar Regolith: Hydrogen Retention in a Surface with Defects.” *Icarus*. doi:10.1016/j.icarus.2014.09.014.
- Feldman, W. C., S. Maurice, A. B. Binder, B. L. Barraclough, R. C. Elphic, and D. J. Lawrence. 1998. “Fluxes of Fast and Epithermal Neutrons from Lunar Prospector: Evidence for Water Ice at the Lunar Poles.” *Science*. doi:10.1126/science.281.5382.1496.

- Gladstone, G. Randall, Dana M. Hurley, Kurt D. Retherford, Paul D. Feldman, Wayne R. Pryor, Jean Yves Chaufray, Maarten Versteeg, et al. 2010. “LRO-LAMP Observations of the LCROSS Impact Plume.” *Science*. doi:10.1126/science.1186474.
- Grand, D., A. Bernas, and E. Amouyal. 1979. “Photoionization of Aqueous Indole: Conduction Band Edge and Energy Gap in Liquid Water.” *Chemical Physics*. doi:10.1016/0301-0104(79)80064-6.
- Hodges, R. R. 2011. “Resolution of the Lunar Hydrogen Enigma.” *Geophysical Research Letters*. doi:10.1029/2011GL046688.
- Honniball, CI, Paul G. Lucey, HM Kaluna, S Li, and L Sun. 2018. “Lunar Surface Water: Latitude, Longitude Systematics, and Detection and Abundances at Small Geologic Targets from Groundbased Telescopic Observations.” In 49th Lunar and Planetary Science Conference, 1726. Lunar and Planetary Institute.
- Hühn, Carolin, Andreas Erlebach, Dorothea Mey, Lothar Wondraczek, and Marek Sierka. 2017. “Ab Initio Energetics of Si–O Bond Cleavage.” *Journal of Computational Chemistry*. doi:10.1002/jcc.24892.
- Hurley, Dana M., and Mehdi Benna. 2017. “Simulations of Lunar Exospheric Water Events from Meteoroid Impacts.” *Planetary and Space Science*. doi:10.1016/j.pss.2017.07.008.
- Hurley, Dana M., Mehdi Benna, T J Stubbs, Paul R Mahaffy, and Richard C Elphic. 2018. “LADEE NMS Observations of Exospheric Water Events at the Moon.” In Lunar and Planetary Science Conference, 2052.
- Ichimura, A. S., A. P. Zent, R. C. Quinn, M. R. Sanchez, and L. A. Taylor. 2012. “Hydroxyl (OH) Production on Airless Planetary Bodies: Evidence from H^+/D^+ ion-Beam Experiments.” *Earth*

- and Planetary Science Letters. doi:10.1016/j.epsl.2012.06.027.
- Jenniskens, Peter. 1994. "Meteor Stream Activity I. The Annual Streams." *Astron. Astrophys.* 287. doi:10.4278/ajhp.110624-QUAL-265.
- Keller, Lindsay P, and David S Mckay. 1997. "The Nature and Origin of Rims on Lunar Soil Grains." *Geochimica et Cosmochimica Acta* 61 (I): 2311–41. doi:10.1016/S0016-7037(97)00085-9.
- Küppers, Michael, Laurence O'Rourke, Dominique Bockelée-Morvan, Vladimir Zakharov, Seungwon Lee, Paul Von Allmen, Benoît Carry, et al. 2014. "Localized Sources of Water Vapour on the Dwarf Planet (1) Ceres." *Nature*. doi:10.1038/nature12918.
- Leapman, Richard D., and Songquan Sun. 1995. "Cryo-Electron Energy Loss Spectroscopy: Observations on Vitrified Hydrated Specimens and Radiation Damage." *Ultramicroscopy*. doi:10.1016/0304-3991(95)00019-W.
- Li, Shuai, Paul G. Lucey, Ralph E. Milliken, Paul O. Hayne, Elizabeth Fisher, Jean-Pierre Williams, Dana M. Hurley, and Richard C. Elphic. 2018. "Direct Evidence of Surface Exposed Water Ice in the Lunar Polar Regions." *Proceedings of the National Academy of Sciences*. doi:10.1073/pnas.1802345115.
- Li, Shuai, and Ralph E. Milliken. 2017. "Water on the Surface of the Moon as Seen by the Moon Mineralogy Mapper: Distribution, Abundance, and Origins." *Science Advances*. doi:10.1126/sciadv.1701471.
- Love, S. G., and D. E. Brownlee. 1991. "Heating and Thermal Transformation of Micrometeoroids Entering the Earth's Atmosphere." *Icarus*. doi:10.1016/0019-1035(91)90085-8.

- Lucey, P. 2006. "Understanding the Lunar Surface and Space-Moon Interactions." *Reviews in Mineralogy and Geochemistry*. doi:10.2138/rmg.2006.60.2.
- Managadze, G.G., V.T. Cherepin, Y.G. Shkuratov, V.N. Kolesnik, and a.E. Chumikov. 2011. "Simulating OH/H₂O Formation by Solar Wind at the Lunar Surface." *Icarus* 215 (1): 449–51. doi:10.1016/j.icarus.2011.06.025.
- Milliken, Ralph E., and Shuai Li. 2017. "Remote Detection of Widespread Indigenous Water in Lunar Pyroclastic Deposits." *Nature Geoscience*. doi:10.1038/NGEO2993.
- Moroz, L. V., A. V. Fisenko, L. F. Semjonova, C. M. Pieters, and N. N. Korotaeva. 1996. "Optical Effects of Regolith Processes on S-Asteroids as Simulated by Laser Shots on Ordinary Chondrite and Other Mafic Materials." *Icarus*. doi:10.1006/icar.1996.0130.
- Needham, Debra H., and David A. Kring. 2017. "Lunar Volcanism Produced a Transient Atmosphere around the Ancient Moon." *Earth and Planetary Science Letters*. doi:10.1016/j.epsl.2017.09.002.
- Nozette, S., C. L. Lichtenberg, P. Spudis, R. Bonner, W. Ort, E. Malaret, M. Robinson, and E. M. Shoemaker. 1996. "The Clementine Bistatic Radar Experiment." *Science*. doi:10.1126/science.274.5292.1495.
- Ong, Lissa, Erik I. Asphaug, Donald Korycansky, and Robert F. Coker. 2010. "Volatile Retention from Cometary Impacts on the Moon." *Icarus*. doi:10.1016/j.icarus.2009.12.012.
- Orlando, Thomas M, Brant Jones, Carol Paty, Micah J Schaible, John R Reynolds, Phillip N First, Stephen K Robinson, Valeria La Saponara, and Esther Beltran. 2018. "Catalyst: Radiation Effects on Volatiles and Exploration of Asteroids and the Lunar Surface." *Chem* 4 (1). Elsevier: 8–12. doi:10.1016/j.chempr.2017.12.004.

- P. Greenwood, J. S. Itoh, N. Sakamoto, Larry Taylor, P. H. Warren, and Hisayoshi Yurimoto. 2010. Water in Apollo Rock Samples and the D/H of Lunar Apatite. Vol. 41.
- Pieters, C. M., J. N. Goswami, R. N. Clark, M. Annadurai, J. Boardman, B. Buratti, J.-P. P. Combe, et al. 2009. "Character and Spatial Distribution of OH/H₂O on the Surface of the Moon Seen by M3 on Chandrayaan-1." *Science* 326 (5952): 568–72. doi:10.1126/science.1178658.
- Rivkin, Andrew S., and Joshua P. Emery. 2010. "Detection of Ice and Organics on an Asteroidal Surface." *Nature*. doi:10.1038/nature09028.
- Rivkin, Andrew S., Ellen S. Howell, Joshua P. Emery, and Jessica Sunshine. 2018. "Evidence for OH or H₂O on the Surface of 433 Eros and 1036 Ganymed." *Icarus*. doi:10.1016/j.icarus.2017.04.006.
- Roskosz, M., E. Deloule, J. Ingrin, C. Depecker, D. Laporte, S. Merkel, L. Remusat, and H. Leroux. 2018. "Kinetic D/H Fractionation during Hydration and Dehydration of Silicate Glasses, Melts and Nominally Anhydrous Minerals." *Geochimica et Cosmochimica Acta*. doi:10.1016/j.gca.2018.04.027.
- Saal, Alberto E., Erik H. Hauri, Mauro Lo Cascio, James A. Van Orman, Malcolm C. Rutherford, and Reid F. Cooper. 2008. "Volatile Content of Lunar Volcanic Glasses and the Presence of Water in the Moon's Interior." *Nature*. doi:10.1038/nature07047.
- Sasaki, Sho, Keiko Nakamura, Yoshimi Hamabe, Erika Kurahashi, and Takahiro Hiroi. 2001. "Production of Iron Nanoparticles by Laser Irradiation in a Simulation of Lunar-like Space Weathering." *Nature*. doi:10.1038/35069013.
- Schaible, Micah J., and Raúl A. Baragiola. 2014. "Hydrogen Implantation in Silicates: The Role of Solar Wind in SiOH Bond Formation on the Surfaces of Airless Bodies in Space." *Journal*

- of Geophysical Research: Planets 119: 2017–28. doi:10.1002/ 2014JE004650.
- Sefton-Nash, Elliot, Matthew A. Siegler, and David A. Paige. 2013. “Thermal Extremes in Permanently Shadowed Regions at the Lunar South Pole.” In Proceedings of the 44th Lunar and Planetary Science Conference, 2617.
- Sigmund, P., I.S. Bitensky, and J. Jensen. 1996. “Molecule and Cluster Bombardment: Energy Loss, Trajectories, and Collision Cascades.” Nuclear Instruments and Methods in Physics Research Section B: Beam Interactions with Materials and Atoms 112 (1–4): 1–11. doi:10.1016/0168-583X(95)01125-0.
- Stacy, N. J S, D. B. Campbell, and P. G. Ford. 1997. “Arecibo Radar Mapping of the Lunar Poles: A Search for Ice Deposits.” Science. doi:10.1126/science.276.5318.1527.
- Stern, S. Alan, Jason C. Cook, Jean Yves Chaufray, Paul D. Feldman, G. Randall Gladstone, and Kurt D. Retherford. 2013. “Lunar Atmospheric H₂ Detections by the LAMP UV Spectrograph on the Lunar Reconnaissance Orbiter.” Icarus. doi:10.1016/j.icarus.2013.07.011.
- Stewart, Bénédicte D., Elisabetta Pierazzo, David B. Goldstein, Philip L. Varghese, and Laurence M. Trafton. 2011. “Simulations of a Comet Impact on the Moon and Associated Ice Deposition in Polar Cold Traps.” Icarus. doi:10.1016/j.icarus.2011.03.014.
- Sunshine, Jessica M., Tony L. Farnham, Lori M. Feaga, Olivier Groussin, Frédéric Merlin, Ralph E. Milliken, and Michael F. A’Hearn. 2009. “Temporal and Spatial Variability of Lunar Hydration as Observed by the Deep Impact Spacecraft.” Science 326 (5952): 565–68. doi:10.1126/science.1179788.
- Weber, William J., Dorothy M. Duffy, Lionel Thomé, and Yanwen Zhang. 2015. “The Role of Electronic Energy Loss in Ion Beam Modification of Materials.” Current Opinion in Solid

- State and Materials Science. doi:10.1016/j.cossms.2014.09.003.
- Williams, J. P., D. A. Paige, B. T. Greenhagen, and E. Sefton-Nash. 2017. “The Global Surface Temperatures of the Moon as Measured by the Diviner Lunar Radiometer Experiment.” *Icarus*. doi:10.1016/j.icarus.2016.08.012.
- Wu, Yanxue, Xiongyao Li, Wenqing Yao, and Shijie Wang. 2017. “Impact Characteristics of Different Rocks in a Pulsed Laser Irradiation Experiment: Simulation of Micrometeorite Bombardment on the Moon.” *Journal of Geophysical Research: Planets*. doi:10.1002/2016JE005220.
- Yoshida, Tomoko, Tetsuo Tanabe, Masahiro Hirano, and Shunsuke Muto. 2004. “FT-IR Study on the Effect of OH Content on the Damage Process in Silica Glasses Irradiated by Hydrogen.” In *Nuclear Instruments and Methods in Physics Research, Section B: Beam Interactions with Materials and Atoms*. doi:10.1016/j.nimb.2003.12.056.
- Zeller, E. J., L. B. Ronca, and P. W. Levy. 1966. “Proton-Induced Hydroxyl Formation on the Lunar Surface.” *Journal of Geophysical Research*. doi:10.1029/JZ071i020p04855.
- Ziegler, James F., M. D. Ziegler, and J. P. Biersack. 2010. “SRIM - The Stopping and Range of Ions in Matter (2010).” *Nuclear Instruments and Methods in Physics Research, Section B: Beam Interactions with Materials and Atoms* 268 (11–12): 1818–23. doi:10.1016/j.nimb.2010.02.091.

Chapter 6

CONCLUSION

6.1 Summary of Results

Within this thesis, several laboratory experiments have been presented that reveal important new insights to chemical reactions driven by space weathering processes on planetary surfaces. The impact of these results is summarized here.

The objective of Chapter 3 was to investigate the degradation of perchlorates within the terminal track of galactic and solar cosmic rays in the Martian regolith to more fully understand the role these oxidizing agents play in the destruction of organic molecules [ten Kate 2010; Poch et al. 2013]. GCRs provide the most suitable explanation for the weathering of organics beneath the uppermost layer of the Martian surface, despite having an energy flux much lower than the energy flux of solar photons, because UV photons are completely absorbed within the top few monolayers of the regolith dust [Muñoz-Caro, Mateo-Martí, and Martínez-Frías 2006]. This fact has been largely underrepresented in the literature. The results show that not only is molecular oxygen (O_2) produced by the radiolysis of perchlorates with low-energy ions, but also provide proof-of-concept that GCRs can take part in the formation of new products after they have been implanted in the soil. These experiments have detected for the first time the formation of hydrogen peroxide, another known strong oxidizer, in addition to molecular oxygen (O_2) and molecular deuterium (D_2). At extreme energy doses, heavy water (D_2O) was also detected. Thus, it has been found that not only do GCRs play a direct role in the destruction of organic molecules up to 2 m below the surface, but they also breakdown perchlorates into volatile compounds with greater oxidizing power than perchlorates themselves.

Chapter 4 is a study demonstrating the relationship between the solar wind and the lunar exosphere. Olivine samples were irradiated with deuterium ions to the known lunar regolith saturation point at temperatures consistent with permanently shadowed regions at the poles to mid latitude regions during sunrise. Temperature programmed desorption results show that on the Moon, the thermal processing of the regolith as the night cycles to day allows trapped hydrogen atoms to diffuse through the silicate and recombine to form molecular hydrogen (H_2) that contributes to the total concentration of molecular hydrogen in the lunar exosphere. These investigations signify the first step toward a systematic comprehension on the formation and release of molecular hydrogen from lunar silicates and its contribution to the lunar exosphere. It was found that for the coldest irradiation temperature at 10 K, 3.51 ± 0.55 % of the impinging solar wind proxy ions could be converted to D_2 (H_2 on the moon) through a diffusion-barrier reaction. This yield is lower than the estimated efficiency by Hurley et. al [2017] proposing that close to 10% of the incoming solar wind protons would need to be converted to molecular hydrogen (H_2) to account for the observed molecular hydrogen density of $1,200 \text{ cm}^{-3}$ in the lunar exosphere. Further studies are required to observe the kinetic energy distribution of hydrogen as it leaves the sample as this might critically reduce the required yield to a few per cent as observed experimentally in our study.

Finally, the thesis concludes with observing the combined effects of space weathering on the lunar surface by the solar wind and micrometeoroid impacts. Contrary to other reports [Managadze et al. 2011; Bradley et al. 2014; Ichimura et al. 2012], no evidence could be found that water (H_2O) can be generated and liberated from the lunar regolith by solar wind ions alone. Instead, these studies reveal the importance of thermal processing by micrometeorite impacts to induce bond formation with trapped solar wind ions and free oxygen atoms in the amorphous rims

of irradiated grains. While remote sensing missions and ground based observations have confirmed the presence of hydroxyl groups (-OH), via detection of the $2.8\text{ }\mu\text{m}$ band [Pieters et al. 2009; Sunshine et al. 2009; Clark 2009], and surface exposed water ice [Li et al. 2018], the investigations made in this thesis represent the first step toward a systematic understanding on the formation and release of (precursors to) lunar water in silicates. Future experiments are still needed to explore the question of whether lithology (texture, grain size, chemical composition) and temperature of the lunar soil has a significant effect on water. Despite these open questions, our proof-of-concept study of a symbiotic solar wind – micrometeorite induced formation of water in lunar silicates provides a critical benchmark toward a better understanding of the water production on the Moon as well as on airless bodies in our Solar System.

6.2 References

- Bradley, John P, Hope A Ishii, Jeffrey J Gillis-Davis, James Ciston, Michael H Nielsen, Hans A Bechtel, and Michael C Martin. 2014. “Detection of Solar Wind-Produced Water in Irradiated Rims on Silicate Minerals.” *Proceedings of the National Academy of Sciences of the United States of America* 111 (5): 1732–35. doi:10.1073/pnas.1320115111.
- Clark, Roger N. 2009. “Detection of Adsorbed Water and Hydroxyl on the Moon.” *Science* (New York, N.Y.) 326 (5952): 562–64. doi:10.1126/science.1178105.
- Hurley, Dana M., Jason C. Cook, Kurt D. Retherford, Thomas Greathouse, G. Randall Gladstone, Kathleen Mandt, Cesare Grava, et al. 2017. “Contributions of Solar Wind and Micrometeoroids to Molecular Hydrogen in the Lunar Exosphere.” *Icarus* 283: 31–37. doi:10.1016/j.icarus.2016.04.019.
- Ichimura, A. S., A. P. Zent, R. C. Quinn, M. R. Sanchez, and L. A. Taylor. 2012. “Hydroxyl (OH) Production on Airless Planetary Bodies: Evidence from H^+/D^+ ion-Beam Experiments.” *Earth and Planetary Science Letters*. doi:10.1016/j.epsl.2012.06.027.
- Kate, Inge L ten. 2010. “Organics on Mars?” *Astrobiology* 10 (6): 589–603. doi:10.1089/ast.2010.0498.
- Li, Shuai, Paul G. Lucey, Ralph E. Milliken, Paul O. Hayne, Elizabeth Fisher, Jean-Pierre Williams, Dana M. Hurley, and Richard C. Elphic. 2018. “Direct Evidence of Surface Exposed Water Ice in the Lunar Polar Regions.” *Proceedings of the National Academy of Sciences*. doi:10.1073/pnas.1802345115.

- Managadze, G.G., V.T. Cherepin, Y.G. Shkuratov, V.N. Kolesnik, and a.E. Chumikov. 2011. “Simulating OH/H₂O Formation by Solar Wind at the Lunar Surface.” *Icarus* 215 (1): 449–51. doi:10.1016/j.icarus.2011.06.025.
- Muñoz-Caro, G. M., E. Mateo-Martí, and J. Martínez-Frías. 2006. “Near-UV Transmittance of Basalt Dust as an Analog of the Martian Regolith: Implications for Sensor Calibration and Astrobiology.” *Sensors* 6 (6): 688–96. doi:10.3390/s6060688.
- Pieters, C M, J N Goswami, R N Clark, M Annadurai, J Boardman, B Buratti, J-P P. Combe, et al. 2009. “Character and Spatial Distribution of OH/H₂O on the Surface of the Moon Seen by M3 on Chandrayaan-1.” *Science* 326 (5952): 568–72. doi:10.1126/science.1178658.
- Poch, O., A. Noblet, F. Stalport, J. J. Correia, N. Grand, C. Szopa, and P. Coll. 2013. “Chemical Evolution of Organic Molecules under Mars-like UV Radiation Conditions Simulated in the Laboratory with the ‘Mars Organic Molecule Irradiation and Evolution’ (MOMIE) Setup.” *Planetary and Space Science* 85: 188–97. doi:10.1016/j.pss.2013.06.013.
- Sunshine, Jessica M., Tony L. Farnham, Lori M. Feaga, Olivier Groussin, Frédéric Merlin, Ralph E. Milliken, and Michael F. A’Hearn. 2009. “Temporal and Spatial Variability of Lunar Hydration as Observed by the Deep Impact Spacecraft.” *Science* 326 (5952): 565–68. doi:10.1126/science.1179788.

APPENDIX

A.1 Bakeout Procedure

This section describes the necessary steps to properly evacuate the chamber for experiments. Several components of the SSM are designed to operate only under UHV conditions, thus it is imperative that these procedures are strictly observed to avoid severe damage to the instruments:

- After loading the sample or installing the silver mirror and securing the front plate, ensure that all CF connections make a proper seal over the copper gaskets and tighten the bolts in a star pattern.
- Close the leak valves to the MC (to the left of the front plate) and RIV of the ion gun.
- The scroll pumps must be turned on first to bring each region to low 10^{-2} Torr before the turbo pumps can start. To do this, first bypass the interlock system for each gate valve that leads to the scroll pumps for MC, RI, RII, RIII, RIV, as well as the gate valve between RIV/MC. Then open each gate valve. **IMPORTANT:** It is likely that regions between the closed gate valves and the scroll pumps are still under slight vacuum from previous use. Always check to make sure these regions have been vented by carefully disconnecting the KF connections on the inlet of the scroll pumps in the pump room. Use the readout of the diaphragm gauges to check that atmospheric pressure is established before the gate valves are opened! Failure to do so will cause air to violently rush through the turbo pumps and damage them.

- Start the scroll pumps for RI, RII, RIII/IV, and MC. Watch the pressure gauges on the control panel. If a pressure lower than 10^{-1} Torr cannot be attained after a few minutes, there is a leak.
- Once each region has reached a pressure in the low 10^{-2} Torr range, start the turbo pumps for RI, RII, RIII, RIV, MC Main, and MC backing pump. Monitor the RPM values on the turbos as they are speeding up. If they are having difficulty or an error is displayed, there is most likely a leak that must be fixed immediately.
- Turn on the Pfeiffer pumping stations that evacuate the differentially pumped feedthroughs of the MC and the gas mixing chamber (GMC).
- Once the turbos are at full speed, turn on the ion gauges for RI, RII, RIII, RIV and MC. Let the turbos run for several minutes before degassing each ion gauge.
- At this point, check to make sure that the interlock indicator is illuminated on each ion gauge. If this is the case, turn off the bypass switches for each gate valve to activate the interlock system.
- To turn on the QMS and/or ion gun power supply, first push the large, red RESET button on the interlock. Otherwise, power will not be supplied.
- Double check that all wiring connections for the QMS system are properly installed. Then turn on the power supply to the QMS on the instrument control panel.
- Open the SETUP program from the Quadstar software. Select ion source from the control bar at the top. A window opens to turn on the SEM and the ion source. Select both. If the filament to the ion source is turned on, the MC will be illuminated and the pressure will quickly rise to high 10^{-7} Torr range.

- Wait a few minutes for the pressure to come down again before engaging the “degas” mode in the program. This will run for 5 minutes.
- REMOVE THE MAGNET FROM THE WIEN MASS FILTER ON THE ION GUN AND DISCONNECT THE CABLES LEADING TO THE ION SOURCE CHAMBER, THE WIEN FILTER, AND THE ION BEAM FOCUSING LENS. OPEN THE ANGLE VALVE ON THE ION GUN COMPLETELY.
- Secure the heating tapes around each region of the machine and make sure the proper thermocouple is fastened in a way that it will accurately read the temperature. Then generously cover the SSM with aluminum foil.
- Double check that all thermocouples are secure!!!
- Begin the bakeout by turning on the switches for the heating tapes on the SS control panel. Ensure that the thermocouples show an increase in temperature. If not, either the fuse needs to be replaced or the thermocouple is not properly secured. If the thermocouples are not properly secured, this can have serious consequences as the heating tapes will continue to heat up and could cause damage to the machine. (Table A.1)
- Turn on the Lakeshore 336 controller. Set the setpoint to 310 K with the heater on high. The MC pressure will spike to $\sim 10^{-6}$ K. Increase setpoint to 318 K when P(MC) decreases again.
- Check temperature periodically for the first 2 hours. Ensure no overheating at surfaces.

Table A.1 Setpoint temperatures for bakeout of SSM

Zone	Location	Setpoint T (°C)
R1	Region 1 – Ion Source Installed Only	45
R2	Region 2 – Ion Source Installed Only	40
R3	Region 3	40
R4	Region 4	50
XY	Deflection plates	60
LTM	Linear transfer arm (or front plate)	55
CTI	Coldhead top	60
TOP	Main chamber top	70
MID	Main chamber middle	65
LOW	Main chamber bottom	60
MCFC	Main chamber faraday cup	65
GMC	Gas mixing chamber – Sensor Only	-

A.2 Ion Gun Operation

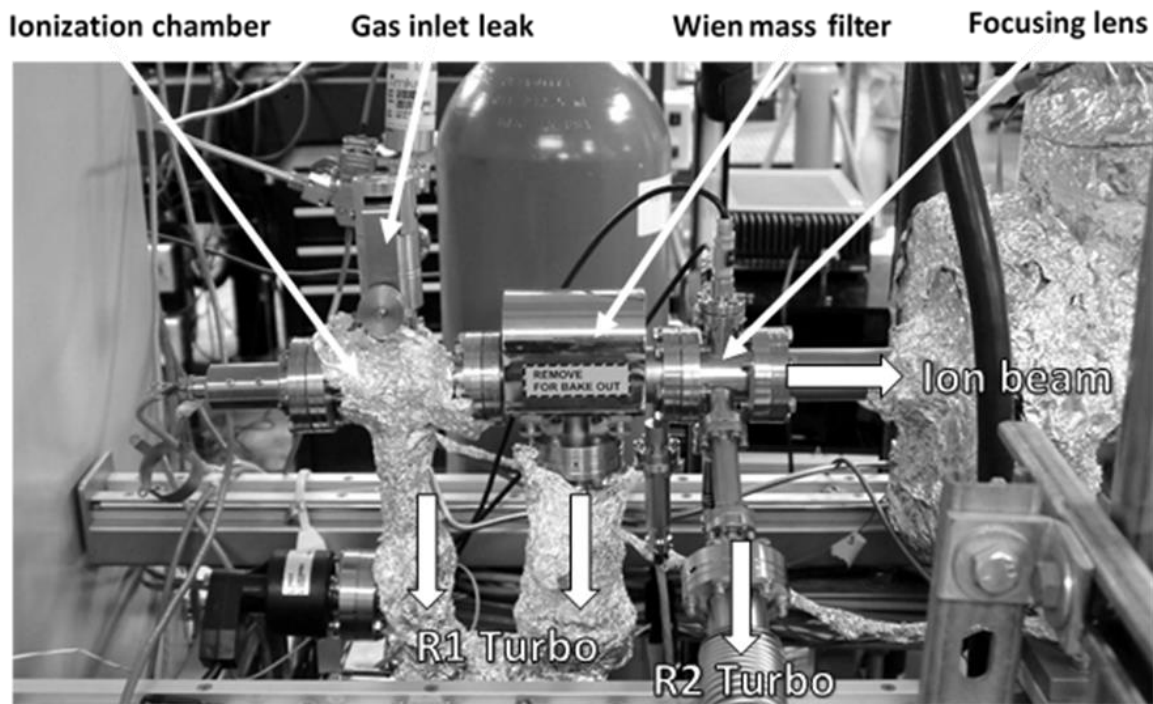


Figure A.1 Picture of the SPECS IQE 12/38 charged particle source.

The working principle and detailed operation instructions are given in the operator's manuals produced by SPECS, GmbH. There are three manuals that cover all aspects of operation: the power supply operation manual (PU-IQE 12/38), the charged particle source manual (Specs IQE 12/38), and Wien mass filter manual. A basic overview of operating the instrument for the experiments in this thesis are provided here and in the following sections.

- After the bakeout procedure, reconnect all cables to the ion source chamber, the Wien mass filter, and the ion beam focusing lens. Also reinstall the magnet to the Wien mass filter, paying special attention to the proper orientation of the magnet as indicated by the arrow marked on the top of the magnet. The cables must be orientated properly. See the operation manuals for positioning the F1 lens cable, F2 lens cable, Wien filter cable, and deflection plate cable.

- If bakeout has been properly executed, the base pressure in RI of the ion gun should be low 10^{-8} Torr at most. Ensure that the angle valve is still open.
- Turn on the power supplies for the ion gun and the Wien mass filter. The PU 12/38 should start up in “OFF” mode. If it is in “STANDBY” mode, hold the “NUM” key while pressing the “OPERATE” key to put it in “OFF” mode. Make sure the “ON” switch is active on the Wien filter
- Go to “SETUP” and cycle through the options by continuing to push “SETUP” until the display reads “L”. Change the value to 94.5 by pushing the “MODIFY” key and rotating the scroll wheel and then hit “MODIFY” again.
- If the filament for the ion source replaced during the last venting, you will need to follow the procedures for first time use as described in the IQE 12/38 operation manual under Sec. 4.2.2
- Put the power supply in “STANDBY” mode by pushing the “OPERATE” key once. The current of the filament will rise to the standby value saved in the setup options. You will also see the pressure rise on the cold cathode gauge.
- Ensure the RIV faraday cup is in place to detect the incoming ions, put the phosphor screen in place to block the beam if the faraday cup is moved, and have RIV/MC gate valve closed.
- Set “EMISSION” to zero before putting the supply in operate mode.
- Set the remaining options to the proper values for operating the source. For the experiments used in this thesis, the following settings were a general starting point and then fine-tuned to maximum current (keep emission at 0.0 for this part):

Table A.2 Example of ion gun parameters used in experiments

Energy (eV)	5000
Extractor (5)	98.34
F1 (%)	83.34
F2 (%)	38.72
Emission (mA)	10.00
PX (mm)	-1.4
PY (mm)	-2.1
Width X & Y	0.0
Mass scale (Wien filter PS)	658
Stigmator	1000
RIV F.C.	580
MC F.C.	2000
Leak current (μ A)	13-14

- Supply feed line with ~ 800 Torr of D_2 gas (capacitance diaphragm gauge – Terranova 908A).
- Keeping the angle valve open, introduce D_2 gas to the ion source following SOPs until the pressure on the cold cathode gauge reads mid 10^{-6} Torr.
- Put the power supply in “OPERATE” mode by pushing the “OPERATE” key a second time. The pressure will rise again.
- The emission current needs to be increased SLOWLY to 10.00 mA for best stability of the filament. This is a crucial step, otherwise the filament can warp and come in contact with the anode cage inside the source chamber. The current values shown on the display readout are a good indicator for the health of the filament. Overtime, the filament will require increasingly

higher currents to achieve 10.00 mA emission current of the ions. As a way to ensure that the emission current is increased slowly and to monitor the efficiency of the filament, a common practice is to increase the emission current by 0.25 mA and record the voltage and current values on the display readout until 10.00 mA is reached.

- Once 10.00 mA is reached, slowly close the angle valve and increase the D₂ gas pressure to mid 10⁻⁴. At this pressure, it should be easy to find the beam on the RIV faraday cup. Positioning of the faraday cup requires very fine adjustments.
- Maximize the beam current by cycling through each parameter in Table A.1 and optimizing each one. Start first with either PX and PY (translation of the beam) or mass scale on the Wien filter (changing the m/z that passes through the filter).
- Once all settings have been optimized for maximum current, allow the ions to pass through to the main chamber to be detected by the main chamber faraday cup. Read the total ion current at the sample. Increase the gas pressure to the desired current (typically 2000 nA). Then reoptimize the parameter settings again. A good principle is to achieve the highest current with the lowest pressure in the source chamber. The manual suggests not exceeding 1.0×10^{-3} Torr, though more is often required due to the ion gun not being designed to operate with such a large working distance.
- During the experiments, there is no direct method of monitoring the beam current to ensure it remains constant. The cold cathode gauge is a good indicator since the current is directly proportional to the pressure at the source. However, from experience it has been shown that the leak current displayed on the readout of the power supply to the ion gun is the best indicator for fine tuning the beam current. Take note of this value at the beginning of the experiment and adjust the leak valve above the source chamber to keep it constant.

A.3 Ion Beam Alignment

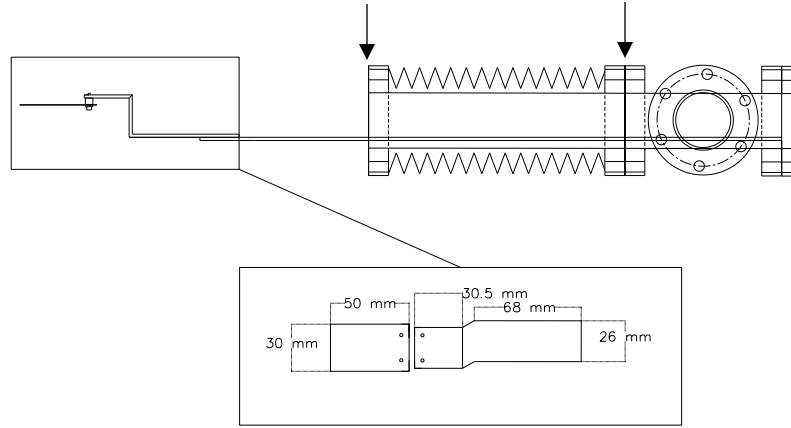


Figure A.2 Design of the main chamber faraday cup (MCFC), which was constructed for the experiments in this thesis. The arrows indicate the distance measured by calipers for positioning the faraday cup in front of the sample.

There are two faraday cups installed on the SSM. The first is in RIV of the differentially pumped chamber and is used to align the ion beam to the target while the second is designed to fit directly in front of the sample in the main chamber in order to measure the total ion current of the ion beam. The primary difference between the two is that the RIV faraday cup has a smaller diameter than the diameter of the ion beam in order to profile the shape of the beam, whereas the detector of the main chamber faraday cup is a tantalum sheet much larger than the size of the beam at the target distance. Both need to be used in tandem for proper alignment.

Prior to experiments being conducted, it was necessary to determine reference points for positioning the faradays cups so that the ion beam would be guaranteed to reach the center of the target. With the main chamber vented and the front plate removed, the main chamber faraday cup was moved in front of the sample holder until the front edge of the tantalum sheet was exactly at the center of where the sample would be. The linear transfer mechanism of the faraday cup does

not exhibit a reference scale for precise positioning. Using calipers to measure the distance between the two flanges on either side of the beveled region of the arm is an ample method that is reproducible over time (Figure A.2). The value on the calipers at which the faraday cup half-covered the target was recorded as 95.0 mm. Thus, the sample is completely exposed when the distance is 102 mm or more and is entirely covered by the faraday cup when the distance is 88 mm and below. THE MC FARADAY CUP SHOULD NOT BE EXTENDED PAST 84.0 MM! THE COLDHEAD SHOULD NEVER BE MOVED WHEN USING THE FARADAY CUP!

A second preliminary test was conducted to align the RIV faraday cup to the center of the beam. With the entire system under UHV, an ion beam of D_2^+ ions was produced and aimed at the target. The MC faraday cup was slowly moved in at increments of 1 mm and the current was recorded (Figure A.3). By adjusting the PX and PY values on the 12/38 power supply, the beam was translated until the curve in Figure A.3 was at half maximum when the calipers showed a distance of 95 mm between the flanges (arrows in Figure A.2). At this point the beam is exactly centered in the X direction of the target surface. With the beam position set, the RIV faraday cup

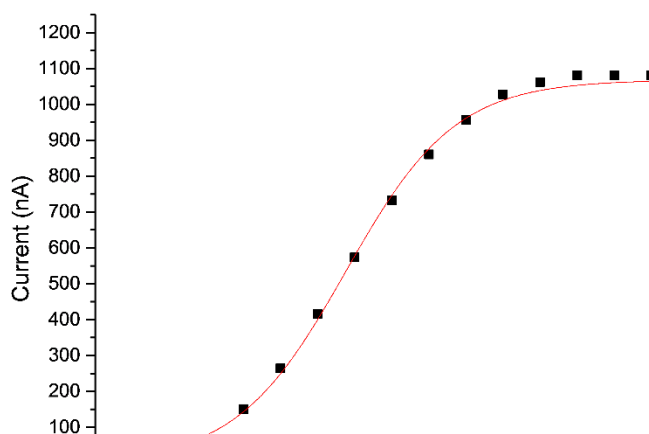


Figure A.3 Ion beam profile using the MC faraday cup.

is then used to profile the beam in the X direction (Figure A.4). It is important to note that the RIV faraday cup rotates in the Y direction around a central axis, so this must be optimized before profiling the beam and locked in place using the lock mechanism. For the experiments in this thesis, the RIV faraday cup showed the maximum peak intensity when the markings on the dial read 64.

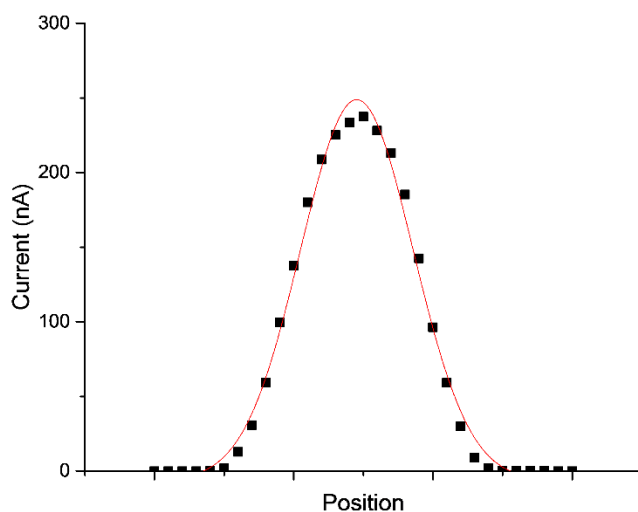


Figure A.4 Ion beam profile using the RIV faraday cup.

Calibrating the positions of both faraday cups with the beam centered on the target is a convenient way to center the beam without irradiating the sample before the experiments are ready to begin. Each experiment was preluded following these steps:

- Start with the RIV faraday cup positioned at 64. Produce the beam as outlined in section A.2.
- Profile the beam by moving the faraday cup to 50 and slowly rotate the dial to move the cup while recording the current in Excel. The dial has 5 major tick marks as it rotates around indicating a value of 1. So current values were recorded at 50, 51, 52... etc.
- Moving across should produce a beam profile like the one seen in Figure A.4. If the peak maximum is not at 64, then the beam is off centered. Move the faraday cup back to 64 and

reoptimize the ion gun parameters on the 12/38 power supply until the maximum current is at 64.

- The beam profile should be symmetrical to a large extent. Otherwise, the beam needs to be optimized at the ion focusing lens and using the stigmator on the Wien mass filter. Consult the operation manuals if this is the case.
- With the beam centered on the RIV faraday cup, move the MC faraday cup into position to measure the total ion current at the sample. Rotate the cup out of the plane of the beam in the Y direction, open the RIV/MC gate valve, and move the phosphor screen from blocking the beam. Adjust the gas pressure for the desired ion current as described in section A.2.
- Block the beam with the phosphor screen, close the RIV/MC gate valve and remove the MC faraday cup. The beam is now ready for the experiment.

The final point to mention is that the SSM lacks the capability to profile the beam in the Y direction. It is important to ensure that the beam is centered in both directions for the experiments or the beam may be clipping part of the face plate of the copper sample holder. One method that works well is to translate the beam in the Y direction using the 12/38 power supply over the surface of the MC faraday cup until the beam current begins to decrease rapidly. At this point, the beam is falling off the edge of the detector. Move the beam in both directions and record the current in excel to see where the current falls off. Between these two values is the center of the target in the Y coordinate. From experience, the center of the MC faraday cup sits slightly lower than the center of the target, so this was taken into account when positioning the beam.

A.4 Ion Selection

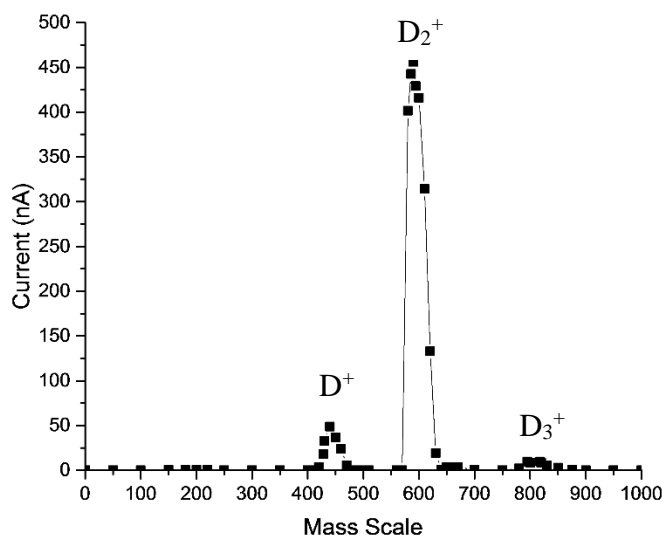


Figure A.5 Relative beam currents of ions produced from D_2 gas (D^+ , D_2^+ , D_3^+)

When a pure gas is ionized in the source chamber of the 12/38 ion gun, typically more than one ion species is produced. For this reason, our model is equipped with a Wien mass filter that allows only a selected *mass-to-charge* ratio to pass through to ensure that the beam produced is free of unwanted ions. The Wien filter works by tuning an electric field held perpendicular to a constant magnetic field produced by a strong magnet. Depending on the molar mass of the gas, there are 3 separate magnets that can be installed with various strengths. For a detailed explanation on the working principle of the Wien filter and the mass ranges of the magnets, see the operation manual published by SPECS.

Selecting the desired ion requires some foreknowledge of the ion species that can be produced. When generating a beam for the first time, it is easiest to start with the ion species that is produced in highest abundance first as some species are generated at very low beam currents and can be extremely difficult to find with the faraday cup. “Finding” a beam is a matter of having

the PX and PY values aiming at the faraday cup and then scanning the mass scale potentiometer on the Wien filter power supply until a current is detected on the picoammeter. The final step is calibrating the mass scale potentiometer for each ion by scanning the dial from 0 to 1000 and recording the beam current on the picoammeter. The result will appear as Figure A.5.